

Validation of land surface temperatures from MSG satellite measurements by observations at the ground station near Evora, Portugal

Zur Erlangung des akademischen Grades eines

DOKTOR-INGENIEURS

von der Fakultät für
Bauingenieur-, Geo, und Umweltwissenschaften
der Universität Fridericiana zu Karlsruhe (TH)

genehmigte

DISSERTATION

von

Dipl.-Ing. Ewa Kabsch

aus Tarnów (Polen)

Tag der mündlichen Prüfung: 12.02.2009
Hauptreferent: Prof. Dr.-Ing. Hans-Peter Bähr
Korreferent: Prof. Dr. Herbert Fischer
Korreferent: Prof. Dr.-Ing. Stefan Hinz

Karlsruhe, 2009

Zusammenfassung

Der erste einer Reihe europäischer Satelliten (Meteosat Second Generation, MSG) wurde 2002 in eine geostationäre Umlaufbahn gebracht und über dem Äquator bei 0° geographischer Länge positioniert. Dieser Satellit liefert alle 15 Minuten einen kompletten Datensatz hoher spektraler Auflösung (12 Kanäle im Bereich von 0.4 bis $14.0 \mu\text{m}$). Die Bodenoberfläche direkt unter dem Satelliten wird in einer Schrittweite von 3 km abgetastet, die sich entsprechend des Betrachtungswinkels vergrößert. Ein wichtiges Produkt des MSG Satelliten ist die Landoberflächentemperatur (LST), die zeitnah durch die LSA-SAF (Satellite Application Facility) zur Verfügung gestellt wird. Das Produkt entsteht aus der in zwei benachbarten Infrarot-Kanälen des Satellitensensors gemessenen Strahldichte, die mit aktuellen Eigenschaften und Wetterinformationen des jeweiligen Bildpunktes in einem komplexen Verfahren kombiniert wird. Für die kontinuierliche Überprüfung der so erhaltenen Landoberflächentemperaturen wurde eine neue Bodenstation aufgebaut.

Es wurde gezeigt, dass der ausgewählte Ort in der Nähe von Evora, Portugal (38.54° N , 8.00° W) über mehrere MSG Bildpunkte ausreichend homogen ist. Diese Gegend besteht hauptsächlich aus Baumkronen und Grasbereichen, was die Hypothese nahe legt, dass die mittlere Landoberflächentemperatur aus der Verteilung nur zweier Temperaturen (Bäume und Gras) dargestellt werden kann. Der Schlüsselparameter dieses Modells, nämlich der bewaldete Flächenanteil um die Bodenstation, wurde zu 0.4 ± 0.1 abgeschätzt. Dies ergab sich aus der Berechnung des Vegetationsindex (NDVI) aus einem hochaufgelösten Landsat Satellitenbild der Region. Zur radiometrischen Bestimmung der Temperatur der Oberflächenelemente wurden Infrarot Sensoren über den Bäumen angebracht und auf Messpunkte im Baum- und Gras-Bereich gerichtet, wobei die Blickrichtung der des MSG Satelliten entsprach. Der Einfluss der von den Messpunkten reflektierten Strahlung wurde durch zusätzliche Messung der atmosphärischen Hintergrundstrahlung ermittelt, so dass die von den Messpunkten emittierte Strahlung berechnet werden konnte.

Die Landoberflächentemperatur der Evora-Region wurde aus der gewichteten Strahlung seiner Oberflächenelemente bestimmt, wobei die Gewichte den jeweiligen Flächenanteilen entsprechen. Es wurde gezeigt, dass der Standardfehler der radiometrisch bestimmten Temperaturen der Evora-Region proportional zur Temperaturdifferenz von Baum- und Gras-Bereich sowie der Standardabweichung des Flächenanteils an Baumbereich ist. Nachts war dieser Fehler typisch etwa 0.2°C und erreichte ein Maximum bis zu 1°C gegen Mittag. Der Vergleich des MSG-LST Produkts mit den am Boden bestimmten Temperaturen der Evora-Region bezieht sich auf den Zeitraum zwischen August 2005 und August 2007. Dabei wurde eine Anzahl offensichtlich falscher MSG-Temperaturangaben entdeckt, die sich auf unerkannte Wolken zurückführen ließen und in der nachfolgenden Analyse weggelassen wurden. Die Anwesenheit von Wolken wurde durch objektive Kriterien festgestellt, die hauptsächlich auf

Messung der atmosphärischen Hintergrundstrahlung basieren. Diese beiden unabhängigen Datensätze korrelieren besser als 0.98 und bestätigen die angegebene Genauigkeit von 2°C für das MSG-LST Produkt. Die kleinsten Temperaturunterschiede traten nachts auf, wobei das MSG Produkt um 1°C niedriger als die am Boden ermittelte Temperatur war. Die größten Temperaturunterschiede traten tagsüber auf und ließen sich auf variable Schattenbereiche an den Messorten zurückführen. Diese Schattenbereiche hängen von Tagesgang und Jahreszeit ab.

Abstract

The first satellite of the series of European geostationary satellites, Meteosat Second Generation (MSG), was launched in 2002 and positioned over the equator at 0° longitude. The satellite provides data at high temporal (15 minutes) and spectral resolution (12 channels covering the range from 0.4 to 14.0 μm). The land surface underneath the satellite is sampled at a distance of 3 km which increases according to the viewing angle. An important product of the MSG satellite is the land surface temperature (LST) which is provided on an operational basis by the LSA-SAF project. This product is derived from the detected radiance in two adjacent infrared bands of the satellite's sensor and combined with actual site and weather information in a complex procedure. For validation of MSG-provided land surface temperatures a new ground station had to be set up.

It has been shown that the selected validation site near Evora, Portugal (38.54° N, 8.00° W) is of sufficient homogeneity within an area comprising several MSG pixels. The site basically consists of tree crowns and grass in between which has led to the hypothesis that the mean land surface temperature of the site is determined by just two temperatures distributed over the land cover elements. The key parameter of this model, namely the area fraction of the site covered by tree crowns, was estimated to 0.4 ± 0.1 from the Normalised Difference Vegetation Index (NDVI) of a high resolution Landsat satellite image. For radiometric determination of the temperatures of the land cover elements the infrared sensors were mounted on a tower above the tree canopy and directed towards the tree and grass targets at the same viewing angle as the MSG satellite. The influence of radiance reflected from the targets was estimated by an additional measurement of the sky radiance, so that the emitted radiance from the targets could be retrieved in a subsequent step. The land surface temperature of the Evora site was derived from the average of radiances of the land cover elements with weights according to their area fraction. It was shown that the standard error of the temperature thus retrieved is proportional to the temperature difference of the land cover elements and the standard deviation of the tree area fraction. At night this error was typically around 0.2°C and displayed a peak of up to 1°C around noon.

Comparisons of the ground and satellite based LSTs refer to the period between August 2005 and August 2007. Analysis of MSG derived land surface temperatures of the Evora site revealed a number of outliers due to undetected clouds that were excluded from the subsequent comparisons with LST ground data. The presence of clouds was established by objective criteria based mainly on ground measurements of the sky radiance. These two independent datasets correlate to better than 0.98 and confirmed the specified nominal accuracy of 2°C of the MSG-LST product. The smallest deviations occurred at night with the satellite derived LSTs lower by about 1°C. The larger deviations observed at

daytime arise from shaded areas of the measurement targets at the ground station. These shaded areas vary in a diurnal and seasonal dependent way.

Index

1	<i>Introduction</i>	- 1 -
2	<i>Meteosat satellite system</i>	- 3 -
3	<i>Physical background</i>	- 10 -
3.1	Definition of temperature	- 10 -
3.2	Thermal emission	- 10 -
3.3	Brightness temperature	- 11 -
3.4	Emissivity	- 12 -
3.5	Radiometric ground temperature measurements	- 13 -
3.6	Land surface temperature	- 14 -
3.7	Radiative transfer model of the atmosphere	- 15 -
3.8	Land surface temperature retrieval from MSG satellite	- 16 -
4	<i>Ground validation station</i>	- 21 -
4.1	Existing LST validation sites	- 21 -
4.2	Requirements for LST validation sites	- 22 -
4.3	Potential validation sites in Europe	- 23 -
4.4	Characterisation of the Evora site	- 24 -
4.5	Site characterisation with high resolution satellite images	- 26 -
4.5.1	Landsat 5 TM	- 27 -
4.5.2	Ikonos	- 29 -
4.6	Instrumentation of the validation station for LST	- 34 -
4.6.1	Rotating radiometer (Rotrad)	- 35 -
4.6.2	Radiometer KT15	- 37 -
4.6.3	Standard meteorological equipment	- 39 -
4.6.4	Upward-looking pyrgeometer	- 39 -
4.6.5	Upward-looking pyranometer	- 40 -
4.6.6	Sunshine sensor	- 40 -
4.6.7	Data recording	- 40 -
4.7	Initial measurements at the institute in Karlsruhe	- 41 -
4.8	Implementation of the LST validation system	- 42 -
5	<i>Data collection and preprocessing</i>	- 51 -
5.1	Emissivity of the Evora site	- 51 -
5.2	Ground measurements	- 52 -
5.3	Acceptance criteria for ground data	- 61 -
5.4	Acceptance criteria for satellite data	- 61 -
5.5	Evora ground temperature	- 63 -
5.6	Resampling	- 67 -
5.7	Error analysis	- 68 -
6	<i>Comparisons of ground and satellite LSTs</i>	- 77 -
6.1	Comparisons with MSG data	- 77 -

6.2	Comparisons with Meteosat-7 data	- 85 -
7	<i>Conclusions and outlook</i>	- 89 -
8	<i>References</i>	- 91 -
9	<i>Publications of the author</i>	- 97 -
10	<i>Acknowledgement</i>	- 98 -
11	<i>List of used notations</i>	- 100 -
12	<i>List of used abbreviations</i>	- 101 -
13	<i>Appendix</i>	<i>i</i>
13.1	Rotrad technical details	i
13.2	Description of datalogger output file	vi

1 Introduction

Earth surface temperature is a key parameter in the physical description of surface-atmosphere interactions and energy fluxes. It is an important factor in modelling large hydrological systems and land surface energy balance. Long-term temperature monitoring is used to quantify the greenhouse effect. Knowledge of the temperature distribution is of prime importance in agricultural applications such as e.g. evaluating water requirements for wheat growth and for determining frost damage in orange groves ([Caselles and Sobrino, 1989](#)). Suitability of the surface temperature data in environmental applications is limited by their accuracy; for example, 1 – 3°C errors in surface temperature can lead to surface flux errors of up to 100 W/m² ([Kustas and Norman, 1996](#)).

The possibility for efficient radiometric observations of surface temperature from satellites has been recognised already in the late 1960's ([Price, 1984](#)). Operational retrieval of the surface temperature on a global scale is only possible with remote sensing measurements from satellites in atmospheric windows. In order to obtain surface temperatures by remote radiometry it is necessary to take the surface emissivity of the measurement target into account ([Becker, 1987](#)) and to correct the recorded signal for the atmospheric attenuation along the path to the satellite's sensor. The main obstacle of temperature determination from satellites in infrared range is the presence of clouds and only for completely cloud-free pixels surface temperature determination is reliable.

Due to the success of the infrared measurements in determining temperature of the water surface ([Prabhakara et al., 1974](#); [McMillin, 1975](#)) much work has been done to extend these methods to the problem of estimating land surface temperatures (LST). LST retrieval methods have been recently reviewed by e.g. [Prata et al., 1995](#), [Sobrino et al., 2002](#), and [Dash et al., 2002](#).

In general LSTs have a strong diurnal variation which can be observed by geostationary satellites due to their excellent temporal resolution. Furthermore, the high altitude of the satellite at about 36 000 km allows simultaneous sampling of large parts of the globe that extend from the equator to the middle latitudes.

The first series of geostationary Meteosat satellites, Meteosat-1 – Meteosat-7, was operated during the period 1977 – 2006 delivering images of the Earth and its atmosphere every half hour in three spectral channels. The first satellite of the Meteosat Second Generation (MSG) program was launched in 2002. The excellent spectral and spatial resolution of the Spinning Enhanced Visible and Infra-Red Imager (SEVIRI) of the MSG satellite allows observations every 15 minutes in 12 spectral channels. The wealth of this information and the correct operation of the satellite are supervised by Eumetsat (www.eumetsat.de). Eumetsat has initialised and coordinates the Satellite Application Facility (SAF) network. Land surface temperatures are provided as one of the main products by the Land Surface Analysis subdivision of SAF (LSA-SAF).

The LST product is operationally computed using the generalised split-window algorithm proposed by [Wan and Dozier, 1996](#) and adapted to the MSG data ([Madeira, 2002](#)). The algorithm corrects for atmospheric effects based on the differential absorption in two adjacent IR bands. It uses pre-calculated coefficients from an extensive look-up table that are updated according to the actual atmospheric conditions at the measured pixels. In addition, the algorithm requires emissivity information which is independently estimated based on land cover classification.

The complex procedure used to generate the LST-MSG product requires permanent validation by ground-based measurements. A number of regions were evaluated, but none of the existing stations were found suitable for MSG. Many of them are not in the field of view of this satellite or are too heterogeneous which would prevent reliable ground measurements at the site. It is shown that a suitable validation site for MSG is the area near Evora, Portugal. Characterisation of the selected site, instrumentation set-up, measurements, determination of surface temperatures of the site and comparisons with the corresponding LST satellite products are described in this thesis.

2 Meteosat satellite system

The Meteosat satellite system is a series of geostationary meteorological satellites operated by Eumetsat. The first generation of Meteosat satellites, Meteosat-1 to Meteosat-7, has produced images of the Earth and its atmosphere every half an hour in three spectral channels (visible, infrared and water vapour regions of the electromagnetic spectrum) via the Meteosat Visible and Infrared Imager (MVISR) instrument. Within the operational period (1977 – 2006) the first series of the Meteosat satellites has provided the raw data for a wide range of meteorological products. The improvements in the first series of Meteosat satellites resulted in the new generation of the geostationary satellites ([The Meteosat System, 2000](#)).

The new generation of Meteosat, called Meteosat Second Generation (MSG), consists of a series of four geostationary meteorological satellites that will operate consecutively until 2018. The first one of this series, the MSG-1 satellite also named Meteosat-8, has been launched on August 28, 2002. MSG-2, named Meteosat-9, started operation in December 21, 2005. MSG-2 is currently the prime satellite in Meteosat service and positioned over the equator at 0° longitude. The MSG-1 serves as a back-up for MSG-2. Each Meteosat scene encompasses Europe, Africa, Near East and partly South America, as shown in Figure 2.1.

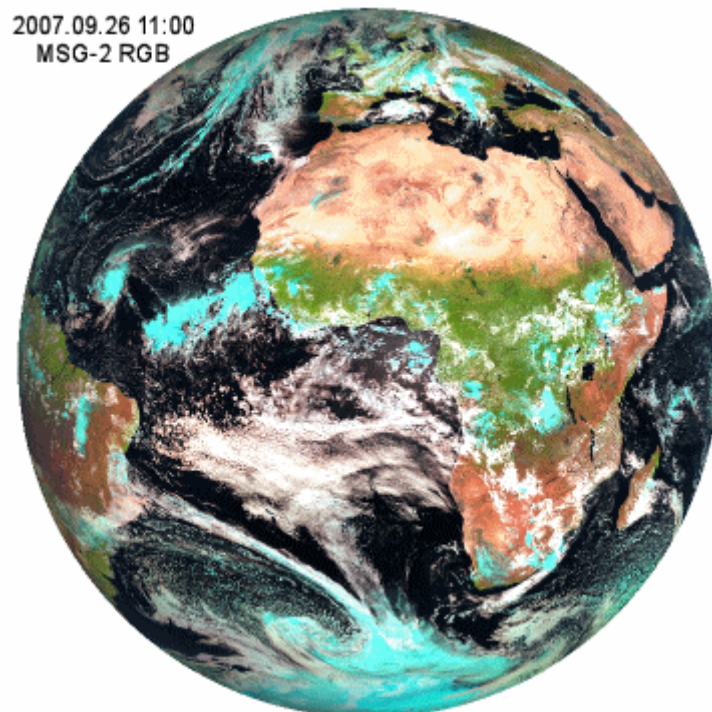


Figure 2.1: The MSG satellite's view of the earth. Three spectral channels 0.6, 0.8 and 1.6 μm are assigned to blue, green and red, respectively. Ice clouds appear in blue because they reflect less solar radiation at 1.6 μm than clouds consisting of water.

Each MSG satellite carries two sensors: the Geostationary Earth Radiation Budget (GERB), and the Spinning Enhanced Visible and Infrared Imager (SEVIRI). The GERB is a scanning radiometer with two broadband channels, one covering the solar spectrum, the other covering a large part of the electromagnetic spectrum. The objective of the GERB sensor is to retrieve radiative fluxes of reflected solar radiation and emitted thermal radiation. The SEVIRI is the main payload on board of MSG ([Sobrino and Romaguera, 2004](#)). Figure 2.2 depicts the principle of the SEVIRI pixel acquisition. Three detectors (nine for high resolution visible, HRV) acquire simultaneously three image lines (nine for HRV) per revolution of the satellite, with sampling distance of 3 km (1 km for HRV) at sub-satellite point both in East-West and in North-South directions. Pixel size underneath the satellite equals $4.8 \times 4.8 \text{ km}^2$, apart from the high resolution visible channel with a pixel size at the sub-satellite point of $1.7 \times 1.7 \text{ km}^2$.

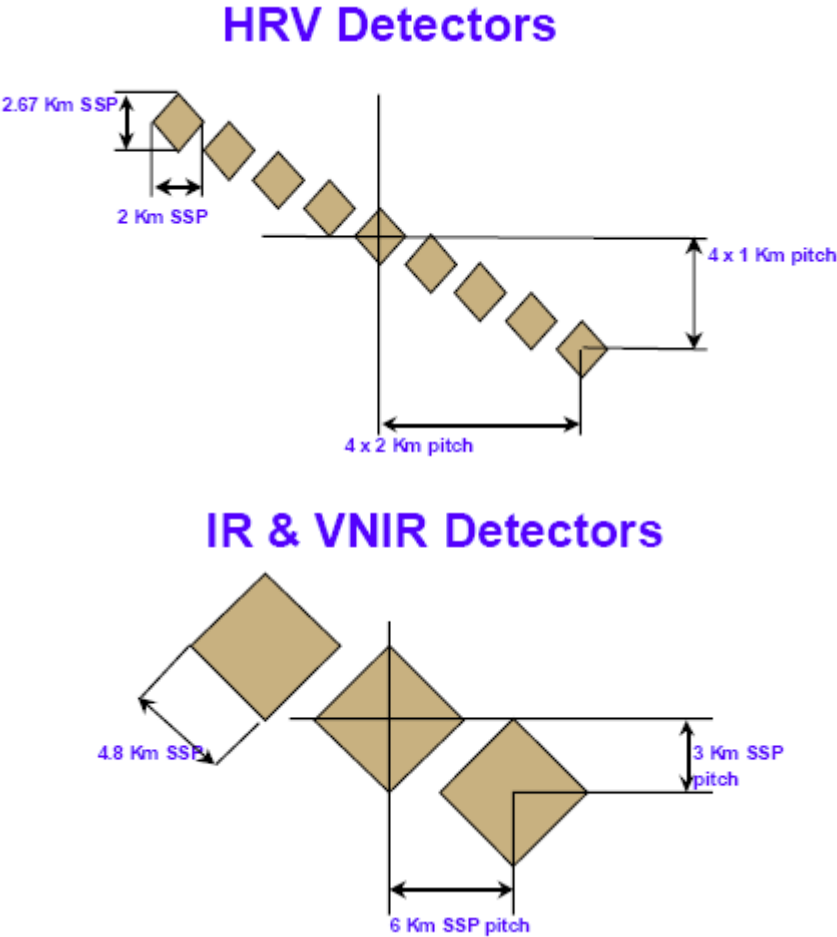


Figure 2.2: Pixel acquisition principle from SEVIRI HRV (above) and IR and VNIR (visible and near infrared, below) detectors. Apparent pixel size underneath the satellite (sub-satellite point, SSP). Figure adopted from [Pili, 2000](#).

Figure 2.3 shows the imaging principle. The east-west scanning capability of SEVIRI is provided by the satellite spin. The MSG satellite spins at a rate of 100 revolutions per minute. Each revolution lasts nominally 600 ms of which about 30 ms are dedicated to Earth viewing. To ensure the necessary south-north coverage, a scan mirror is stepped from south to north in steps of 9 km at SSP. The full Earth disc image is obtained in about 12 minutes. The scan mirror is then driven back to its initial position and a flip-flop type mechanism is actuated to place the infrared calibration reference source into the instrument field of view. The black body is removed after about 2 seconds from the calibration position. Hence, the full Earth disc is then covered in 15 minutes for the 12 spectral channels. The high resolution visible channel provides also full-disc coverage in the north-south, but due to the data limitations only half-disc coverage in the east-west direction. The position of the HVR scene is, however, programmable (Pili, 2000).

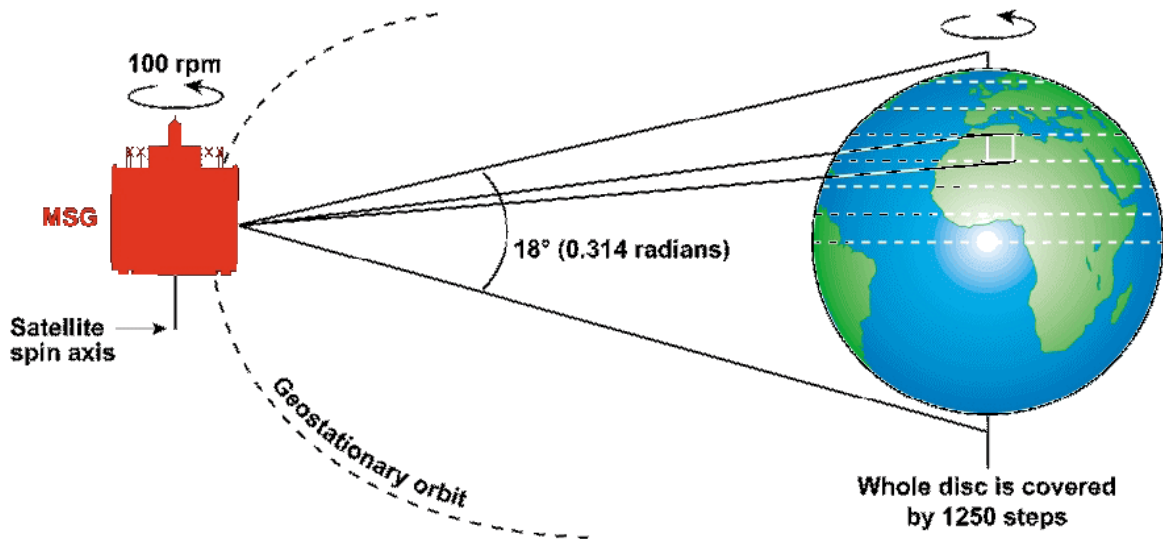


Figure 2.3: SEVIRI image acquisition principle (adopted from [Meteosat Second Generation, MSG System Overview, 2001](#)).

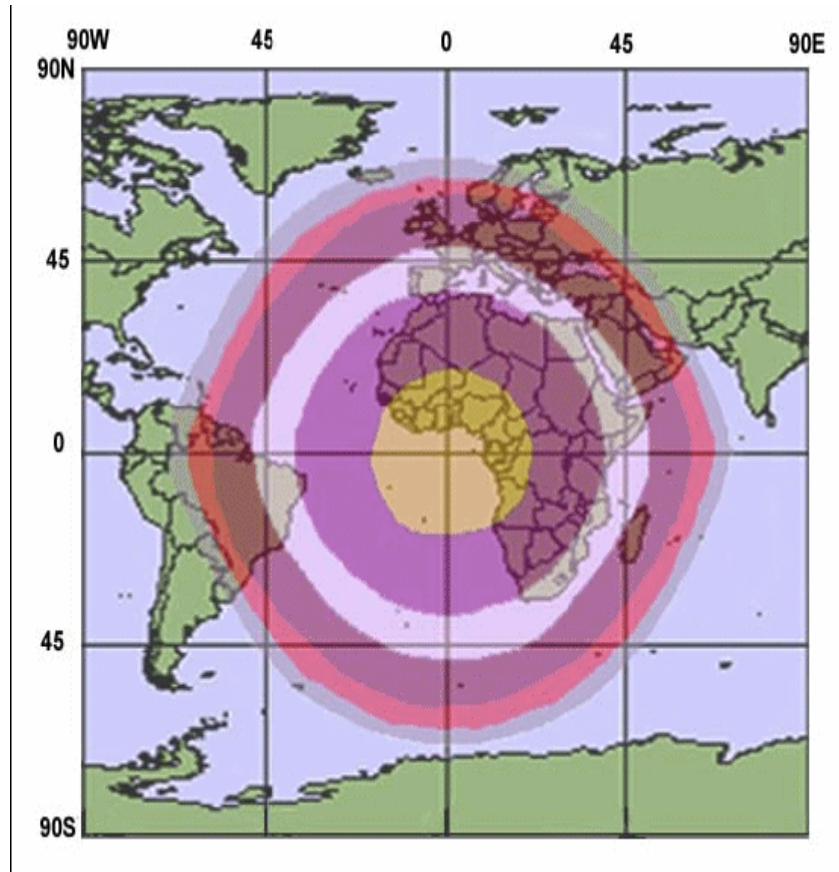


Figure 2.4: SEVIRI multi-spectral image pixel spacing (equivalent surface). The bands show the decrease in pixel resolution away from the sub-satellite point. 3.1 km pixel spacing (inner circle), 4 km, 5 km, 6 km, 8 km and 11 km (outer band). Adopted from [Meteosat Second Generation, MSG System Overview, 2001](#).

Due to the fact that MSG/SEVIRI acquires images in constant angular steps, the on-ground resolution varies according to the geographical location on Earth as shown in Figure 2.4.

Meteosat Second Generation satellite significantly improves the capabilities of the Meteosat First Generation (MFG). The radiometer (SEVIRI) on-board the MSG satellite has a total of 12 imaging channels instead of the three on the original Meteosat satellites. Images are generated every 15 minutes instead of every 30 minutes. The sampling distance of the infrared channels at the sub-satellite point is improved to 3 km compared with 4.5 km, while the new high resolution visible channel provides 1 km instead of the previous 2.25 km sampling distance. The characteristic of the old series of Meteosat satellite compared to the improvements implemented by the MSG is presented in Table 2.1.

Satellite	MFG	MSG
Temporal resolution	30 min	15 min
Spectral channels	3 channels	12 channels
Sampling distance at sub-satellite point	2.25 km (VIS) 4.5 km (IR + WV)	1 km (HRV) 3 km (others)

Table 2.1: Characteristics of the Meteosat First Generation compared to the Meteosat Second Generation (adopted from [Meteosat Second Generation, MSG System Overview, 2001](#)).

The primary mission of the MSG satellites is the continuous observation of the Earth's full disc with a multi-spectral imager. The repeat cycle of 15 minutes for full-disc imaging provides multi-spectral observations of rapidly changing phenomena. SEVIRI has eight spectral channels in the infrared (IR), three channels in the solar spectrum, and a broadband high resolution visible channel. Table 2.2 provides more details of the characteristics of these channels, and indicates how each channel is used for observations of clouds and surface temperatures, water vapour or ozone.

Channel No.	Spectral Band [μm]	Characteristics of Spectral Band [μm]			Main observational application
		λ_{cen}	λ_{min}	λ_{max}	
1	VIS 0.6	0.635	0.56	0.71	Surface, clouds, wind fields
2	VIS 0.8	0.81	0.74	0.88	Surface, clouds, wind fields
3	NIR 1.6	1.64	1.50	1.78	Surface, cloud phase
4	IR 3.9	3.90	3.48	4.36	Surface, clouds, wind fields
5	WV 6.2	6.25	5.35	7.15	Water vapour, high level clouds, atmospheric instability
6	WV 7.3	7.35	6.85	7.85	Water vapour, atmospheric instability
7	TIR 8.7	8.70	8.30	9.1	Surface, clouds, atmospheric instability
8	TIR 9.7	9.66	9.38	9.94	Ozone
9	TIR 10.8	10.80	9.80	11.80	Surface, clouds, wind fields, atmospheric instability
10	TIR 12.0	12.00	11.00	13.00	Surface, clouds, atmospheric instability
11	TIR 13.4	13.40	12.40	14.40	Cirrus cloud height, atmospheric instability
12	HRV	Broadband (about 0.4 – 1.1 μm)			Surface, clouds

Table 2.2: Spectral characterisation of the SEVIRI in terms of central, minimum and maximum wavelength of the channels and the main application areas of each channel (adopted from MSG interpretation guide provided by Eumetsat: http://oiswww.eumetsat.org/WEBOPS/msg_interpretation/index.html).

All spectral regions are affected by the absorption in the atmosphere. However, in ranges of atmospheric windows the Earth's atmosphere is largely or partially transparent (chapter 3.7). The distribution of the SEVIRI infrared channels over the atmospheric windows with main absorbing gases in each range is shown in Figure 2.5. Water vapour is responsible for atmospheric effects in the whole presented range with different intensity. Other gases absorb the radiance only in some selected parts of spectral range. Figure 2.5 presents the radiance measured by the infrared sensor at the top of atmosphere, converted to temperature via Planck's equation. This brightness temperature (chapter 3.3) can be interpreted as a weighted average temperature of the atmospheric layers where the absorbing gases are present. The graph shows also the influence of gases present in the atmosphere on radiance propagation.

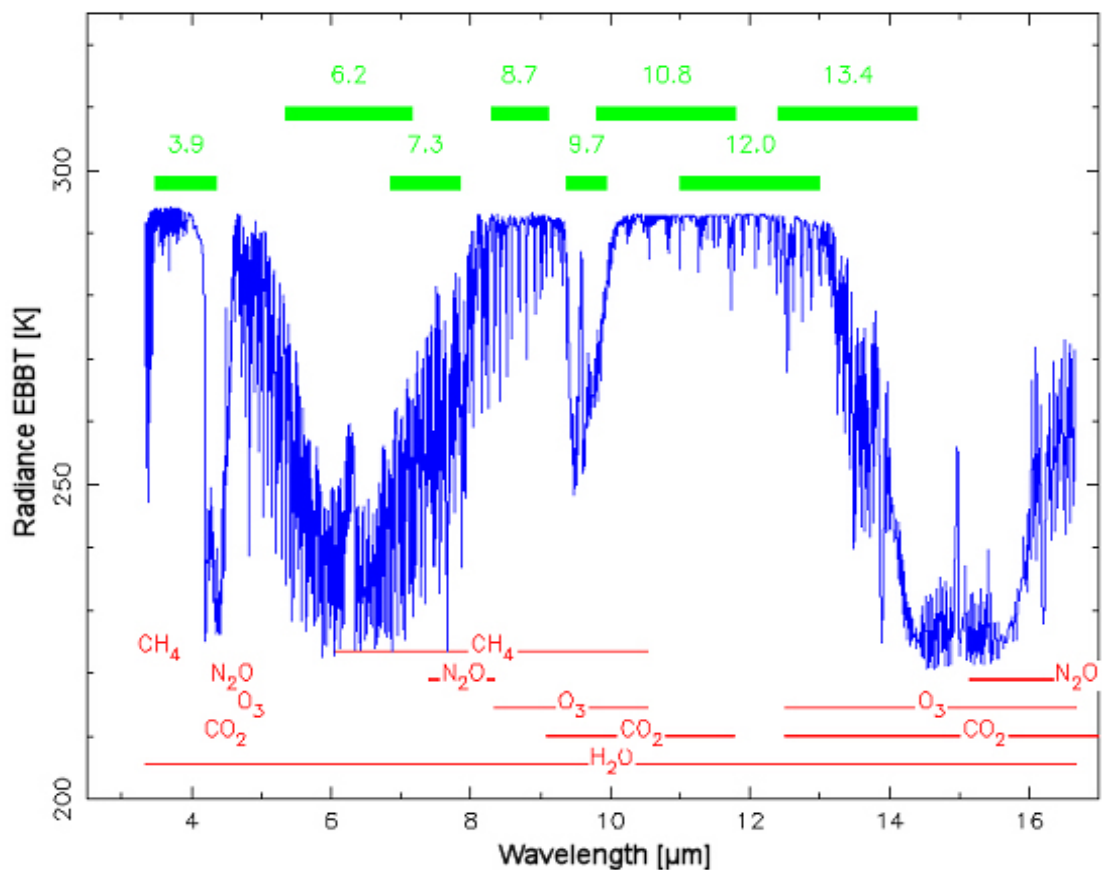


Figure 2.5: 99% energy bandwidths of the SEVIRI infrared channels (green bars) in terms of its distribution within atmospheric windows. The blue line represents the radiance equivalent black body temperature (EBBT), also called brightness temperature (adopted from MSG interpretation guide: http://oiswww.eumetsat.org/WEBOPS/msg_interpretation/index.html).

3 Physical background

Each body emits electromagnetic radiation depending on its temperature. Measurements of the thermal radiation thus provide an important method for temperature determination that does not require thermometers in close contact to the measured object. For a perfect black body – an object that absorbs all incident electromagnetic radiation – the emitted radiance is given by Planck’s equation. The body temperature can be obtained from the radiance at a fixed wavelength by inversion of the Planck formula. The physical background of the methods employed for remote temperature retrieval of real objects is given in this chapter together with a short discussion of the effect of the atmosphere on the radiation sensed by a satellite.

3.1 Definition of temperature

Thermodynamic temperature is a macroscopic quantity that is constant for any group of interacting subsystems when no heat transfer takes place ([Norman and Becker, 1995](#)). It can be shown that thermodynamic temperature is independent of properties of the material. Intuitively, temperature is a measure of how hot or cold something is. The unit of temperature in the International System of Units (SI) is the Kelvin [K]. By definition, absolute zero is a temperature of precisely 0 K or -273.15°C. A temperature increment of one Kelvin is identical to that of one degree Celsius. It is often convenient to use the Celsius scale, in which 0°C corresponds to the temperature at which water freezes and 100°C corresponds to the boiling point of water at sea level.

From the atomic point of view temperature is a measure of the mean kinetic energy of the particles in a monatomic gas; the mean kinetic energy of the particles is proportional to the absolute temperature T of the gas, and given by

$$\frac{mv^2}{2} = \frac{3}{2}kT \quad \text{Eq. 1}$$

where m is the mass of a particle, v^2 is the mean squared velocity of particles, and k is Boltzmann’s constant ($k = 1.381 \times 10^{-23}$ J/K).

3.2 Thermal emission

A black body is defined as an object that absorbs all incident electromagnetic radiation. If the black body is in thermal equilibrium with its environment at finite temperature it will on average emit exactly as much radiation as it absorbs, at every wavelength (Kirchhoff’s law). At room temperature, black bodies emit infrared light, and start emitting at visible wavelengths as the temperature increases above a few hundred degrees Celsius. Technically, a black body can be realised to close approximation as a small hole in an empty box.

The amount of black body spectral radiance emitted at a given wavelength and temperature is described by Planck’s function

$$B_{\lambda}(T) = \frac{2hc^2}{\lambda^5 \left(e^{\frac{hc}{k\lambda T}} - 1 \right)} \quad \text{Eq. 2}$$

where $c = 2.998 \times 10^8$ m/s is the speed of light, $h = 6.626 \times 10^{-34}$ Js is Planck's constant, and $k = 1.381 \times 10^{-23}$ J/K is Boltzmann's constant. If λ is given in m, the physical dimension of B_{λ} is power per unit surface area per unit solid angle per unit wavelength $W/(m^2 \text{ sr m})$.

From Planck's function it follows that maximum emission from a black body of temperature T occurs at wavelength λ_{max} , as given by Wien's displacement law

$$\lambda_{\text{max}} = \frac{C}{T} \quad \text{Eq. 3}$$

where the constant $C = 2.898 \times 10^{-3}$ mK. For example, the sun with a temperature of about 6000 K has its peak emission at a wavelength of 0.48 μm , whereas typical atmospheric temperatures in the range 200 – 300 K yield peak emission in the range 9.6 – 14.4 μm .

The integration of Planck's function over all wavelengths and over a hemisphere leads to the total broadband flux as given by the Stefan-Boltzmann law,

$$F_B = \pi \int_0^{\infty} B(\lambda, T) d\lambda = \sigma T^4 \quad \text{Eq. 4}$$

$$\sigma = \frac{2\pi^5 k^4}{15c^2 h^3} = 5.67 \times 10^{-8} \frac{W}{m^2 K^4}$$

Thus, doubling the temperature of a black body leads to sixteen-fold increase of the total emitted broadband flux.

3.3 Brightness temperature

At a fixed wavelength Planck's equation can be inverted to yield the black body temperature as a function of its radiance.

$$T_b = B_{\lambda}^{-1}(I_{\lambda}) = \frac{hc}{k\lambda \ln \left(\frac{2hc^2}{I_{\lambda} \lambda^5} + 1 \right)} \quad \text{Eq. 5}$$

T_b is called brightness temperature and is computed from a measured radiance I_{λ} . Eq. 5 is a starting point for remote temperature measurements also for real objects that deviate from the ideal black body.

For such temperature measurements radiometers are used that are sensitive for radiance within a certain bandwidth $[\lambda_1, \lambda_2]$. Let $f(\lambda)$ describe the spectral response function of the instrument and $B(\lambda, T)$ Planck's function. For a black body at temperature T we expect to observe the radiance

$$I(T) = \frac{\int_{\lambda_1}^{\lambda_2} f(\lambda) B(\lambda, T) d\lambda}{\int_{\lambda_1}^{\lambda_2} f(\lambda) d\lambda} \quad \text{Eq. 6}$$

The weighted mean wavelength λ_f recorded by the radiometer is defined as

$$\lambda_f = \frac{\int_{\lambda_1}^{\lambda_2} \lambda f(\lambda) d\lambda}{\int_{\lambda_1}^{\lambda_2} f(\lambda) d\lambda} \quad \text{Eq. 7}$$

We treat the observed radiance as monochromatic at wavelength λ_f and use the inverse Planck's equation (Eq. 5) to retrieve the brightness temperature T_b . For the black body thermodynamic and brightness temperatures are identical. For non-black bodies this is no longer the case. The brightness temperature now depends on the spectral response function of the radiometer $f(\lambda)$.

3.4 Emissivity

Planck's function $B_\lambda(T)$ describes thermal emission from a black body which corresponds to the maximum possible emission from any object of the same temperature. Real objects do not absorb all incident radiation and thus have lower thermal emission than a black body. This motivates the definition of emissivity. The monochromatic emissivity ε of the surface of a real object is defined by

$$\varepsilon_\lambda = \frac{I_\lambda(T)}{B_\lambda(T)} \quad \text{Eq. 8}$$

where $I_\lambda(T)$ is the emitted radiance at a given wavelength λ and temperature T . $B_\lambda(T)$ is the radiance that would be emitted by a given surface if it were a black body with temperature T at the wavelength λ .

Emissivity depends generally on wavelength. If this dependency is only moderate within a range of wavelengths the emissivity of the object can be approximated by a constant (grey body). Practically, in radiative measurements the band average emissivity is used, as the instruments are making measurements in a defined spectral range. Accordingly, the equation above have to be modified to account for the spectral response function $f(\lambda)$ of the radiometer (see chapter 3.3). This yields a band average emissivity for a grey body ([Wan and Dozier, 1996](#))

$$\varepsilon_f = \frac{\int_{\lambda_1}^{\lambda_2} f(\lambda)\varepsilon(\lambda)B(\lambda,T)d\lambda}{\int_{\lambda_1}^{\lambda_2} f(\lambda)B(\lambda,T)d\lambda} \quad \text{Eq. 9}$$

The band average emissivity is a function of the surface temperature. In Earth's environment this temperature-dependence is usually very small ([Wan and Dozier, 1996](#)).

Natural surfaces are often composed of regions at different temperatures and emissivities. Let p_t and p_g denote area fractions of tree and grass sub-regions at temperatures T_t and T_g with emissivities ε_t and ε_g , respectively. By extending Eq. 9 to these sub-regions we obtain the combined effective emissivity ([Wan and Dozier, 1996](#))

$$\bar{\varepsilon} = \frac{\int_{\lambda_1}^{\lambda_2} [p_t\varepsilon_t(\lambda)B(\lambda,T_t) + p_g\varepsilon_g(\lambda)B(\lambda,T_g)]f(\lambda)d\lambda}{\int_{\lambda_1}^{\lambda_2} [p_tB(\lambda,T_t) + p_gB(\lambda,T_g)]f(\lambda)d\lambda} \quad \text{Eq. 10}$$

For sub-regions at equal temperature the combined effective emissivity reduces to the simplified form

$$\bar{\varepsilon} = \frac{p_t\varepsilon_t + p_g\varepsilon_g}{p_t + p_g} \quad \text{Eq. 11}$$

3.5 Radiometric ground temperature measurements

For ground measurements atmospheric radiance emitted on the path to the instrument can be neglected. Under this assumption the radiance measured by a near ground IR sensor consists solely of surface leaving radiance, namely the radiance emitted by the surface and reflected radiance from the environment. At wavelength λ the emitted radiance is approximated by the black body radiance B_λ at the temperature T_{sr} of the surface multiplied by the emissivity ε_λ . The radiance reflected by the surface is assumed as reflectance $(1-\varepsilon_\lambda)$ times the irradiance from the sky $B_\lambda(T_{sky})$. The total radiance leaving the surface is thus

$$B_\lambda(T_b) = \varepsilon_\lambda B_\lambda(T_{sr}) + (1 - \varepsilon_\lambda) B_\lambda(T_{sky}) \quad \text{Eq. 12}$$

If the measurements are carried out with a radiometer having spectral response function $f(\lambda)$ the measured radiance leaving the surface is

$$I_{tot} = \varepsilon_f I_{sr} + (1 - \varepsilon_f) I_{sky} \quad \text{Eq. 13}$$

where ε_f is the band average emissivity (Eq. 9) and

$$I_{tot} = \frac{\int_{\lambda_1}^{\lambda_2} B(T_b) f(\lambda) d\lambda}{\int_{\lambda_1}^{\lambda_2} f(\lambda) d\lambda} \quad \text{Eq. 14}$$

$$\varepsilon_f I_{sr} = \frac{\int_{\lambda_1}^{\lambda_2} f(\lambda) \varepsilon(\lambda) B(\lambda, T_{sr}) d\lambda}{\int_{\lambda_1}^{\lambda_2} f(\lambda) d\lambda} \quad \text{Eq. 15}$$

$$(1 - \varepsilon_f) I_{sky} = \frac{\int_{\lambda_1}^{\lambda_2} f(\lambda) (1 - \varepsilon(\lambda)) B(\lambda, T_{sky}) d\lambda}{\int_{\lambda_1}^{\lambda_2} f(\lambda) d\lambda} \quad \text{Eq. 16}$$

An approximation of I_{sky} is obtained from a measurement of the sky radiance reaching the Earth's surface under zenith angle 53° ([Kondratyev, 1969](#)).

From the two observations I_{tot} and I_{sky} we can now estimate the surface emitted radiance I_{sr} by

$$I_{sr} = \frac{I_{tot} - (1 - \varepsilon_f) I_{sky}}{\varepsilon_f} \quad \text{Eq. 17}$$

Together with the weighted mean wavelength λ_f the surface temperature T_{sr} is obtained by inverting Planck's function (Eq. 5). Our radiometrically determined surface temperature is expected to be close to the thermodynamic temperature because of the emissivity correction.

3.6 Land surface temperature

At infrared wavelengths the concept of brightness temperature is useful for remote temperature measurements. At terrestrial IR wavelengths most land and water surfaces as well as dense cloud layers have a nearly constant emissivity $\varepsilon > 0.9$. Therefore, in case of a transparent atmosphere, the brightness temperature of the surface is very close to its thermodynamic temperature (see e.g. textbook [Petty, 2004](#)).

Land surface is far from being a skin or a homogeneous two-dimensional entity. It is often composed of sub-regions of various materials at different temperatures, so there is no equivalent black body with a given temperature yielding the same radiance at all wavelengths ([Norman and Becker, 1995](#), [Becker and Li, 1995](#)). However, for a limited wavelength interval, it is always possible to find a unique integrated temperature that provides a black body

radiance matching the combined radiance of sub-regions even if these have different thermodynamic temperatures.

Let p_t and p_g denote area fractions of tree and grass sub-regions at temperatures T_t and T_g , respectively. If the field of view of the radiometer covers the two sub-regions we expect to observe the combined radiance

$$I(T'_{sr}) = p_t I(T_t) + p_g I(T_g) \quad \text{Eq. 18}$$

which is the weighted sum of the radiances from each sub-region. T'_{sr} is the calculated brightness temperature derived from the observed radiance. T_{sr} is a close approximation to the weighted temperatures of the sub-regions

$$T_{sr} = p_t T_t + p_g T_g \quad \text{Eq. 19}$$

Using Stefan-Boltzmann's law, $F = \sigma T^4$ (Eq. 4), we obtain after some calculations

$$T'_{sr} = T_{sr} \left(1 + \frac{3}{2} p_g p_t \left(\frac{T_g - T_t}{T_{sr}} \right)^2 \right) \quad \text{Eq. 20}$$

For $T_{sr} = 300$ K, $T_g - T_t = 30$ K, and $p_t = p_g = 0.5$ the difference is $T'_{sr} - T_{sr} = 1$ K. For remote measurements the details of sub-structure within the field of view of the radiometer are unknown. What can be determined is the land surface temperature T'_{sr} , which – we have shown here – is a good estimate for the weighted thermodynamic temperatures of the sub-regions.

3.7 Radiative transfer model of the atmosphere

Satellites allow remote sensing of land surface temperature. Due to the presence of gases even the cloud-free atmosphere is far from being transparent in most spectral bands. Figure 3.1 depicts the absorption contribution for a number of gases in the IR range.

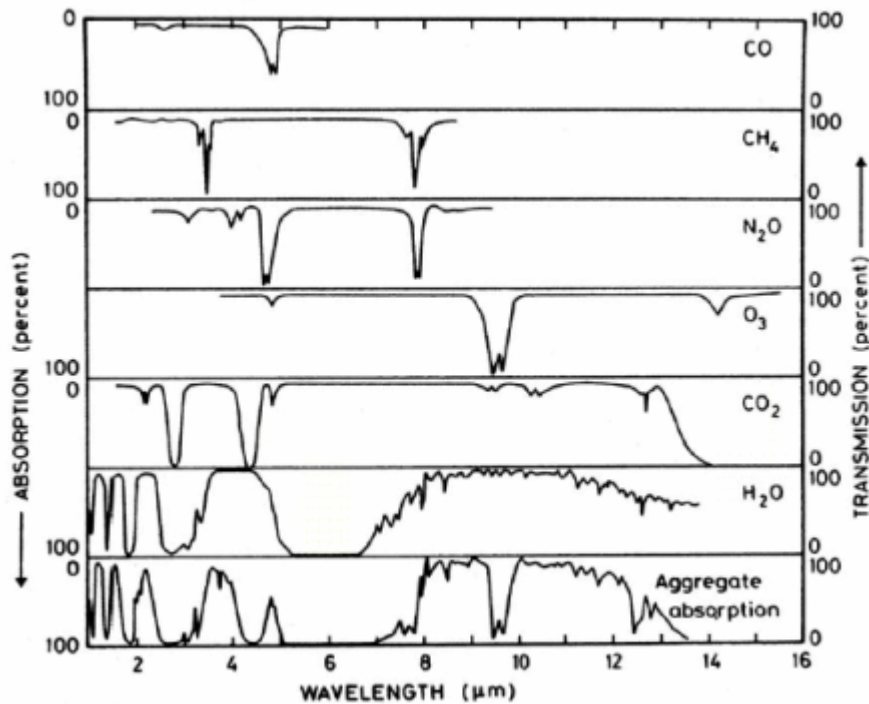


Figure 3.1: Schematic spectrum of most significant atmospheric absorbing gases in the infrared range (adopted from [Brasseur and Solomon, 1986](#)).

For wavelengths in the terrestrial IR region there are broad bands of almost total absorption due to CO₂ (near 4 μm, and 13 – 17 μm), water vapour (5 – 8 μm), and ozone (near 9.6 μm). Obviously, the atmospheric window from 8 to 13 μm, omitting the ozone region, is used for remote surface radiometry (see e.g. textbook [Petty, 2004](#)). For clear-sky conditions, the difference between surface temperature and satellite-measured brightness temperature in the spectral range of 10.5 – 12.5 μm can be as large as 10 K for tropical atmospheres ([Wan and Dozier, 1989](#)).

The treatment of the influence of water vapour on radiative transfer is particularly difficult because its concentration in both horizontal and vertical layers is highly variable. Water molecules tend to cluster by forming hydrogen bonds rather than to distribute evenly in the atmosphere. This influence on radiative transfer is accounted for in the split-window method (see chapter 3.8) by providing frequent sampling of water vapour and near surface air temperature.

3.8 Land surface temperature retrieval from MSG satellite

Historically, retrieval of surface temperature from satellite has concentrated on sea areas ([Prabhakara et al., 1974](#); [McMillin, 1975](#)) because of their homogeneity and a large amount of work has been undertaken to account for atmospheric effects. During the last years this work has been applied and extended to the problem of estimation of land surface temperatures (LST). A review of the used methods can be found in [Prata et al., 1995](#), [Sobrino et al.,](#)

2002, or in [Dash et al., 2002](#). Basically, three methods (and their various combinations) are distinguished:

1. single-channel methods, which use only one IR band (e.g. [Price, 1983](#); [Becker, 1987](#); [Becker and Li 1990](#); [Göttsche and Olesen, 2002a](#); [Göttsche and Olesen, 2002b](#); [Bhattacharya and Dadhwal, 2003](#); [Sobrino et al., 2004a](#))
2. two-channel or split-window methods, which use a combination between two IR bands (e.g. [Price, 1984](#); [Ottlé and Vidal-Madjar, 1992](#); [Wan and Dozier, 1996](#); [Sobrino et al., 1996](#); [Sobrino and Romaguera, 2004](#); [Sobrino et al., 2004b](#))
3. two-path methods, which use one IR band and two atmospheric paths of different length (e.g. [Sobrino et al., 1996](#); [Sobrino et al., 2004b](#))

Advances in satellite techniques are implemented in the second generation of Meteosat satellites. Due to the fact that two of the SEVIRI sensor channels are covering adjacent thermal IR bands, for the atmospheric correction the second method, namely the split-window method, can be used. The effect of absorption and emission of atmospheric gases can be accounted for by differential absorption in two spectrally close infrared bands. Since surface emission is assumed to be known in the bands, the differential shift in sensor measured radiance results almost entirely from atmospheric attenuation. Signal differences of the two channels are mainly due to water vapour content and temperature profile of the atmosphere. The main advantage of this method is that it does not require an accurate description of the atmosphere in the form of vertical profiles of temperature and water vapour and no radiative transfer calculations based on these profiles are needed ([Coll et al., 2006](#)).

The terrestrial radiance peaks at about 10 μm and is most sensitive towards temperature changes in this region ([Dash et al. 2002](#)). A detailed analysis on the suitability of MSG channels for LST retrieval by the split-window technique can be found in [Sobrino and Romaguera, 2004](#).

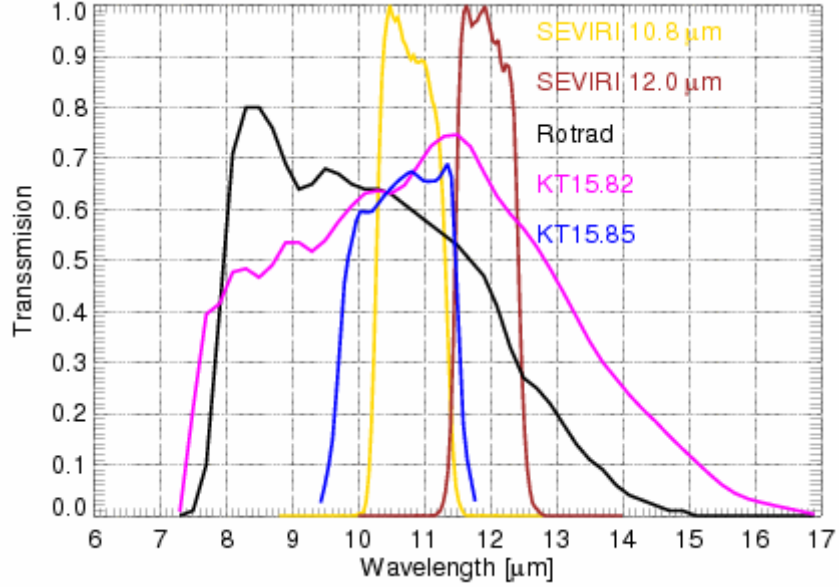


Figure 3.2: Spectral response of two SEVIRI split-window channels compared with the spectral response of the radiometers at the Evora ground station (for further details concerning ground radiometers see chapters 4.6.1 and 4.6.2).

In this thesis we use LST products derived from channels TIR 10.8 μm and TIR 12.0 μm (Figure 3.2) as provided by the Land Surface Analysis Satellite Application Facility (LSA-SAF) via <http://landsaf.meteo.pt/>. For this product the generalized split-window (GSW) algorithm (Wan and Dozier, 1996) adapted to SEVIRI sensor data (Madeira, 2002) is used.

The land surface temperature T_{sr} is provided by LSA-SAF and given by

$$T_{sr} = \left(A_1 + A_2 \frac{1-\varepsilon}{\varepsilon} + A_3 \frac{\Delta\varepsilon}{\varepsilon^2} \right) \frac{T_{10.8} + T_{12.0}}{2} + \left(B_1 + B_2 \frac{1-\varepsilon}{\varepsilon} + B_3 \frac{\Delta\varepsilon}{\varepsilon^2} \right) \frac{T_{10.8} - T_{12.0}}{2} + C \quad \text{Eq. 21}$$

as a time series for each cloud-free image element (pixel) within the satellite's view. $T_{10.8}$ and $T_{12.0}$ are the top of atmosphere brightness temperatures of the 10.8 μm and 12.0 μm SEVIRI bands. $\varepsilon = (\varepsilon_{10.8} + \varepsilon_{12.0})/2$ and $\Delta\varepsilon = \varepsilon_{10.8} - \varepsilon_{12.0}$ are the mean and the difference of the effective emissivities measured in the 10.8 μm and 12.0 μm SEVIRI bands respectively. The effective emissivities are obtained by combining vegetation area and exposed soil as

$$\varepsilon_i = \varepsilon_{i,v} p_v + \varepsilon_{i,g} (1 - p_v) \quad \text{Eq. 22}$$

where $\varepsilon_{i,v}$ and $\varepsilon_{i,g}$ are respectively the vegetation and ground emissivity in channel i and p_v is the land area fraction covered by vegetation (Peres and DaCamara, 2005).

In the generalised split-window method the land surface temperature is calculated as a linear combination of the mean brightness temperature in both SEVIRI split-window channels ($[T_{10.8} + T_{12.0}]/2$) and the difference of these temperatures ($T_{10.8} - T_{12.0}$). The difference in the brightness temperatures is

caused by wavelength dependent attenuation of water vapour in the atmosphere. The A, B and C coefficients are selected from look-up tables using the scan angle and atmospheric information. This atmospheric information includes near-ground air temperature and total column water vapour, both obtained from the European Centre for Medium-Range Weather Forecasts (ECMWF).

The look-up table of optimal GSW coefficients was established using a radiative transfer code ([Berk et al., 2000](#)). The coefficients were obtained by regression analysis of simulated data covering a wide range of atmospheric properties ([Chevallier et al., 2000](#)), surface temperatures, surface emissivity and SEVIRI viewing angles. For details of the method and output data format see [Product User Manual PUM LST, 2006](#) and [Product Output Format Document POF, 2006](#), respectively.

A typical land surface temperature product of the SEVIRI sensor provided by LSA-SAF is shown in Figure 3.3.

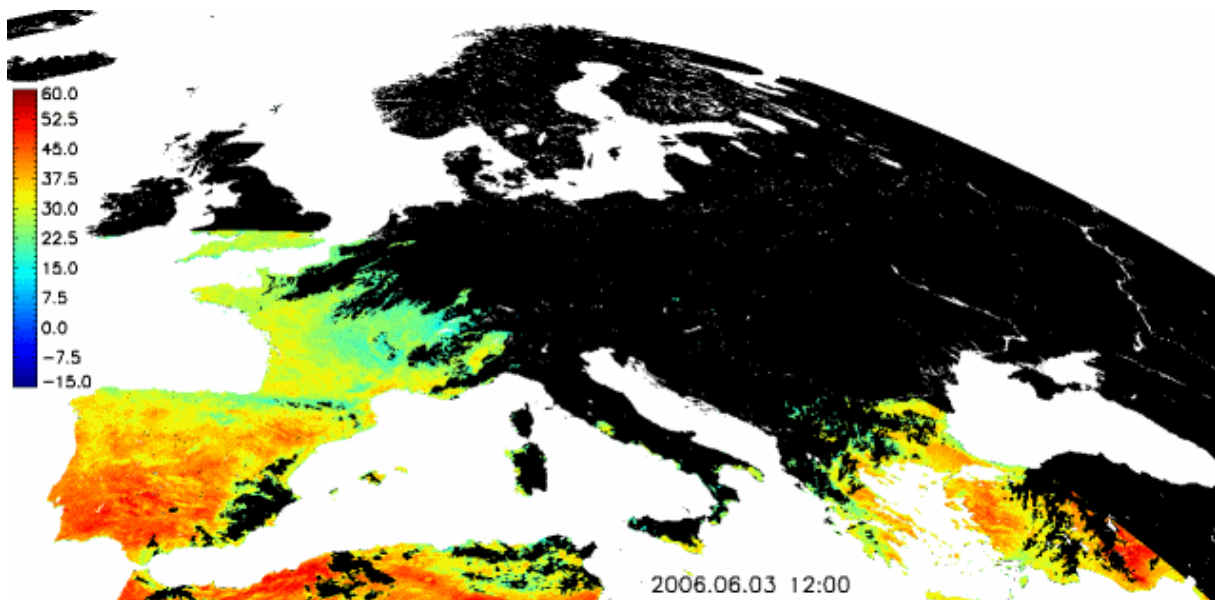


Figure 3.3: Land surface temperature [°C] obtained from the MSG/SEVIRI for zenith viewing angle smaller than 55° ([Product User Manual PUM LST, 2006](#)). Missing LST information due to clouds or regions outside the LST retrieval area is shown in black.

Since the LST retrieval includes only standard aerosol scattering, thin clouds and high aerosol loadings must be detected and excluded from further processing. The cloud mask for the SAF-LST product is provided by Nowcasting and Very Short Range Forecasting (NWC), also a part of the SAF network. Due to high temporal resolution of the SEVIRI (15 min), theoretically, LST and the SAF internal product emissivity can be determined 96 times per day, but in practice fewer observations are available due to cloud cover.

The noise equivalent temperature difference (NE Δ T) for SEVIRI 10.8 and 12.0 μ m channels equals 0.074 K and 0.11 K, respectively. For ‘end of life’

conditions of the sensor the NE Δ T rises to 0.25 K for band 10.8 μ m and to 0.37 K for band 12.0 μ m ([Aminou et al., 2003](#)). However, the final quality of the LST product within LSA-SAF is assessed based on the input parameters: viewing angle, atmospheric characteristics (i.e. near-ground air temperature and column water vapour), and the quality of the emissivity estimation. LSA-SAF defines three LST confidence levels: ‘better than nominal’ ($\pm 1^\circ\text{C}$), ‘nominal’ ($\pm 2^\circ\text{C}$) and ‘worse than nominal’. The accuracy information is embedded in each LST output file together with quality flags for each pixel.

Accuracy studies carried out by LSA-SAF have shown that the LST errors increase for large viewing angles and for moist atmospheric conditions. On the other hand for dry atmospheric conditions the reflected part of radiance corresponds to much lower brightness temperatures than the emitted one, so the algorithm is very sensitive to emissivity uncertainties.

The subject of this thesis is to verify the accuracy of the provided LST from SEVIRI sensor by comparison with corresponding ground-truth observations at a fixed location.

4 Ground validation station

A ground validation station is needed to compare the temperature data from the satellite with the corresponding ground observations. Details of the decision making process that lead to the selection of the Evora site, its characterization and instrumentation are described in this chapter.

4.1 Existing LST validation sites

Lakes are a good starting point for validating of LST algorithms, because water is easily measured and has a stable temperature and emissivity. [Hook et al., 2003](#) and [Hook et al., 2004](#) (<http://laketahoe.jpl.nasa.gov/>) have presented the measurements of the skin temperature over Lake Tahoe in California. This in-situ data were used for calibration as well as validation of surface temperature products from different satellite sensors. Very high accuracy of the LST has been obtained. It results from the homogeneity of the water surface and its relatively narrow temperature range as well as from the dry atmosphere above this lake which is located at high altitude.

[Snyder et al., 1997](#) describe the validation of the LST product determined from MODIS¹ sensor data over Railroad Valley playa in Nevada in the western United States, carried out within one field campaign. Surface temperatures were measured by thermistors, ground radiometers and airborne radiometers. It turned out that spatial distribution of temperature and emissivity within this site varies strongly which adds to the complexity of the validation task.

[Wan et al., 2002](#) have presented the results of seven field campaigns conducted in 2000 and 2001 in California and Nevada, and over Lake Titicaca, Bolivia. Each field campaign lasted for 2 – 3 weeks. It was proven that the MODIS LST accuracy is better than 1 K in the range from 263 to 300 K and for an atmospheric column water vapour range from 0.4 to 3.0 cm. In some cases, however, the MODIS LSTs are few Kelvin degrees lower than the in-situ measured LSTs, mostly due to overestimation of emissivities in semi-arid and arid regions.

Permanent LST validation stations were established in Australia by the Atmospheric Research group from CSIRO² and operated over several years. In scope of this work [Prata, 1994](#) has investigated the issue whether the split-window technique can be applied to land surface. Two field sites were used: Walpeup north-west of Melbourne in Victoria and Uardry near Hay in southern New South Wales. The results demonstrate the applicability of the split-window algorithm for LST retrieval from the AVHRR³ and ATSR⁴ sensor data. Root

¹ Moderate-resolution Imaging Spectroradiometer

² Commonwealth Scientific and Industrial Research Organisation – Australia's national science agency

³ Advanced Very High Resolution Radiometer

⁴ Along-Track Scanning Radiometer

mean square (RMS) deviations of about 1.5 K were obtained for several surface types at these sites. [Prata and Cechet, 1999](#) present the comparisons of GMS^1 -5 satellite data taken every hour over a period of 10 days and two ground-truth sites in Australia (Uardry and Amburla near Alice Springs in the Northern Territory). The results show that LST can be determined from the GMS -5 satellite using split-window with RMS accuracy of 2 – 3°C. Another LST validation site was set up in Thangoo, Western Australia ([Prata, 2003](#)).

[Sobrino et al., 2004b](#) have used available in-situ temperature data from New South Wales in Australia collected in 1999 for validation of ATSR -2 LST data. Using the split-window algorithm RMS deviations less than 1.8 K were obtained. However, these results pertain to situations of relatively low water vapour content (<2 cm) and fairly homogeneous regions.

[Sobrino et al., 2006](#) have validated LST data retrieval from airborne hyperspectral scanner over agricultural areas near Barrax (Albacete) and Córdoba in Spain. The tests conducted in this study showed that the split-window method provides RMS errors between 1.6 and 1.9 K.

[Coll et al., 2006](#) describe field campaigns during the summers of 2002 – 2005 over thermally homogeneous rice fields in full vegetation at Valencia, Spain. The split-window algorithm implemented to AATSR^2 data was proven to work satisfactorily provided that the characteristic of the area is correctly described (emissivity and vegetation cover fraction). Studies on 23 pairs of ground measurements and corresponding AATSR data revealed an agreement of $\pm 1.0^\circ\text{C}$. In another study carried out in Valencia ([Coll et al., 2005](#)) the MODIS LST product was found to agree well with the ground measurements (bias of $+0.1^\circ\text{C}$ and standard deviation of 0.6°C for 11 cloud-free cases and viewing angles smaller than 60°). The Valencia site was also used by [Sobrino et al., 2004a](#) to test the LST algorithms implemented for channel 6 data of Landsat 5 Thematic Mapper (TM).

None of the existing sites mentioned above was found to be optimal for a permanent LST validation station for MSG/SEVIRI . Many of them are not in the field of view of this satellite or are too small to be representative for the MSG/SEVIRI measurements. Therefore, an effort has been made to set up a new permanent station aimed at validation of LSTs derived from MSG data on a regular basis.

4.2 Requirements for LST validation sites

Preferentially, the first permanent LST validation station for MSG should be located in Europe which has advantages in ease of access, available logistics and political stability.

¹ Geostationary Meteorological Satellite (Japanese satellite)

² Advanced Along-Track Scanning Radiometer

The most important factor for any LST validation site is the homogeneity of its surface temperature. Thermal heterogeneity is minimised for regions with uniform land cover and soil moisture. Also, a validation site should not include agricultural regions because of their seasonally changing patterns of growing and collected crops. The validation site should be flat to reduce local temperature variations and to guarantee visibility of the site from the satellite sensors.

To be useful, the validation site should have many cloud- and fog-free days. Another consideration is the satellite's viewing angle of the validation site: large angles lead to increased pixel sizes (Figure 2.4) and imply a longer path for the surface emitted radiance through the atmosphere which weakens the signal. These considerations suggest a location in southern Europe.

The above mentioned conditions must be satisfied throughout the area of the validation site. The area should be big enough to accommodate the size of four satellite pixels to allow for some ambiguity caused by resampling of the original pixels. For SEVIRI with a pixel size of $\sim 6 \times 6 \text{ km}^2$ (Figure 2.4) the minimum area of the validation site should be $\sim 12 \times 12 \text{ km}^2$.

Potential LST validation sites within Europe were identified automatically using the procedure described in the work of [Dash et al., 2004](#). The procedure is based on the high resolution data from the AVHRR sensor of NOAA¹ satellite (1 km resolution) taken between March and October 2002. Two methods were applied. By the moving window technique sample mean and variances of AVHRR brightness temperatures are calculated for a window size of 25×25 pixels. In the second method, segments of brightness temperature information and vegetation data (NDVI), derived from the same satellite, are combined with a digital elevation model (DEM). By the combination of the two methods homogenous areas were identified in middle-south Portugal, in Spain (south of Madrid) and in southern France (Landes).

The final decision on the exact location for the validation site was based on field visits ([Prata, 2004](#)), and whether cooperation with local colleagues would be possible. The cooperation with Dr. Prata, who has successfully run ground validation stations in Australia ([Prata et al., 2000](#)), was extremely useful for selection and development of the station and its instrumentation.

4.3 Potential validation sites in Europe

One of the potential sites is found in the province of Valencia in Spain ([Sobrino et al., 2004a](#), [Coll et al., 2005](#) and [Coll et al., 2006](#)). This region is relatively homogeneous and mostly covered with wine plantations and crops. Potential cooperation partners could come from the University of Valencia, who are running nearby agricultural stations. However, the land cover changes irregularly in the growth and harvest seasons as well as by the daily irrigations.

¹ National Oceanic and Atmospheric Administration

The forest in southern France (Landes) was reported by [Dash et al., 2004](#) to exhibit low standard deviation of brightness temperature at a 1 km scale. A flux measurement station 20 km south-west of Bordeaux is located in pine forest that covers large parts of the area. Randomly spread clear-cuts due to storm and human activities in the forest make this region unsuitable as a LST validation site (http://www.bgc-jena.mpg.de/public/carboeur/sites/le_bray.html).

Three potential validation sites in Portugal were reported by [Prata, 2004](#). The first one between Lisbon and Sines (coordinates: 38.29839° N, 8.47355° W, 89 m ASL) was found unsuitable as a validation site because of the heterogeneity at scales of 10 – 100 m. Therefore, ground measurements at this site are unlikely to be representative for MSG data.

The second one is a hilly terrain south of Grandola covered with dense forest (coordinates: 38.16723° N, 8.64496° W, 26m ASL¹). A fire-watch tower exists that has main power access and is close to the road. It initially appeared to be useful for a planned LST validation station. However, the tower is not tall enough to ensure representative measurements. Moreover, there is a big threat of forest fire.

The third site is located near Evora. It was found suitable for establishing our LST ground station.

4.4 Characterisation of the Evora site

The Evora tower (coordinates: 38.53888° N, 7.99985° W, 265 m ASL) is located in Mitra (Alentejo Central, Portugal), approximately 120 km from Lisbon. The Evora city is about 10 km away from the field site. Electric power, telephone line and maintenance by local staff are available. The height of the tower, about 28 m, allows measurements well above the tree crowns (typically 8 m high). The tower is operated by the Instituto Superior de Agronomica (ISA, Technical University of Lisbon) in collaborations with the University of Evora. It is used to measure carbon fluxes (CarboEuroFlux² project, <http://www.bgc-jena.mpg.de/public/carboeur/sites/evora.html>). Figure 4.1 shows a picture of the Evora tower.

¹ Above Sea Level

² CarboEuroFlux – an investigation on carbon and energy exchanges of terrestrial ecosystems in Europe, funded by European Commission DG Research.



Figure 4.1: The 28 m high Evora tower in the holm and cork oak woodland (adopted from [Prata, 2004](#)).

The region of Alentejo Central is a wide open holm oak and cork oak woodland (Figure 4.2). This type of vegetation covers a large portion of the Mediterranean region (in Portugal more than 10 000 km²), partly interlaced with residential or industrial areas. This evergreen woodland is not influenced by the vegetation season, thus retaining its character of interlacing trees and grass over the whole year. The grass, however, changes its appearance from fresh and bright green in late winter and spring to yellow and dry in summer, which causes variable emissivity. To feed the water needs a number of dams were constructed. The countryside of Evora characterises gentle slope topography (2 – 5°). The Mediterranean-oceanic climate zone determines rainy and chilly season starting in November or December and lasting to February or March. From May to September the weather usually stays hot and dry. The mean precipitation is 665 mm/year and the mean annual temperature is 15.4°C with north-west prevailing wind direction (see http://carbodat.jrc.it/data_arch_site_indiv.cfm?db_id=19). This is in line with relatively rare cloud cover observed at this site.



Figure 4.2: View of the Evora tower from the top of a neighbouring hill (38.537 N, 8.033 W). The tower is in the centre of the picture.

Precise maps and a high resolution Landsat image of the Evora site indicate that the landscape north and west from the tower is more homogeneous than in the other directions. This was confirmed for the region up to 20 km from the station by field inspection using a track-car. It was decided to use MSG pixels from this region (see chapter 5.4) for radiometric comparisons between LST determined from satellite and ground measurements.

4.5 Site characterisation with high resolution satellite images

Site inspections indicate that the selected validation site consists of two kinds of land cover: tree regions and grass (non-tree) areas. To further verify this assumption and to estimate the fraction of tree regions high resolution satellite images from Landsat and Ikonos were analysed. The size of the analysed area is $12 \times 12 \text{ km}^2$ which could accommodate about four adjacent MSG pixels. The analysis of the Landsat image reveals a tree canopy fraction of 40%.

4.5.1 Landsat 5 TM

4.5.1.1 Brightness temperature distribution

Landsat 5 TM images of the Evora site from October 8, 2003 were kindly provided by our cooperation partners from the University of Lisbon. The Landsat IR data (channel 6; 10.4 – 12.5 μm ; pixel size 120 m) have been converted to top of atmosphere brightness temperature. For conversion of Landsat spectral radiance to brightness temperature the following equation is used.

$$T_b = \frac{K2}{\ln\left(\frac{K1}{L_\lambda} + 1\right)} \quad \text{Eq. 23}$$

T_b [K] is the brightness temperature, with calibration constants $K1 = 607.76$ [$\text{W}/(\text{m}^2 \text{ sr } \mu\text{m})$] and $K2 = 1260.56$ [K], and L_λ is the spectral radiance at the sensor's aperture ([Chander and Markham, 2003](#)). The result is depicted in Figure 4.3.

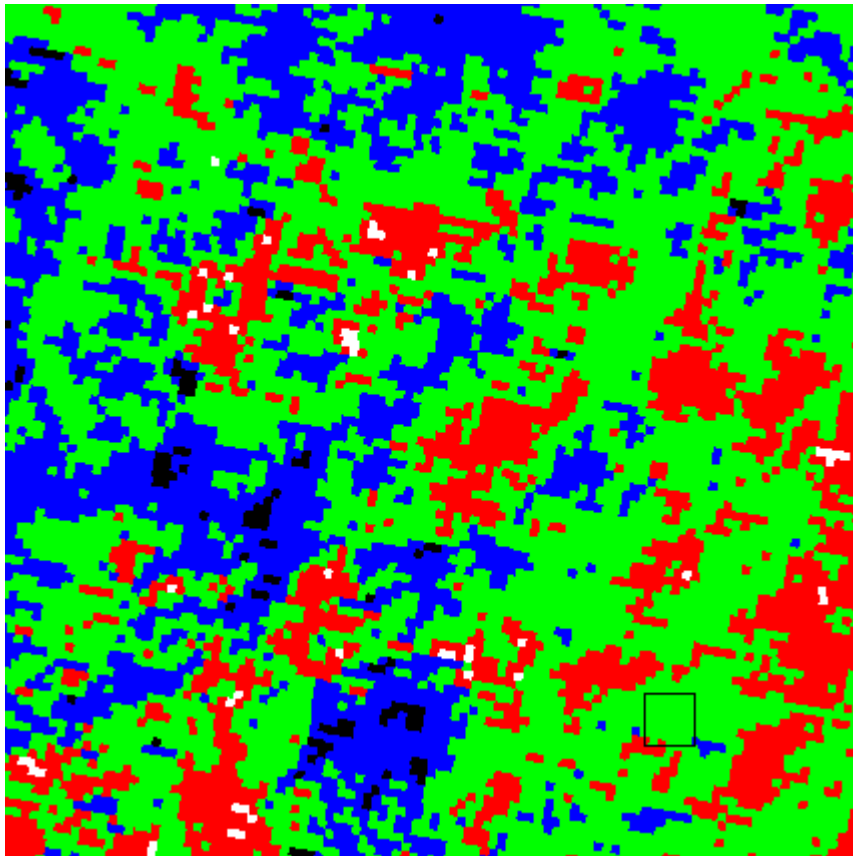


Figure 4.3: Top of atmosphere brightness temperature over Evora site taken by Landsat 5 (channel 6, 10.4 – 12.5 μm) on October 8, 2003. Temperature colour code: black: 18 – 21°C; blue: 21 – 23°C; green: 23 – 25°C; red: 25 – 27°C; white: 27 – 31°C. The picture shows a region of 12 \times 12 km^2 , the Evora tower is marked in the lower-right corner.

A histogram of the top of atmosphere brightness temperature distribution of the above Landsat image is shown in Figure 4.4. The temperatures range from 18°C to 31°C, with a mean value of 23.7°C and a standard deviation of 1.3°C. The brightness temperature at the station tower is 23.5°C.

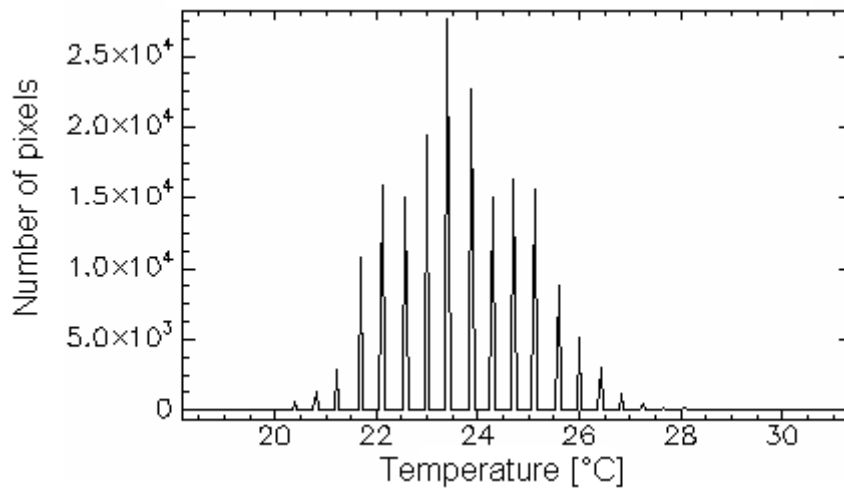


Figure 4.4: Histogram of the top of atmosphere brightness temperatures calculated from image shown in Figure 4.3.

4.5.1.2 Estimation of the tree canopy cover

[Carreiras et al., 2006](#) have developed empirical models employing remote sensed data to estimate the percentage of tree canopy cover applicable to evergreen oak woodlands. For the Evora site ($12 \times 12 \text{ km}^2$) the fraction of trees as a function of the Normalised Difference Vegetation Index (NDVI) was kindly provided by Dr. Carreiras. The area fraction covered with tree crowns is 0.4 with a standard deviation of 0.07. Presumably, this error is a somewhat too optimistic estimate and we assume that an error of 0.1 would be more realistic. These calculations were made with Landsat 5 TM reflectance data with a pixel size of 30 m. The Landsat image was taken on August 15, 1995. Figure 4.5 shows the distribution of the tree canopy of the Evora site.

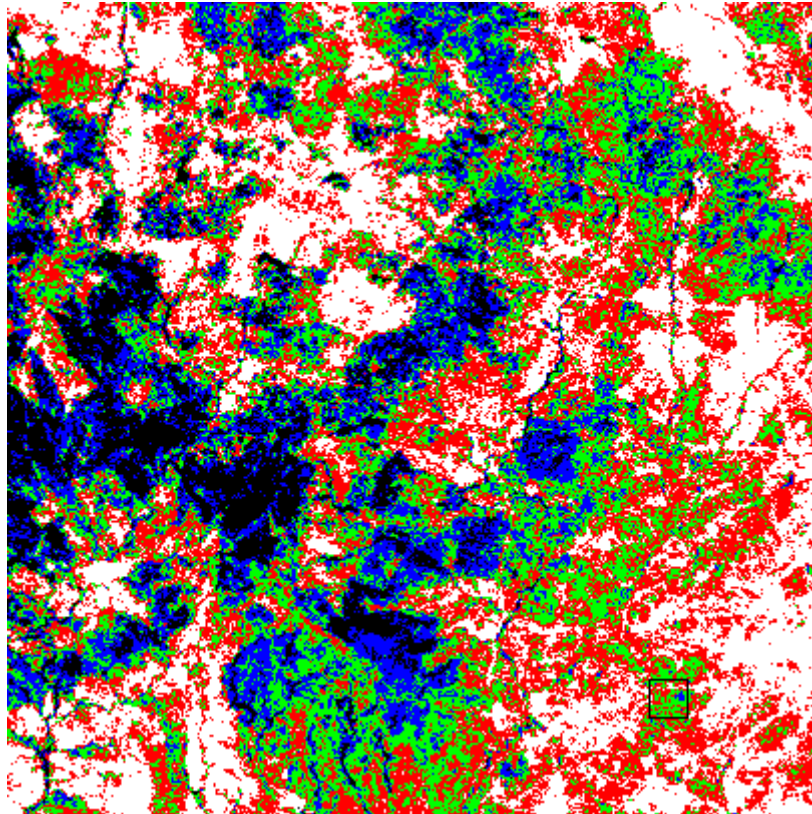


Figure 4.5: Percentage tree canopy cover determined from Landsat 5 TM data taken on August 15, 1995. Colour code: black: 80 – 100%; blue: 60 – 80%; green: 40 – 60%; red: 20 – 40%; white: 0 – 20%. The picture shows a region of 12 × 12 km² of the Evora site. The position of the tower is marked in the lower-right corner. Figure based on data kindly provided by Dr. Carreiras ([Carreiras et al., 2006](#)).

4.5.2 Ikonos

The Ikonos scene at the Evora site was acquired on the June 30, 2005 at 11:23 GMT in four spectral channels: 445 – 516 nm (Blue), 506 – 595 nm (Green), 632 – 698 nm (Red), and 757 – 853 nm (NIR) with spatial resolution of 4 m. One panchromatic channel with spatial resolution of 1 m is available as well. For the analysis the image subset of 12 × 12 km² (the same as for Landsat) was used (Figure 4.6).



Figure 4.6: Ikonos scene (June 30, 2005, 11:23 GMT, 12 × 12 km²) of the Evora site with the Evora tower marked with a red square. RGB composite with green representing NIR band, so that vegetation is marked with intensive green.

Analysis of the Ikonos data was carried out in terms of classification based on area segmentation (eCognition, Definiens Imaging). First the segmentation was carried out on a large scale (scale parameter 200) over all spectral bands. A subset of the segment outlines is shown in Figure 4.7. This scale parameter allows detection of clouds and water bodies.

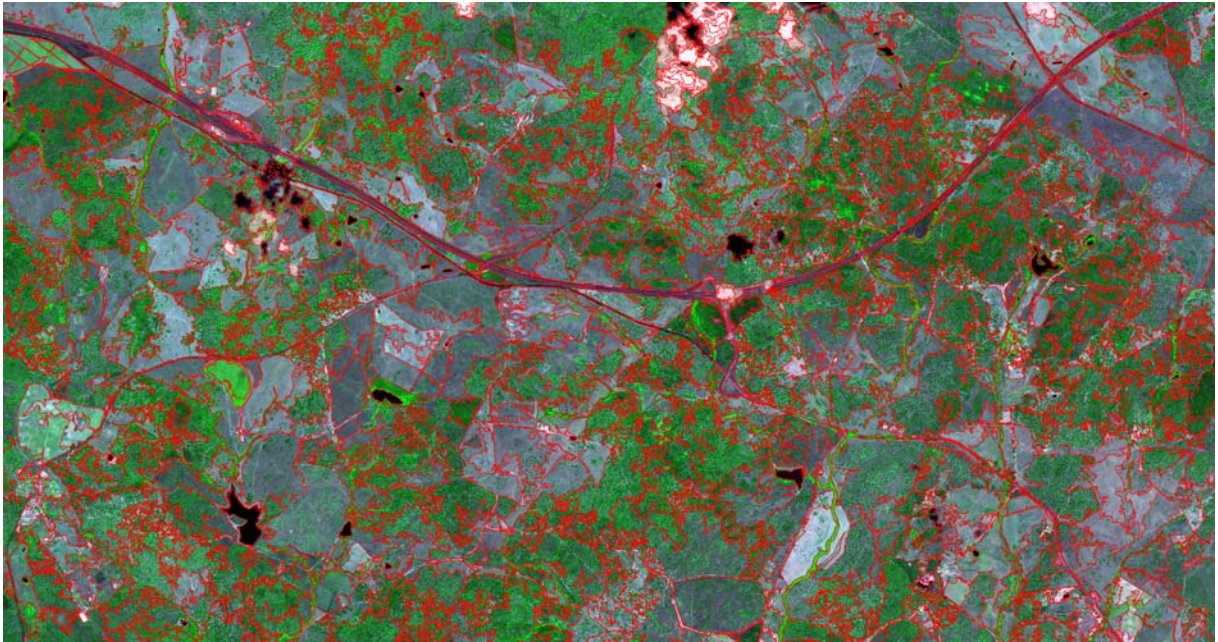


Figure 4.7: Northern part of the Ikonos scene with outlined segments (scale parameter 200). At this scaling level water bodies, clouds and irrigated fields are clearly recognisable.

In the second path smaller segments were created (scale parameter 20) involving only Red and NIR spectral bands which are most suitable for recognition of vegetation. Figure 4.8 depicts the segment outline at this level. The size of the segments (i.e. the scale parameter) was adjusted to the size of one separate tree or group of trees. At this resolution separate trees or groups of trees are lumped within one segment. At the resolution of 4 m shadows from the trees are undetectable. Water bodies and clouds are classified in the previous step.

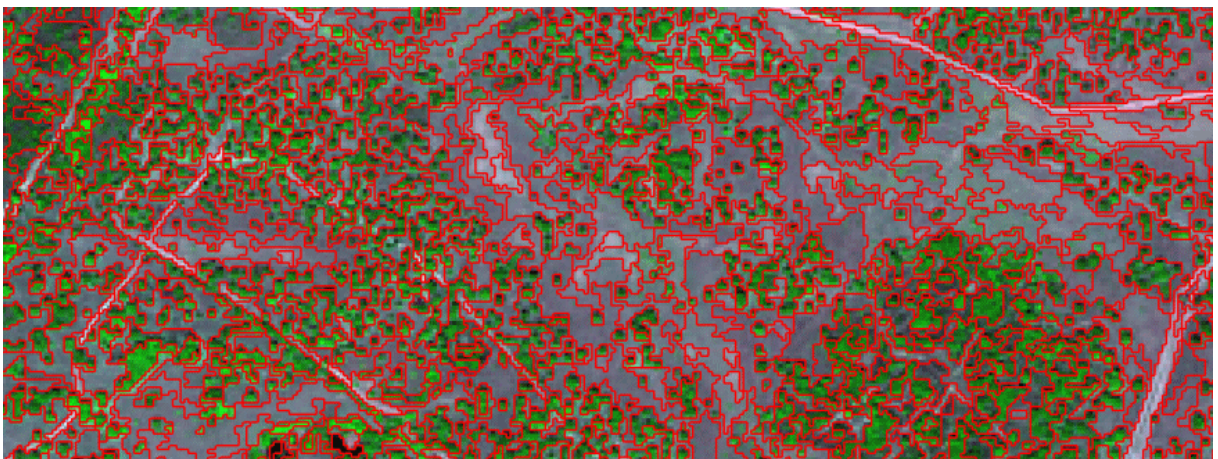


Figure 4.8: Typical subset of the Ikonos scene using small segments (scale parameter 20) for encompassing single trees or group of trees.

In order to reveal the fraction of tree canopy cover, the vegetation index NDVI is used:

$$NDVI = (NIR - Red) / (NIR + Red) \quad Eq. 24$$

The mean NDVI value in each segment was used for its assignment to the vegetation class according to a user defined membership function (fuzzy classification). The membership function depicted in Figure 4.9 was chosen. The results of the classification are shown in Figure 4.10.

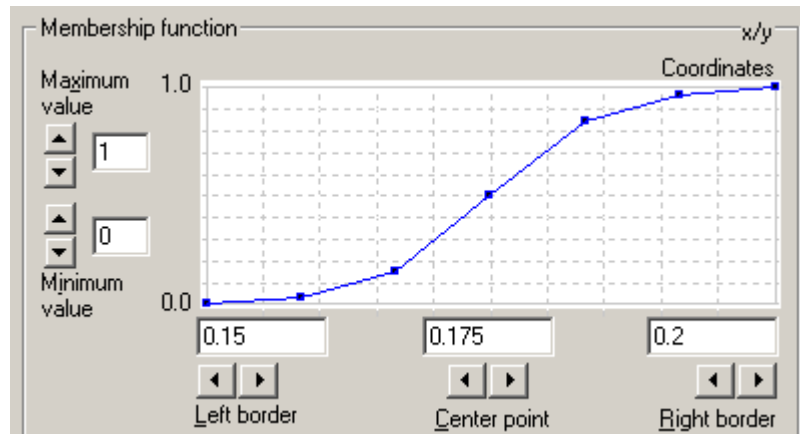


Figure 4.9: User defined function of vegetation index (NDVI) for segments obtained with scale parameter 20 of the Ikonos scene shown in Figure 4.6. Segments with mean NDVI values larger than 0.2 are classified as vegetation, while those with NDVI values in the range 0.15 – 0.2 are classified as vegetation with probability defined by the membership function.

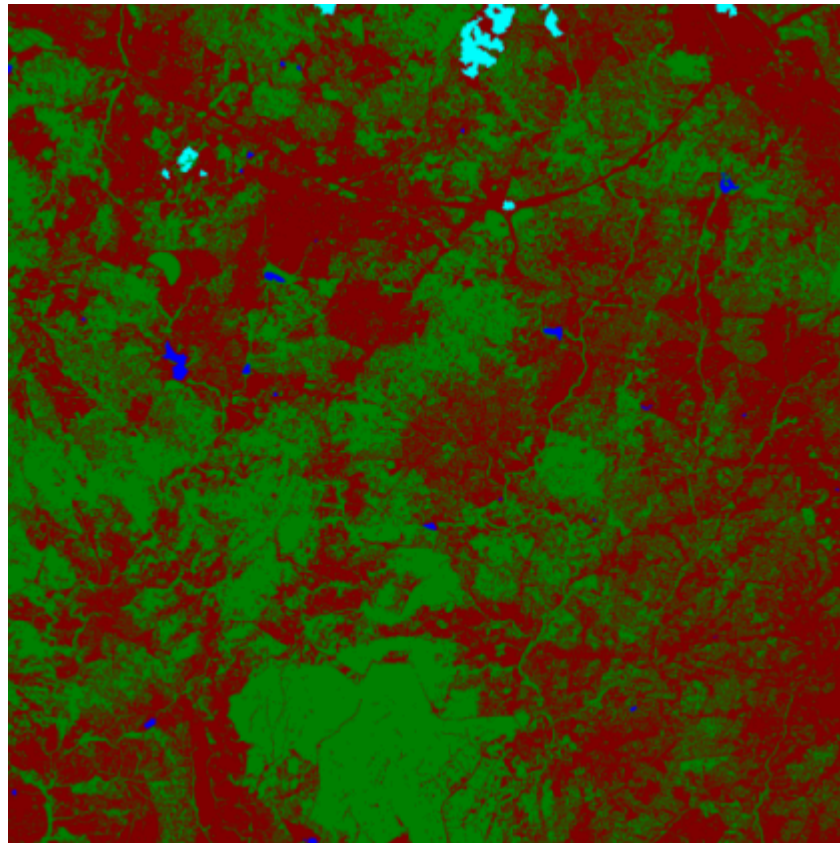


Figure 4.10: Ikonos scene after classification using NDVI. The information about clouds and water bodies was copied from the previous classification on the first level.

The total area of the Ikonos scene encompasses $12 \text{ km} \times 12 \text{ km} = 144 \text{ km}^2$ of which 0.6 km^2 is occupied by clouds (0.4%). Excluding cloud regions the area assigned to each class is summarised in Table 4.1.

Class	Area [km ²]	Area [%]
Vegetation	67.3	46.9
No vegetation	75.8	52.9
Water	0.3	0.2
Sum	143.4	100

Table 4.1: Area of cloud-free pixels for each class determined for the Ikonos scene shown in Figure 4.6.

The area fraction of the vegetation region is 47% of which irrigated green farmlands comprise 0.9%. The farmland is a season dependent, but insignificant contribution to the surface temperature of the site reported by the MSG. Industrial areas such as roads and buildings comprise 1.9% of the area classified as ‘No vegetation’. They are assigned to this class because they have similar temperature as the open areas between the trees. The area of water bodies is not significant regarding the size of the scene (0.2%).

The area fraction of the Evora site covered by trees as obtained by this method (47%) appears quite high. The many separately dispersed trees make it very difficult to measure their area on a pixel based image with resolution of four meters. Round structure of tree crowns results in many mixed pixels on the edges tree-grass. Furthermore, field investigation has revealed that many trees at the validation site are partly transparent. Considering round segments in the classification used for Ikonos images this transparency could not be taken into account.

In summary, studies of the Ikonos data confirm sufficient homogeneity of the Evora region to serve as a validation site, but are not suitable for estimating the tree crown area fraction and its error.

4.6 Instrumentation of the validation station for LST

Experience gained from extensive work at the Australian field sites has strongly influenced the set-up and instrumentation of the Evora ground station. The equipment was provided by the Institute of Meteorology and Climate Research (IMK) at the Forschungszentrum in Karlsruhe (FZK) and the Australian cooperation partner (CSIRO). The following instruments were installed at the LST validation station:

1. A rotating infrared radiometer (Rotrad, 8 – 12 μm) to assess the thermal directional properties of the field site. It is the core instrument of the station.

2. A second infrared radiometer (KT15.82, Heitronics) placed at the same height and in the same viewing orientation as the first one.
3. Two sets of standard instruments for measuring air temperature, relative humidity, wind speed and direction above the ground in the canopy and above the tree crowns.
4. Upward-looking pyrgeometer to measure the downward flux of longwave (3 – 100 μm) radiation.
5. Upward-looking pyranometer to measure the downward flux of shortwave (0.3 – 3.0 μm) radiation.
6. A sunshine sensor to measure the cloudiness at the site.

The Rotrad was later replaced by a set of three KT15.85 (Heitronics) fixed mounted radiometers.

4.6.1 Rotating radiometer (Rotrad)

This radiometer was designed and built by John Bennett, CSIRO, Marine and Atmospheric Research, Aspendale, Vic 3195, Australia. The rotating radiometer, abbreviated Rotrad, was specially designed for the Evora site conditions. The instrument is shown in Figure 4.11. The radiometer head is placed in the centre of the housing on the rotating platform. It is able to rotate about an axis perpendicular to the viewing direction (Figure 4.12). This allows the radiometer to make measurements at varying angles.



Figure 4.11: Rotating radiometer with two black bodies for self calibration (designed by John Bennett, CSIRO).



Figure 4.12: Radiometer sensor on the rotating platform.

The instrument calibrates itself automatically during each sequence of measurements by recording the radiance emitted from the black bodies. The temperatures of the black bodies are slightly different. The first one, called hot black body (HBB), is kept at 42°C during the measurements. The second one, called ambient black body (ABB), assumes the temperature of the surroundings. In each sequence of measurements the sensor is directed towards the HBB and ABB for calibration. After that the measurement of the radiative sky temperature takes place followed by the ground measurements in three different directions. The sensor rests at each direction and carries out a fixed number of measurements at a fixed sampling rate. The median of these measurements is retained for each direction of the sensor. Each median thus obtained is proportional to the incoming radiance minus radiance from the instrument housing. The unknown conversion factor is obtained from the thermodynamic temperatures of HBB and ABB and their corresponding median values from the instrument. The thermodynamic temperatures of the black bodies are measured by independent thermocouples (see Appendix 13.1). Thus at each direction of the Rotrad sensor a radiance is obtained that can be converted to brightness temperature (see chapter 3.3). The accuracy of the radiometer is 0.2 K which is sufficient for the LST validation.

The thermopile of the radiometer is very broadband and the effective spectral range is regulated by a Tasco filter (Tasco Japan Co. Ltd.). The Tasco filter function is shown in Figure 4.13. The Tasco spectral band ranges from 8 to 12 μm (full width at half maximum, FWHM) and thus covers the split-window channels of the SEVIRI satellite sensor (see Figure 3.2).

The opening angle of the detector is 10°. Thus, the diameter of a target seen by the instrument is about 1/6 of the target distance from the sensor. Further technical details are described in Appendix 13.1.

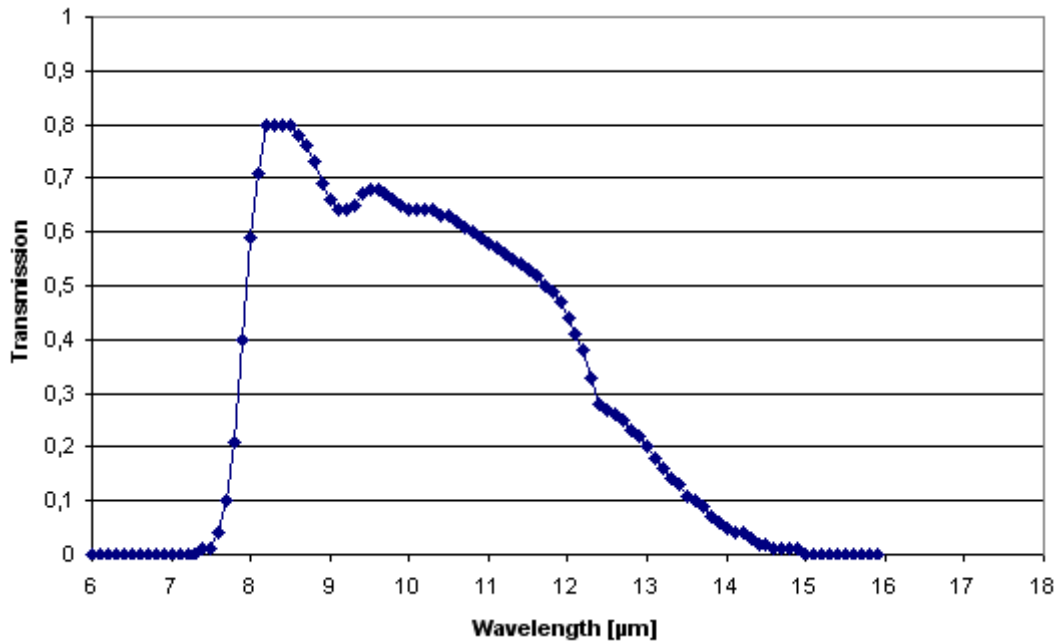


Figure 4.13: The combined spectral response of the TASCO THI-500L detector window and lens filter (taken from [Donlon et al., 1998](#)).

4.6.2 Radiometer KT15

The radiometers KT15.82 and KT15.85 are commercial products from Heitronics Infrared Messtechnik GmbH Wiesbaden, Germany (<http://www.heitronics.de/>). Detailed specifications of the instruments can be found in the user and technical manuals.

Temperature resolution in the range around 20°C is 0.5°C for KT15.82 and 0.4°C for KT15.85 with a minimum measurement time of 1 s. Both radiometers have the same accuracy that depends on the estimated emissivity of the object to be measured. After a warm-up period of 15 min the standard deviation of the measurement is 0.5°C plus 0.7% of the temperature difference between the housing containing the measuring instruments and the object to be measured.

The spectral response functions of the KT15.82 and KT15.85 are shown in Figure 4.14 and Figure 4.15, respectively.

Unlike the KT15.85 the spectral range of the KT15.82 radiometer includes parts of the CO₂ absorption band above 13 µm. In this spectral range the measured radiance refers to the ambient air temperature rather than to the ground temperature. However, transmission at wavelengths above 13 µm occurs only in a small fraction of the filter window. The relative change in radiance due to CO₂ absorption can be calculated using Eq. 6. If ΔT denotes the difference between air and ground temperature T this relative change is $0.046 \times \Delta T/T$. The factor is the ratio of the radiance in band range 13 – 17 µm to the radiance in the whole filter spectral range (7 – 17 µm). Using Eq. 30 this leads to an estimated error of $0.046 \times \Delta T$ due to the CO₂ absorption effect. For $\Delta T = 10^\circ\text{C}$ the error is below

the temperature resolution of 0.5°C of the instrument as specified by the manufacturer.

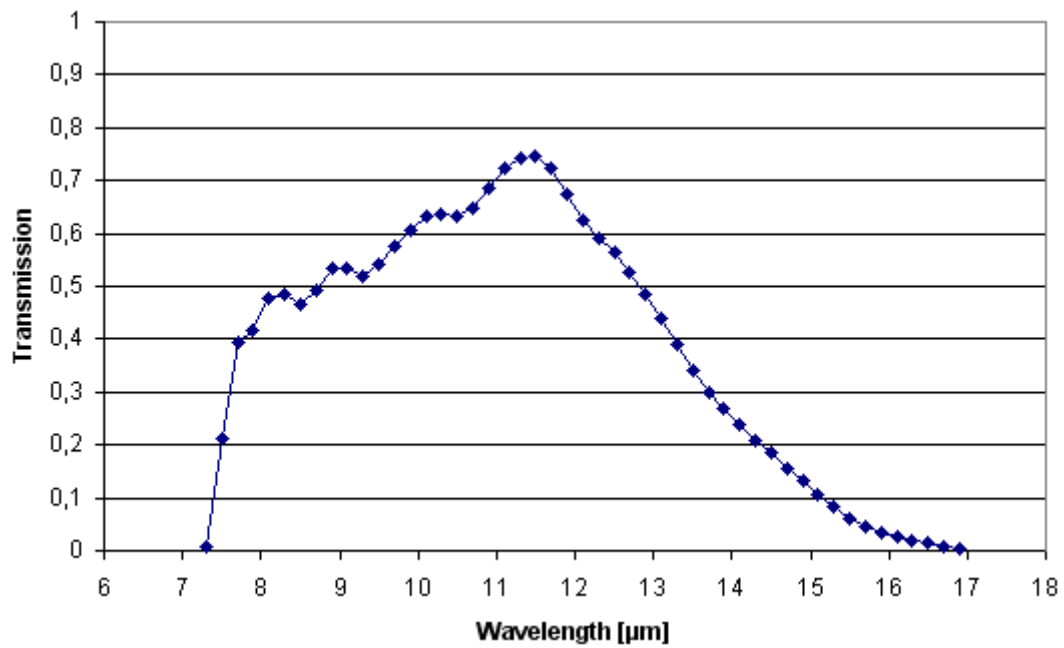


Figure 4.14: Spectral response function of the KT15.82 pyrometer (graph adopted from manufacturer Heitronics Infrared Messtechnik GmbH Wiesbaden, Germany). Although surface leaving radiance at wavelengths above 13 μm is absorbed by CO₂ the resulting contamination of the ground temperature measurements is below the instrument's accuracy.

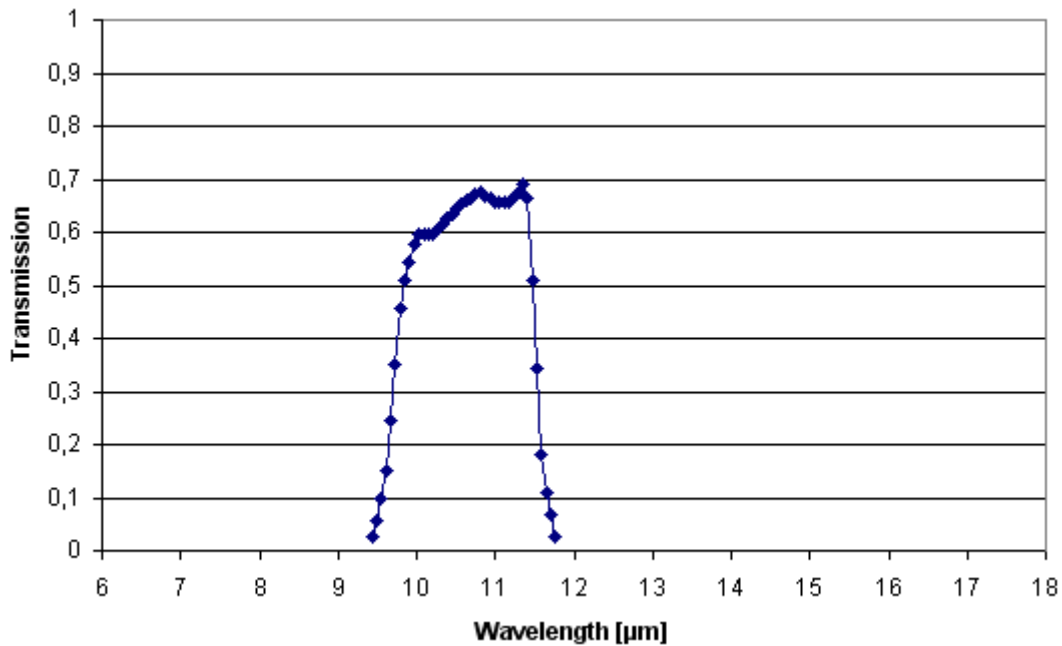


Figure 4.15: Spectral response function of the KT15.85 pyrometer (graph adopted from manufacturer Heitronics Infrared Messtechnik GmbH Wiesbaden, Germany).

4.6.3 Standard meteorological equipment

Air temperature and relative humidity are measured using HMP35 probes (Vaisala, <http://www.vaisala.com/>). Air temperature is measured with a resistance thermometer (Pt100) and relative humidity with HUMICAP H-sensor. Both sensors are placed together in one case, outputting air temperature in °C and relative humidity in % with resolution of 0.2%. The accuracy of the air temperature depends on the relative humidity. The response time equals 15 s and long-term stability of the instrument is better than 1% relative humidity per year. Wind speed [m/s] and wind direction (360°, north at 0°) is measured with a combined sensor manufactured by Theodor & Friedrich (<http://www.th-friedrichs.de/>).

4.6.4 Upward-looking pyrgeometer

Upward-looking infrared radiometer is used for the measurements of the incoming longwave radiation of the atmosphere (model PIR, Eppley Laboratory, Inc., USA, <http://www.eppleylab.com/>). This pyrgeometer measures radiation in the spectral range from 3 to 100 μm for a hemisphere. The instrument outputs two values: a resistance and a voltage.

The housing temperature T [K] is determined from the resistance of the case thermistor across pins D & E according to equation:

$$T = \frac{1}{0.0010295 + 0.0002391 \times \ln(R) + 0.0000001568 \times \ln^3(R)} \quad \text{Eq. 25}$$

Dimensions of the expansion coefficients are 1/K, R is the resistance in multiples of one Ω . Note that the instrument outputs resistance in k Ω , so conversion to Ω is essential.

The net radiation R_{net} at the thermopile is determined by the output voltage V_{ac} across pins A & C after division by the sensitivity S. The instrument specific value for the sensitivity was specified by the manufacturer as $S = 3.99 \times 10^{-3}$ [mV/(W/m²)] (certificate August 11, 1995). R_{net} is typically a negative value as the instrument's case is generally warmer than the atmosphere. The incoming radiation from the atmosphere is thus given by

$$R_{in} = R_{net} + R_{out} = \frac{V_{ac}}{S} + \sigma T^4 \quad \text{Eq. 26}$$

R_{out} is given by the Stefan-Boltzmann law with housing temperature T.

In order to make the voltage signal less sensitive to noise on its long distance to the datalogger it is amplified to yield $V'_{ac} = 1722.3 \times V_{ac} - 7.6975$.

4.6.5 Upward-looking pyranometer

Solar radiation in the spectral range from 0.3 to 3 μm is measured for a hemisphere with a pyranometer (model EP09 Middleton Solar, Australia, <http://www.middletonsolar.com/>).

The irradiance ranges from 0 to 2000 W/m² with signal output of 1.0 mV per W/m². The instrument is able to detect differences in solar radiation as small as 1 W/m². Root mean square noise of the signal is less than 0.5 W/m² and the response time is 10 s. Apart from the radiation signal the instrument outputs the housing temperature and a voltage signal of the humidity inside the case for monitoring its working conditions.

4.6.6 Sunshine sensor

Cloudiness is registered in the visible spectral range from 0.4 to 0.7 μm using a sunshine sensor (model BF3, Delta-T Devices Ltd., <http://www.delta-t.co.uk>). The instrument uses seven photodiodes distributed evenly under a hemispherical transparent dome. A special mask is mounted under the dome to guarantee that at least one photodiode is located in shadow.

The instrument updates its output values five times per second (response time 0.2 s). The largest and the smallest photodiode readings are converted to the final outputs of total and diffuse radiation as well as sunshine status.

4.6.7 Data recording

The Rotrad instrument is directly connected to a laptop via a serial port. It delivers a complete sequence of measurements (see chapter 4.6.1) every

2 minutes; each measurement lasts 2 seconds stopping at each sensor direction for 20 seconds.

The output from all other instruments is logged every 10 minutes on a datalogger (Campbell Datalogger 21X) using communication software PW208 ([PC208W Version 3.3 Datalogger Support Software, User Guide, 2001](#)). The recorded data are mean values from all measurements taken within the past 10 min. The description of the logger output file is given in Appendix 13.2.

The data are downloaded regularly via ISDN telephone line to FZK. The same line allows complete remote control of the laptop.

4.7 Initial measurements at the institute in Karlsruhe

The exact alignment of a radiometer at the field site is not an easy task. A target at a temperature well below ambient temperature placed at the centre of the field of view of the instrument was expected to solve this problem. We used a thin aluminium plate which has a very low emissivity (5%) in the infrared range (8 – 14 μm). In an out-door experiment the aluminium plate reflected the sky radiation which corresponds to an apparent temperature around -40°C and was clearly detectable in the radiometer's field of view (Figure 4.16).

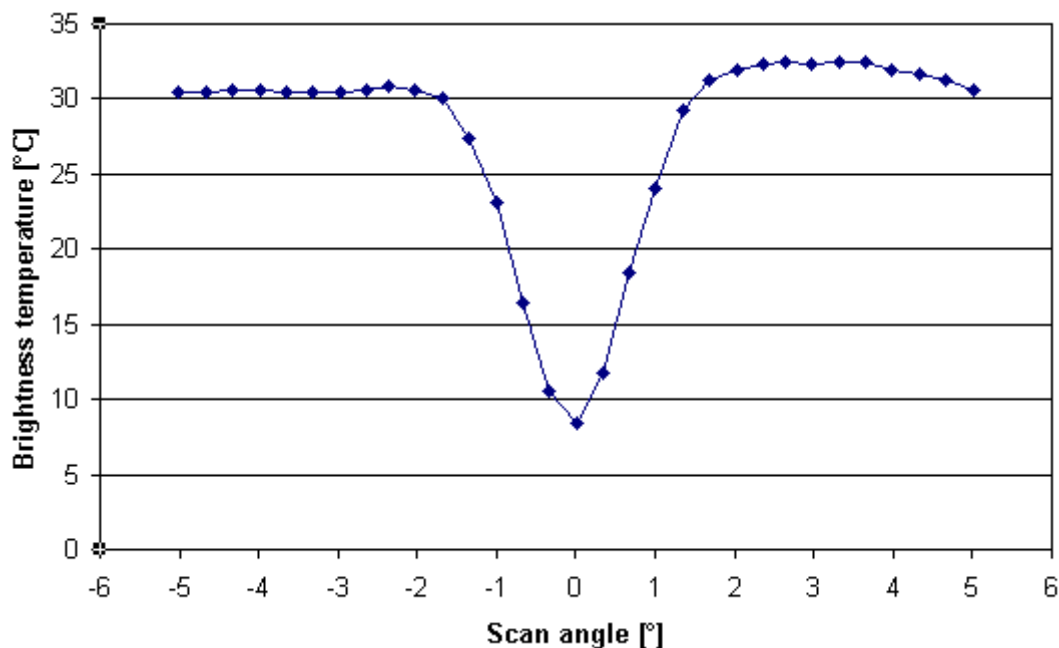


Figure 4.16: Surface brightness temperature scanned with KT15.85 D and scanner SC12. The aluminium plate can be easily recognised in the middle of the scan line as it reflects radiation from the cold sky. The area of the aluminium plate is $0.5\text{ m} \times 0.5\text{ m}$, the field of view of the radiometer is a circle of 1 m diameter.

At the Evora site this method was of limited success. Because of the much larger field of view of the radiometer an excessively large aluminium plate would be required. Moreover, the aluminium plate would also reflect radiation from

nearby trees. Ultimately, we used geometrical relationships for the alignment of the instrument.

4.8 Implementation of the LST validation system

The station was set up on the Evora tower in April 2005. To protect radiometers from getting too hot they are put into an aluminium shell, painted white for maximal reflectivity of shortwave radiation. HMP35 (chapter 4.6.3) is commonly put in a special white shelter with parallel openings around, so that fresh air temperature and humidity measurements in shadow are assured (Figure 4.18 and Figure 4.19). Control unit shown in Figure 4.17 has a closed inner box to protect against dust and insects. A second housing allows ventilation of the inner box that is in the shadow of the outer. Therefore, laptop, modem, telephone system and datalogger are well protected.



Figure 4.17: Control unit of the station. A white painted protecting case contains the datalogger, laptop and outlets of the power supply to all instruments.

Temperature/humidity sensor together with combined sensor for wind speed and wind direction were mounted in the lower level of the tower to provide reference values of the air conditions in the vegetation, as it is shown in Figure 4.18. These measurements are relevant for the LST validation station, as air condition above the ground is closely related to the surface temperature.

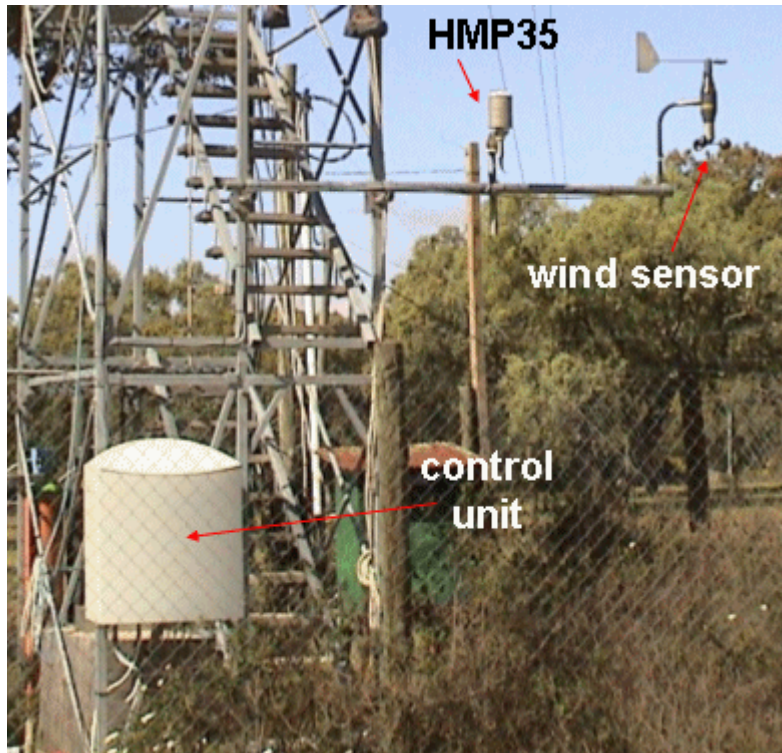


Figure 4.18: The foot of the tower with control unit and sensors for air temperature, air humidity, as well as wind speed and direction.

On the top of the tower well above the trees with free view to the horizon a pyrgometer (chapter 4.6.4), a pyranometer (chapter 4.6.5), and a sunshine sensor (chapter 4.6.6) are mounted. A HMP35 (chapter 4.6.3) completes the instrumentation (Figure 4.19). The wind on top is measured with an ultra-sonic anemometer as part of the CO₂-flux station.

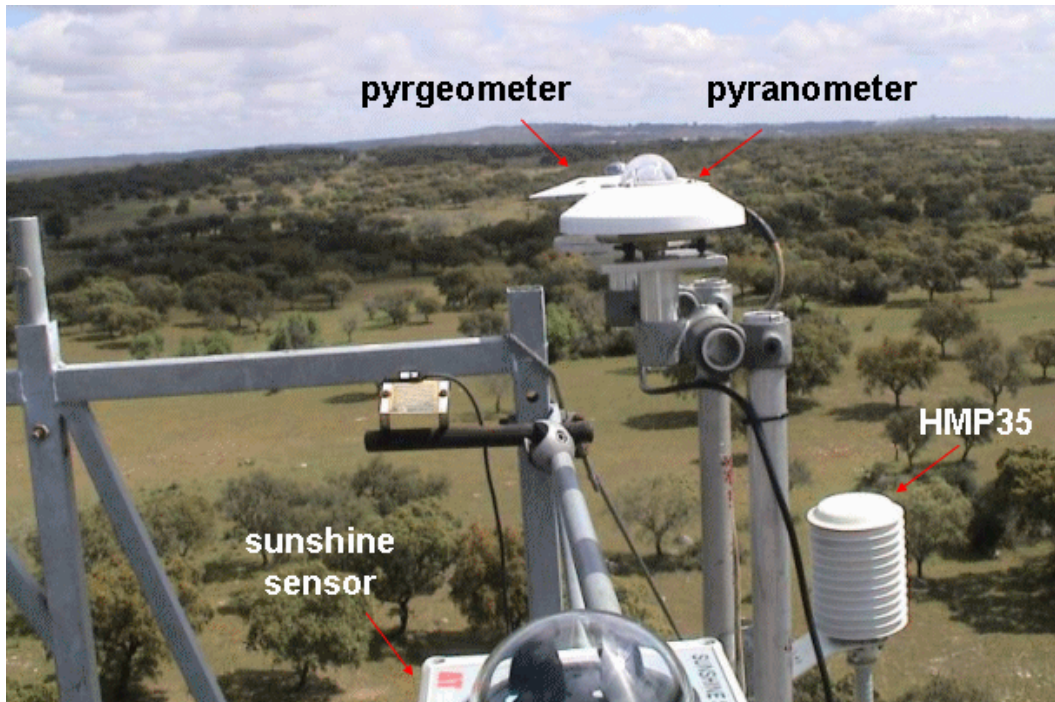


Figure 4.19: The instrumentation mounted on the top of the tower (28 m above the ground) for measurements of solar and terrestrial fluxes. Air temperature and humidity is monitored at this level as well.

The radiometers are mounted 23 m above the ground (Figure 4.20) and oriented in the same direction as seen by the MSG satellite (essentially pointing to the north). The Rotrad measures one spot on a tree and two on the ground. The Rotrad sky view is directed towards MSG (see internal geometry of Rotrad in Figure 13.1 and instrument mounting in Figure 4.21). The Rotrad sky view is adjusted to 40° from zenith. The optimal 53° angle from zenith, the best approximation for measuring of hemispherical atmospheric downward radiation by the directed radiation measurements ([Kondratyev, 1969](#)), was not available because of technical limitations of the instrument. Error analysis has shown that even high uncertainties in sky temperature are of small influence on the resulting surface temperature (chapter 5.7).



Figure 4.20: The main instruments of the station: Rotrad and KT15.82 mounted 23 m above the ground that enables measurements over the tree canopy. Both instruments are tilted, so that the construction of the tower is not in the field of view of the radiometers.

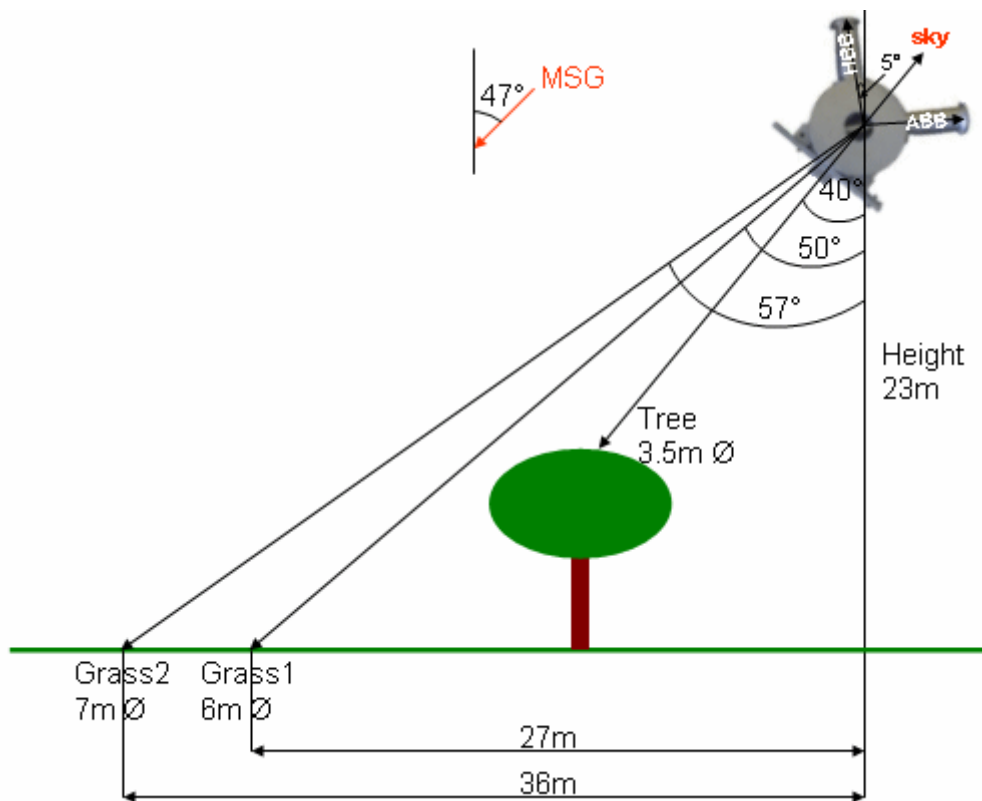


Figure 4.21: Schematic drawing of the Rotrad measurements.

Figure 4.22 shows the measurement targets as they are seen by the radiometers from the tower (schematic circles). Depending on the time of the day (and the year season) the grass spots are totally or partly in the shadow of trees (Figure 4.23). The direction of measurements was chosen to coincide with the satellite's viewing angle to minimize systematic discrepancies in the temperature determinations. Unfortunately, the distribution of shadow in the measured grass regions may not be representative for the entire Evora site as seen from the satellite. However, the position of the radiometers was fixed by the existing Evora tower which strongly limits the selection of more suitable targets.

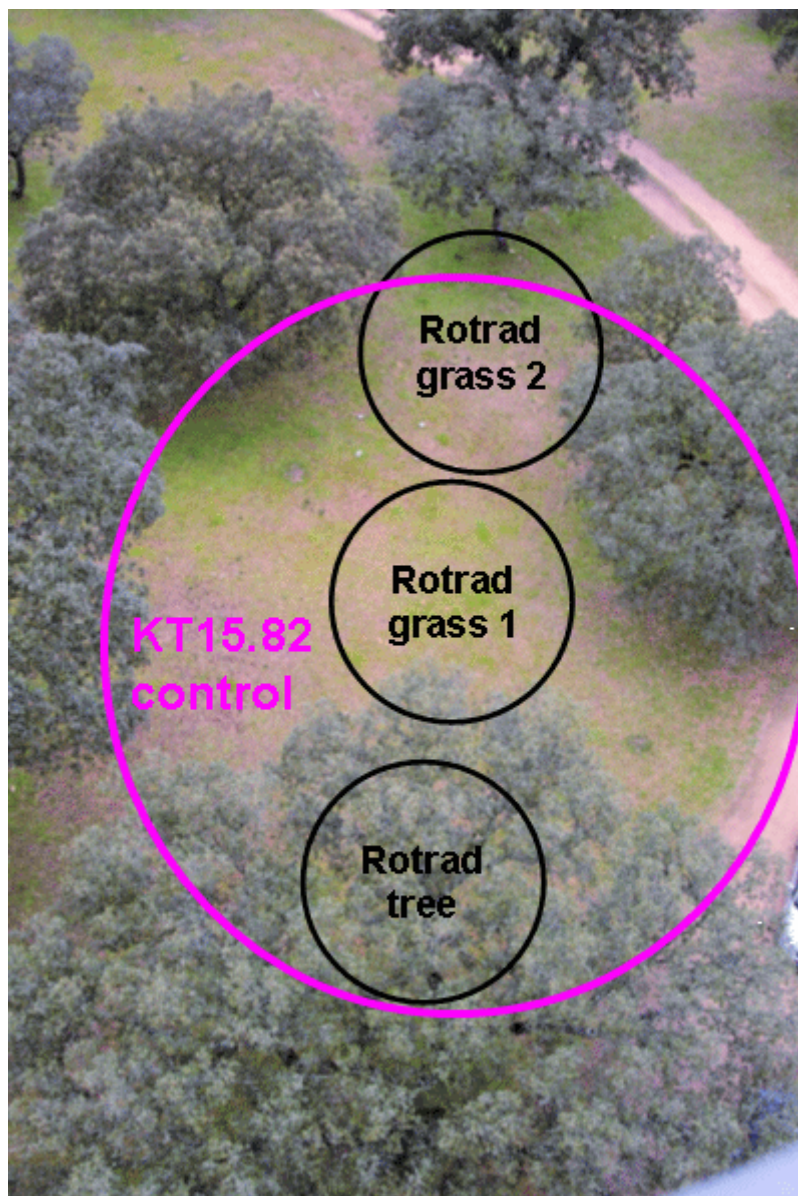


Figure 4.22: KT15.82 control and Rotrad targets ('grass1', 'grass2', and 'tree') at the LST validation site near Evora. The targets are indicated by circles not drawn to scale.



9:30



11:00



13:00



14:00



16:00



17:00

Figure 4.23: Views of the target area seen by the radiometers at different times of August 4, 2005. The viewing direction points to the north. Temperatures in the grass regions are strongly affected by shadows as they move during the day.

For control measurements an additional radiometer KT15.82 is fixed on the Evora tower near the Rotrad (Figure 4.20). The instrument's viewing direction is tilted 45° from nadir and has an opening angle of 31° (lens M6). The target area is roughly centred at 'grass1' and has a diameter of 18 m (Figure 4.22). It includes a mixture of all types of ground cover characteristic for this site: grass in the sun, grass with shadow and tree crowns.

The actual fraction of tree and grass area of the target can be determined with Rotrad. At night this unknown fraction is not relevant because grass and tree regions have very similar temperatures. Measurements from both instruments, Rotrad and KT15.82, are in excellent agreement. For measurements during the day the fraction of tree area matters. A value of 52% for the tree fraction was obtained by regression analysis. The scatter plot between Rotrad and KT15.82 measurements taken over a period of about one year is shown in Figure 4.24. The excellent agreement of these independent measurements (RMS differences equal 0.5°C) proves the internal consistency of the radiometric temperatures collected at the Evora station. Apparently, the KT15 radiometer has a very good long-term stability even without the need of frequent calibration.

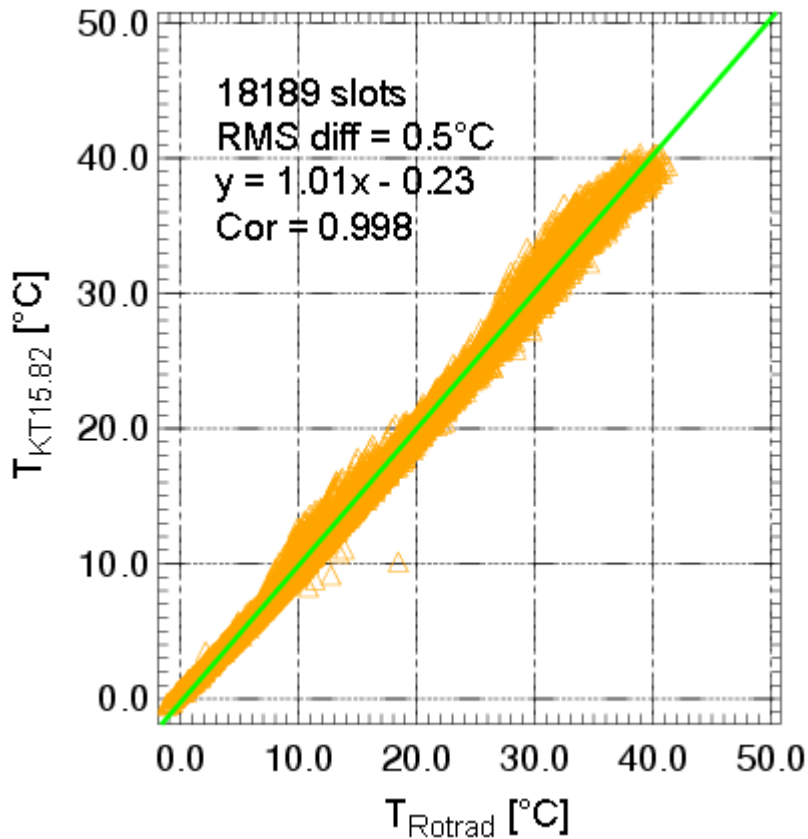


Figure 4.24: Scatter plot of brightness temperatures measured with Rotrad and KT15.82 radiometers. The Rotrad temperatures are the weighted mean of 52% ‘tree’ and 48% ‘grass1’ target regions. The shown regression line has unit slope and almost zero offset.

Due to technical problems in March 2006 the main radiometer Rotrad was replaced by three KT15.85 radiometers. The first radiometer is fixed in the viewing direction marked as ‘tree’ in Figure 4.22. The second one is directed roughly towards ‘grass1’ target region while the third one is pointing to the sky (Figure 4.25). KT15.85 radiometers have an opening angle of 8.5° (lens L6).

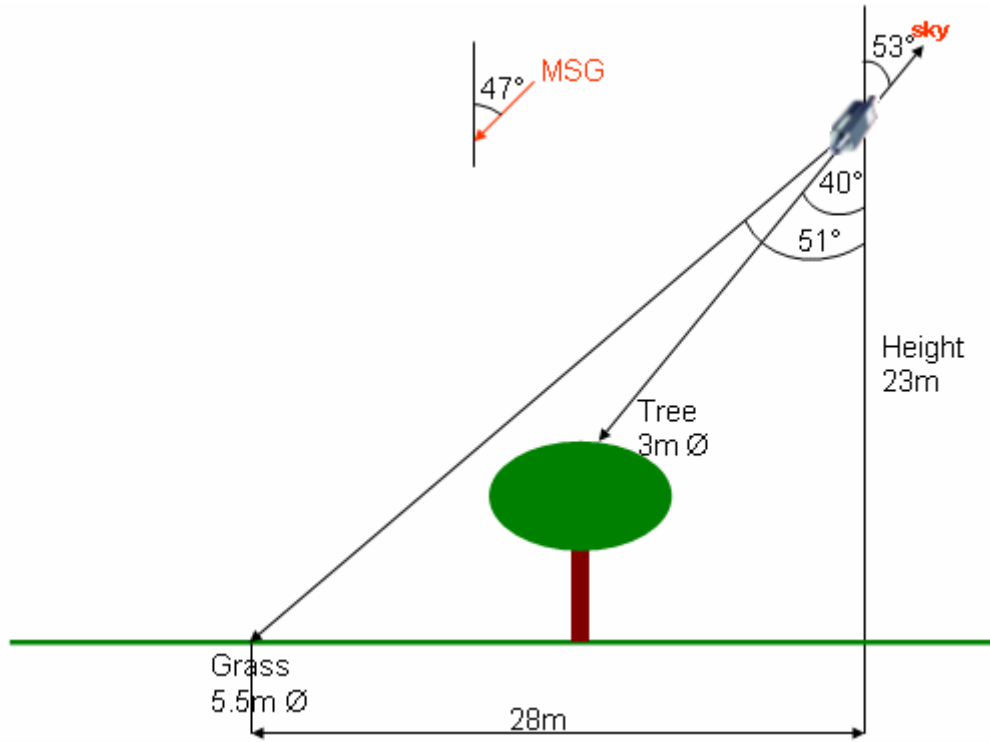


Figure 4.25: Schematic drawing of the KT15.85 measurements.

5 Data collection and preprocessing

The raw data from the ground validation station must be prepared for final comparisons with the satellite observations. This includes resampling, selection of valid data and correction for emissivity. The accuracy of the preprocessed ground-truth data is assessed by detailed error analysis.

5.1 Emissivity of the Evora site

According to Eq. 10 the effective emissivity of the Evora site depends on the temperatures of its land cover elements. The largest temperature differences between the land cover elements occur in summer when the grass is completely dry and resembles soil. Moreover, the emissivity for soil is significantly lower than for green grass during the winter time. According to the UCSB¹ MODIS emissivity library (<http://www.icesb.ucsb.edu/modis/EMIS/html/em.html>) the emissivities within the spectral range of 8 – 14 μm are 0.98 ± 0.01 for green vegetation and 0.95 ± 0.01 for soil. Using Eq. 10 with a tree crown area fraction of 40% (60% soil) calculated emissivities of the Evora site are shown in Table 5.1 for a number of different tree and soil temperatures. Apparently, these emissivities are nearly constant and excellently agree with the approximation of the emissivity given in Eq. 11, which is temperature-independent. Assuming a tree area fraction of 40% the mean emissivity for the Evora site is $\bar{\varepsilon} = 0.96$.

Tree temperature [$^{\circ}\text{C}$]	Soil temperature [$^{\circ}\text{C}$]	Emissivity
5	15	0.96
20	35	0.96
30	50	0.96

Table 5.1: Band-averaged emissivities at the Evora site for various temperatures of its land cover elements calculated using Eq. 10.

Constant emissivities for each pixel covering the Evora site are also used in the calculations of the LST product by the split-window technique. They slightly differ at each adjacent pixel and for each split-window channel as shown in Table 5.2.

¹ University of California, Santa Barbara

Pixel	Channel 10.8 μm	Channel 12.0 μm
1	0.9762	0.9796
2	0.9775	0.9792
3	0.9765	0.9785
4	0.9771	0.9789
mean	0.9768	0.9791
	0.9779	
since October 2006		
1	0.9935	0.9947
2	0.9952	0.9955
3	0.9943	0.9948
4	0.9950	0.9953
mean	0.9945	0.9951
	0.9948	

Table 5.2: Emissivity values for the four pixels covering the Evora site used in the calculations of the LST product by the split-window technique. These values were updated in October 2006.

It appears that the emissivities presented in Table 5.2 are too large for natural surfaces. Nevertheless, we use the mean value of each of the two sets of emissivities (0.9779 and 0.9948) for the ground-truth measurements in order to avoid the influence of different emissivities on the LST validation results. After all, we are mainly interested in verifying the split-window technique used to bypass the complexity of radiative transfer through the atmosphere.

5.2 Ground measurements

Figure 5.1 depicts temperatures observed at the Evora ground station during a typical cloud-free day in June 2006. Air temperatures were measured with HMP35 (chapter 4.6.3) in two different levels (2 m and 28 m above the ground). Brightness temperature of integrated tree crown and grass surface was measured with wide-angle KT15.82 control radiometer (see Figure 4.22). At night surface temperature is very close to near-ground air temperature. However, at daytime

solar radiation is strongly absorbed by the surface which becomes much hotter than the air.

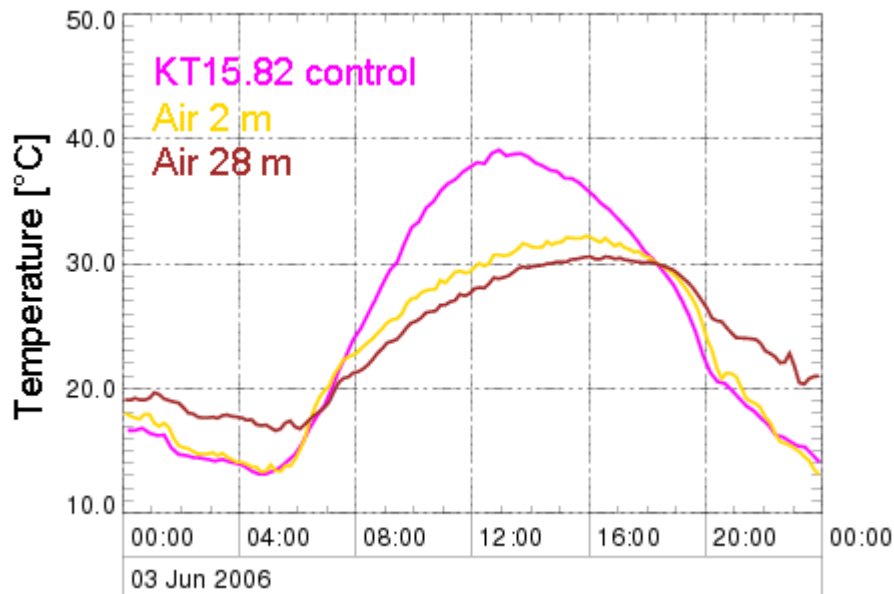


Figure 5.1: Diurnal cycle of air temperatures in 2 m and 28 m height and corresponding surface brightness temperature obtained by the KT15.82 control radiometer.

Separate brightness temperatures of the tree and grass targets (Rotrad, Figure 4.22) are shown in Figure 5.2 together with air temperatures (2 m and 28 m above the ground) of the same day as used in Figure 5.1. As expected the brightness temperature of the tree target (about 8 m high) is close to the near-ground air temperature, but much lower than the temperature of grass at daytime.

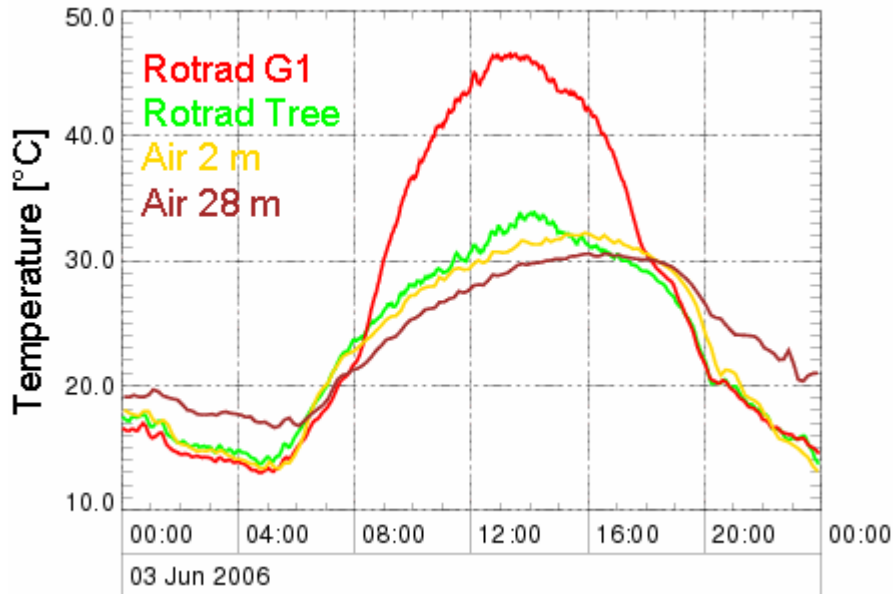


Figure 5.2: Comparison of air temperatures in 2 m and 28 m height with brightness temperature of grass and tree crown measured by the Rotrad. Tree crown brightness temperature is almost the same as 2 m air temperature, whereas 28 m air temperature has lower amplitude of its diurnal cycle.

The typical relationship between relative humidity, air temperature and surface brightness temperature is depicted in Figure 5.3 for April 13–14, 2006. On a cloudy day (April 14) the two air temperatures are similar to the brightness temperature measured by the KT15.82 control radiometer, because the surface is not heated by direct solar radiation. Relative air humidity rises when temperature drops – provided that no exchange of the air mass happens. Close to the surface saturation is reached.

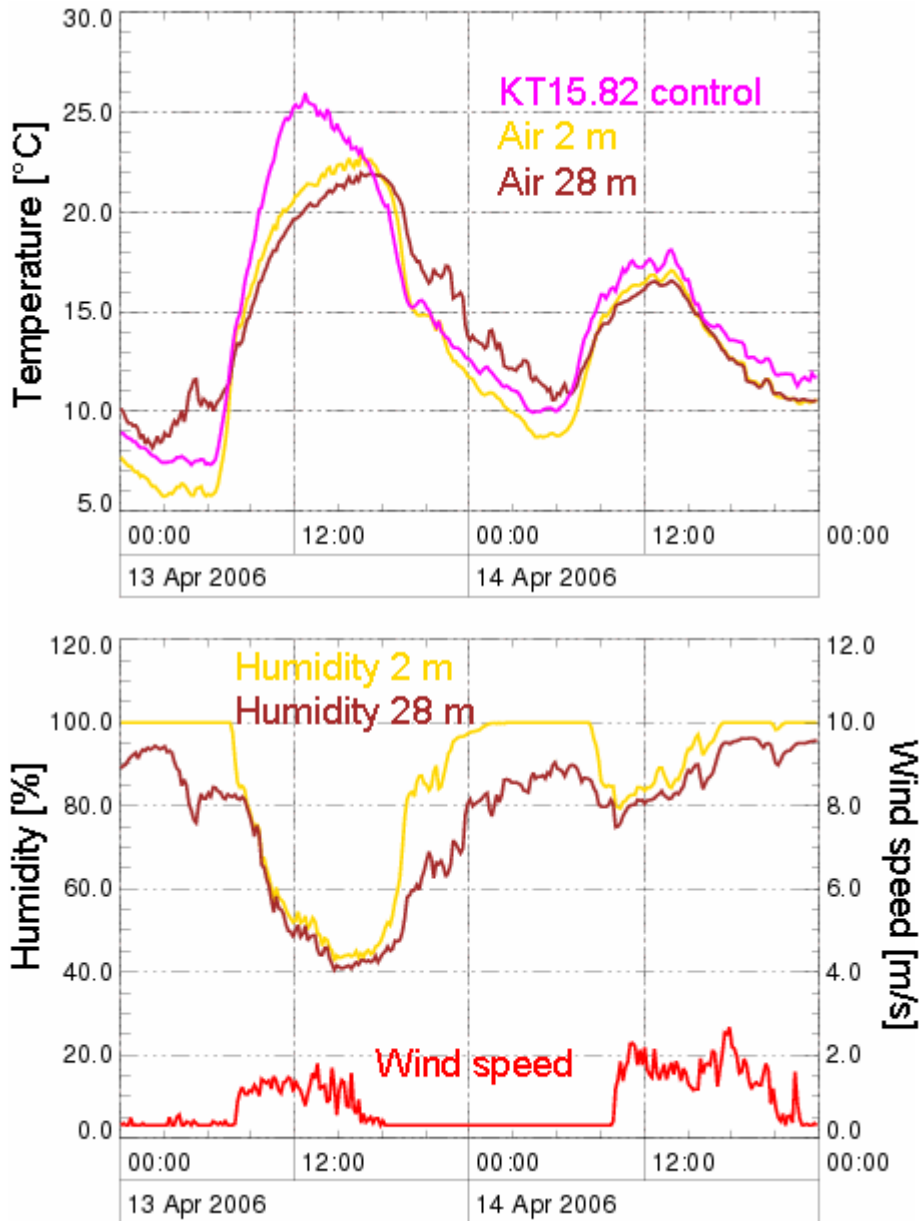


Figure 5.3: Air temperature and relative humidity at the Evora station at two levels (2 m and 28 m above the ground) together with surface brightness temperature (KT15.82 control) and wind speed at 2 m above the ground on two example days (April 13–14, 2006). At night there is almost no wind, but at daytime wind blasts play an important role in the energy exchange between air and surface.

Figure 5.4 shows the standard error in brightness temperature measured by the KT15.82 control radiometer (see Figure 4.22). The errors were monitored during January 7–8, 2006 and sampled in intervals of 10 minutes as delivered by the datalogger. The standard deviations of the measurements are closely related to fluctuations in solar radiation. They rise from 0.1°C during the night to 0.2°C during a clear day, but may increase up to 1.2°C due to temporal cloud cover (7 January) that cause shortwave radiance changes.

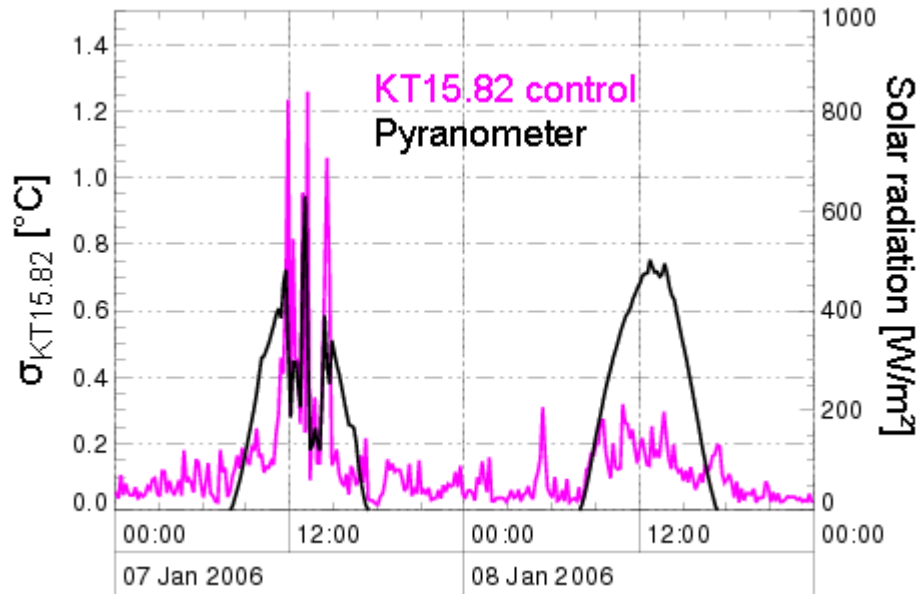


Figure 5.4: Standard deviations of surface brightness temperatures sampled in intervals of 10 minutes (pink line, KT15.82 control radiometer). The increase of standard deviation during daytime is caused by fluctuations in shortwave solar radiation (black line, pyranometer).

An example showing standard errors of control KT15.82 measurements during a cloud free-day followed by a completely cloudy day is depicted in Figure 5.5. Variations in solar radiation during the cloudy day (April 14) do not lead to an increase of the measurement errors.

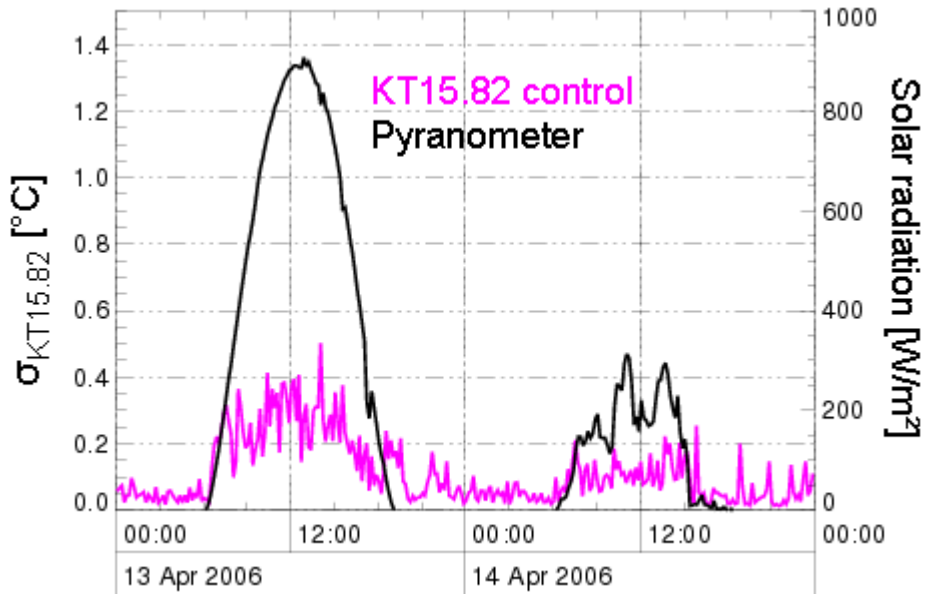


Figure 5.5: Standard deviations of surface brightness temperatures sampled in intervals of 10 minutes (pink line, KT15.82 control radiometer). Fluctuations in shortwave solar radiation (black line, pyranometer) on a completely overcast day (April 14) do not lead to an increase of the errors in surface brightness temperatures.

The standard deviations of Rotrad measurements are obtained every 10 minutes from sampling statistics of the five most recent observations in each target direction (see chapters 4.6.1 and 4.6.7). They are displayed in Figure 5.6 and Figure 5.7 for a cloudy day (January 7, 2006) and a cloud-free day (June 3, 2006), respectively. Apparently, sky brightness temperature varies strongly because of moving clouds which leads to excessively large standard deviations. The standard deviations of the measurements directed towards ground targets are mostly smaller than 1.5°C during daytime. At night the standard deviations are usually smaller than 0.5°C.

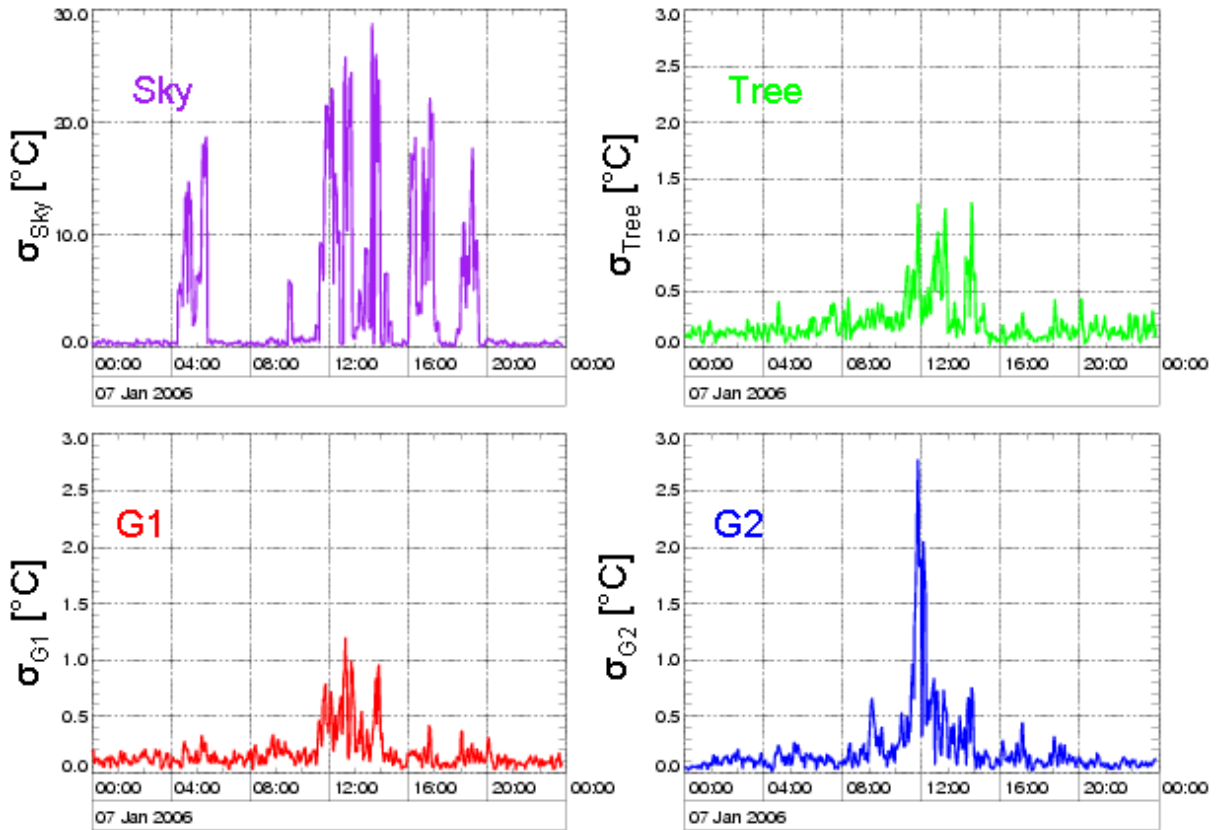


Figure 5.6: Standard deviations of Rotrad brightness temperatures in four target direction for sky, tree (upper) and two grass views (lower) on a cloudy day. Moving clouds are the reason for large standard deviations of sky temperature. Standard deviations are obtained from sampling statistics comprising five consecutive measurements covering a period of 10 minutes. The errors are plotted in steps of 2 minutes which leads to some smoothing effect.

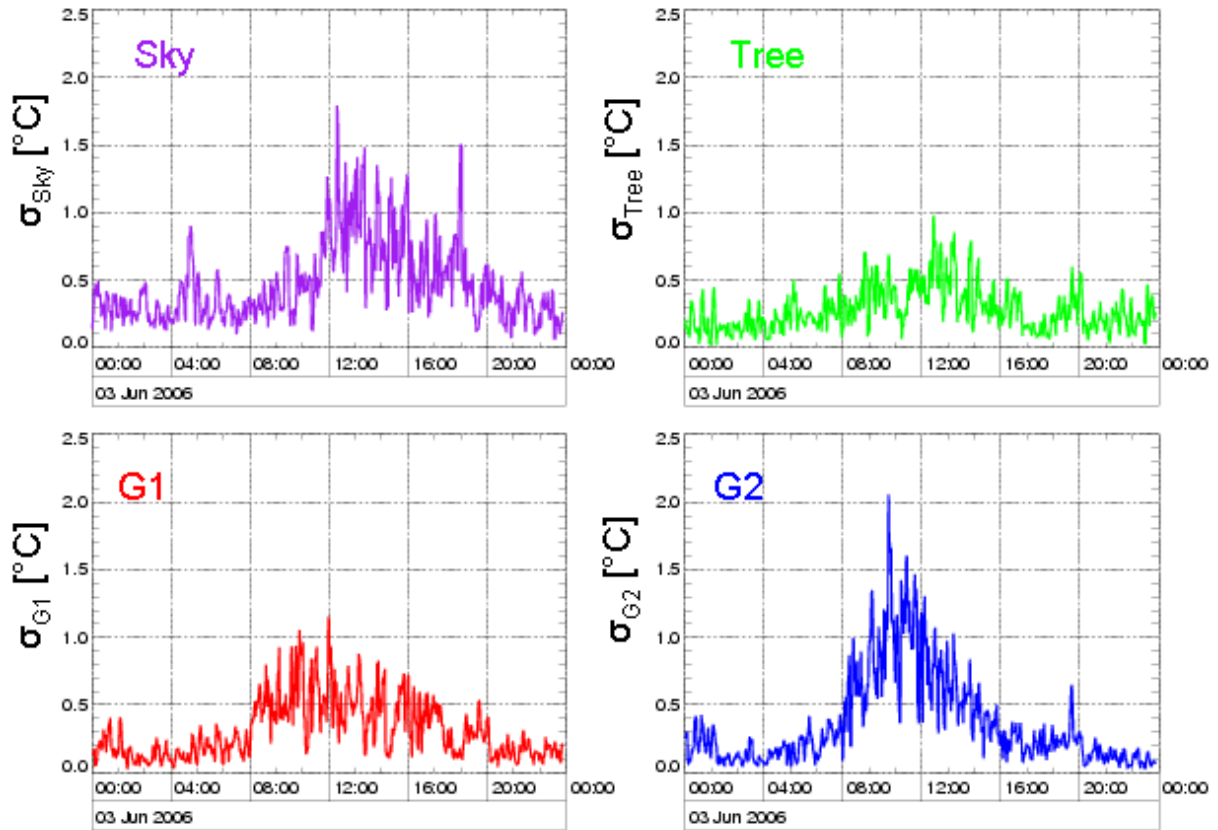


Figure 5.7: Standard deviations of Rotrad brightness temperatures in four target direction for sky, tree (upper) and two grass views (lower) on a cloud-free day. Standard deviations are obtained from sampling statistics comprising five consecutive measurements covering a period of 10 minutes. The errors are plotted in steps of 2 minutes which leads to some smoothing effect.

Figure 5.8 and Figure 5.9 show the flux measurements made with pyrgeometer (chapter 4.6.4), pyranometer (chapter 4.6.5) and sunshine sensor (chapter 4.6.6) at the Evora station on two example days. Solar radiation measurements using the last two instruments detect the presence of clouds very clearly. The solar radiation F monitored on a clear day (April 13) is proportional to the cosine of solar zenith angle θ at the measurement site

$$F = S_0 \cos \theta \quad \text{Eq. 27}$$

as shown in Figure 5.10. The factor S_0 derives from the solar constant (1366 W/m²) at the top of atmosphere which reduces to about 1000 W/m² due to atmospheric attenuations. Deviations between measured solar fluxes and the model are caused mostly by clouds (April 14) and could therefore serve as an additional method for their detection during daytime.

Longwave radiation measured by the pyrgeometer was originally thought to be useful for cloud detection at night. However, this instrument responds more to temperature and humidity changes of the air than directly to the clouds. Hence, these measurements cannot depict cloudy days unambiguously (Figure 5.8).

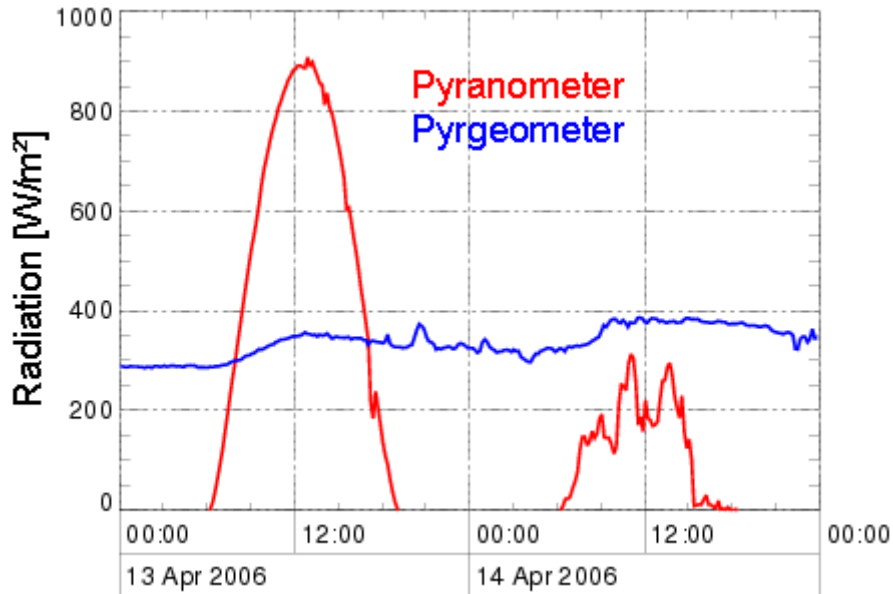


Figure 5.8: Shortwave ($0.3 - 3 \mu\text{m}$, red line) and longwave ($3 - 100 \mu\text{m}$, blue line) downwelling flux measurements at the Evora station. A cloud-free day (April 13) and a cloudy day (April 14) can be easily distinguished by the means of solar flux measurements (red line). The variations in longwave downward fluxes are the effect of the variable humidity and temperature of the air. Thus, these longwave flux measurements are unsuitable for cloud detection.

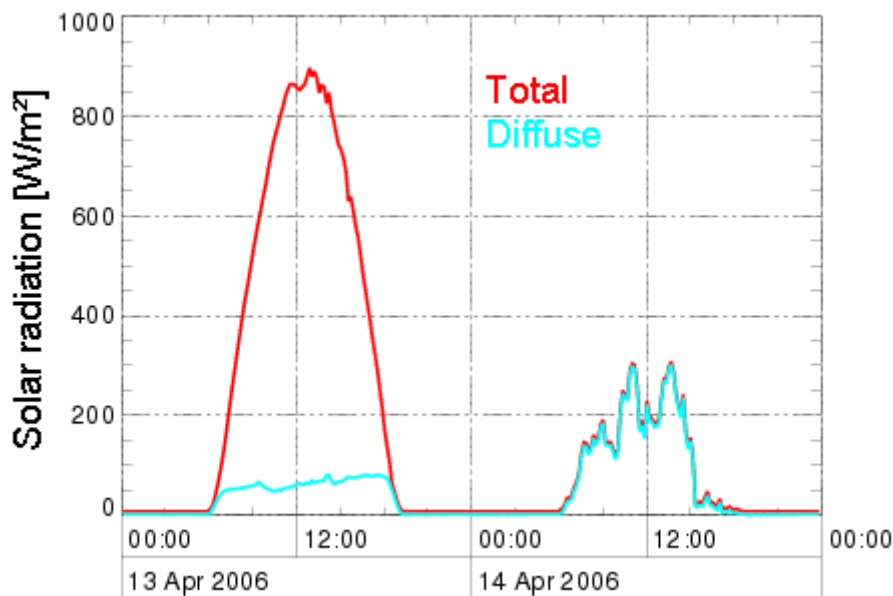


Figure 5.9: Total (red line) and diffuse (blue line) radiation measured by the sunshine sensor in the spectral range $0.4 - 0.7 \mu\text{m}$. The sky is completely covered with clouds if the direct solar radiation equals the diffuse one, as it was on April 14 (cloud detection only possible at daytime).

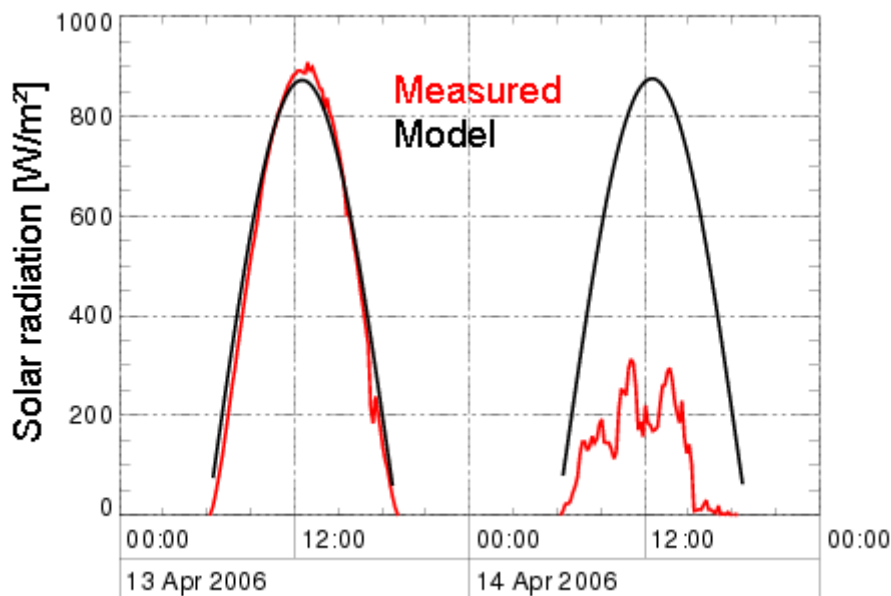


Figure 5.10: Measured (red line, pyranometer) and calculated (black line, Eq. 27) solar radiation reaching the Earth.

5.3 Acceptance criteria for ground data

The absence of clouds is an important precondition for valid surface temperature measurements from satellites. Sky brightness temperature is very sensible to the presence of even thin clouds. On a clear day the sky temperature is almost constant and its magnitude in the 8 – 14 μm spectral range varies mostly with changes in water vapour content. Short-time sky temperature fluctuations are caused by clouds. Radiometric measurements directed towards the sky are expected to reveal clouds on the path between satellite and the Evora site. The presence of clouds is also the major reason of short-term fluctuations in temperature of the ground targets.

Two complementary criteria are used to specify thermally stable ground data suitable for comparison with satellite derived temperatures. The short-term criteria state that standard deviations of radiometric measurements sampled as described in chapter 5.2 should not exceed 2°C for a period of 10 minutes. The long-term criteria are based on the sky brightness temperature distribution for a period of 2 days. A single sky temperature observation exceeding the median of the distribution by more than 5°C is not accepted for the comparison with satellite data. The long-term criteria prevent inclusion of temperature data of low variability when the Evora site is covered by clouds (Figure 5.12).

5.4 Acceptance criteria for satellite data

A set of 2×2 MSG satellite pixels containing the Evora ground station were chosen according to Landsat and Ikonos high resolution images (chapter 4.5). The considered pixels are shown in Figure 5.11. The geographical coordinates

refer to the centre of each pixel and are provided by LSA-SAF (<http://landsaf.meteo.pt/>) separately from the LST product. An address offset error of one pixel along the diagonal has been found in data generated before October 28, 2005. The pixels actually used are specified in Figure 5.11.

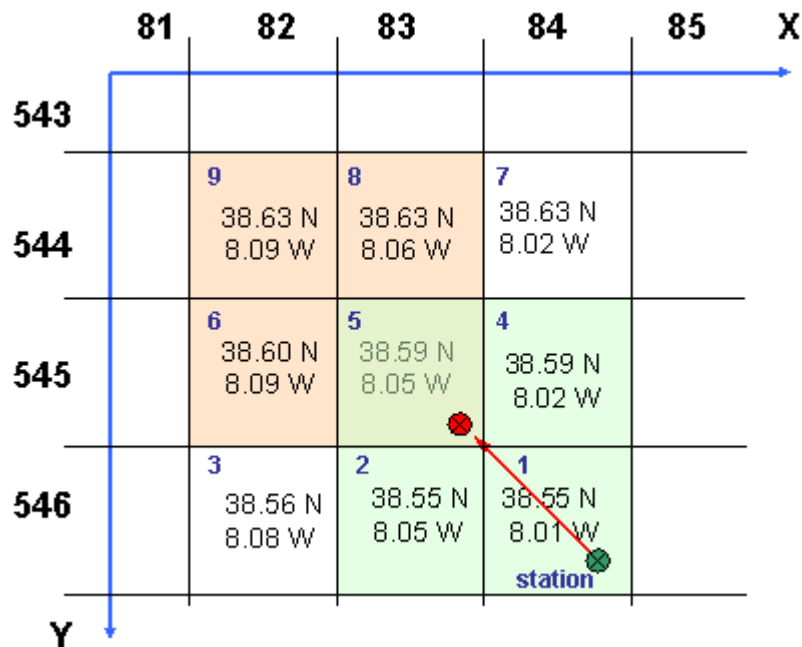


Figure 5.11: A subset of LST-MSG image pixels at the Evora site with X column and Y row number. Each pixel is labelled with its central geographical coordinates. Pixels number 1, 2, 4 and 5 were found representative for station measurements. Pixels 5, 6, 8 and 9 are used in the validation for LST products generated before Oct 28, 2005 in order to compensate a programming error in the LST product.

LSA-SAF project provides land surface temperatures only for cloud-free pixels. These pixels are classified as ‘worse than nominal’, ‘nominal’ or ‘better than nominal’ (chapter 3.8). Due to the homogeneity of the Evora site it is expected that the four MSG pixels have very similar surface temperatures. We use the term ‘MSG slot’ to denote the mean of available LST values from these four MSG pixels observed at the same time. A ‘MSG slot’ is termed ‘consistent’ if the following two conditions are satisfied:

- all four pixels are cloud-free and classified as ‘nominal’ or ‘better than nominal’,
- the estimated standard deviation of the four pixel temperatures is less than 2°C.

A ‘MSG slot’ is accepted in the validation analysis if the following three conditions are satisfied:

- it is internally ‘consistent’,
- it has at least one ‘consistent’ neighbour,

- its temperature differs by less than 3°C from that of any neighbour.

These conditions were tailored to eliminate cloud contaminated pixels as much as possible.

Clouds are frequently observed even in the sunny Evora region of Portugal. Reliable validation requires a completely cloud-free sky over an area of four MSG pixels, i.e. 144 km². Even small cloud contaminations within a pixel cause noticeable decrease in temperature. Despite the attempts to omit cloudy pixels from the distributed LST products, many unrecognised cloudy MSG pixels remain. This problem is depicted in Figure 5.12. In this example LST of ‘MSG slots’ (pink circles) during 0 to 4 a.m. are up to 10°C lower than the surface brightness temperature measured at the ground station. Furthermore, the sky brightness temperature is very close to the surface brightness temperature, indicating clouds over the validation site. In the afternoon from 2 p.m. the sky temperature drops to -40°C which is characteristic for a cloud-free sky. Apparently, undetected clouds are the main weak point of the LST satellite product, because they lead to strongly underestimated surface temperatures.

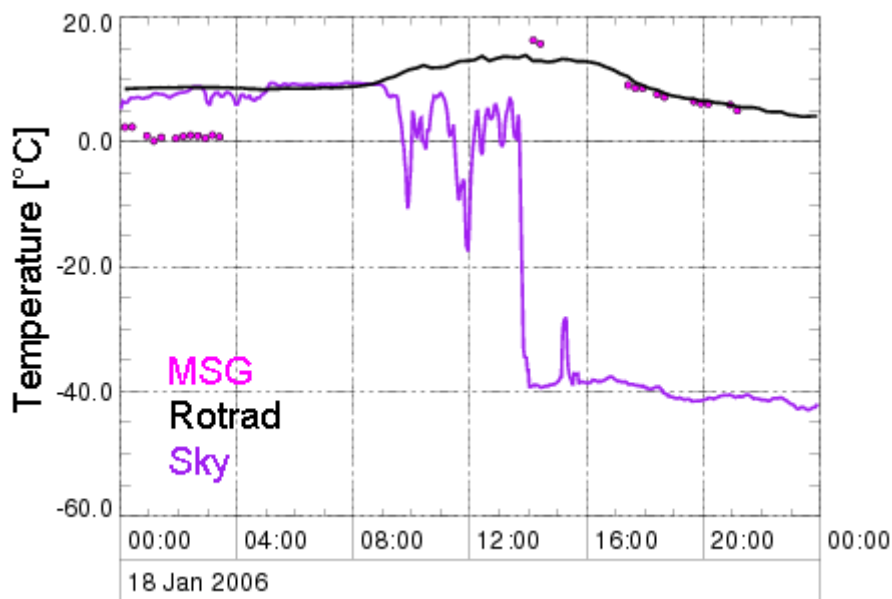


Figure 5.12: An example of LST-MSG (circles) contaminated by clouds at night. Surface brightness temperature measured at the ground station (Rotrad averaged with 40% ‘tree’, 30% ‘grass1’ and 30% ‘grass2’ – black line) is almost equal to the sky brightness temperature (purple line) which is characteristic for an overcast sky.

5.5 Evora ground temperature

The LST satellite product refers to a mean surface temperature within a pixel. For a comparison the surface temperature has to be estimated from the radiances from the Rotrad targets ‘tree’, ‘grass1’, ‘grass2’, and ‘sky’ (Figure 4.21).

The brightness temperatures of the ground targets are shown in Figure 5.13 for representative cloud-free days in each season of the year. At night the ground targets have similar temperatures whereas at daytime they can strongly differ. Differences in temperatures between tree and grass targets vary significantly according to the growth and dry seasons. In terms of surface temperatures, the grass regions are more similar to the tree canopy in the growth season than during summer when the grass regions resemble desiccated soil. Moreover, in the winter/spring seasons solar radiance is mostly absorbed by the leaves due to the low position of the sun.

The fraction of shadow over each grass spot changes daily as well as seasonally. In autumn, winter, and spring both grass spots are significantly shaded in the afternoon. During summer 'grass1' is exposed to direct sunlight over the whole day whereas 'grass2' becomes increasingly shaded in the afternoon. The selected days have been proven to be cloud-free, so that the variations in brightness surface temperature result from moving shadow of trees. Ground radiometers are making measurements in the same direction as the MSG satellite, so that all measurements experience similar fraction of shadow on their targets.

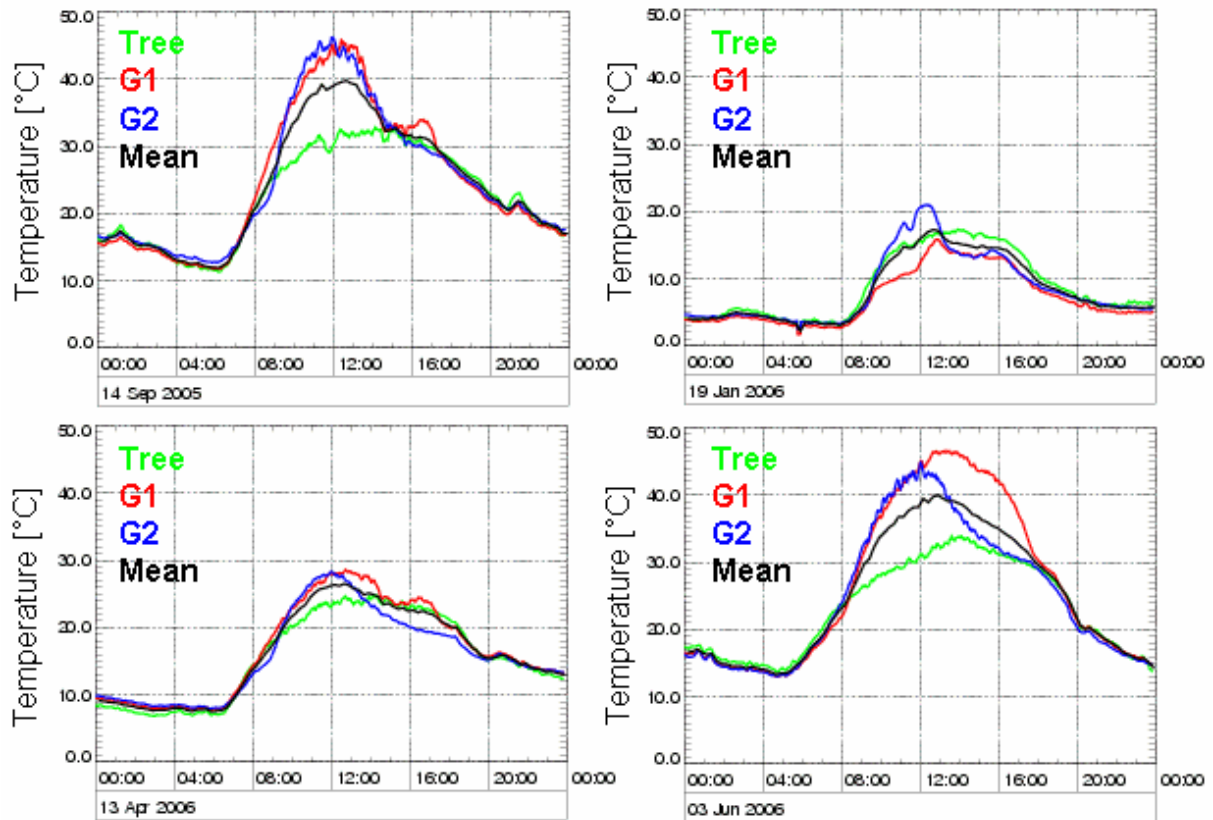


Figure 5.13: Brightness temperatures measured at the Evora site by Rotrad on a representative cloud-free day in each season of the year. Temperatures are smoothed with a moving time window of 10 min width. The black line shows the brightness temperatures of the weighted mean radiances from the ‘tree’ (green, 40%), ‘grass1’ (red, 30%) and ‘grass2’ (blue, 30%) regions. The fraction of shadow over grass regions changes over the year, which can be seen in surface brightness temperature data on selected days.

The brightness temperature of the Evora site should be estimated from the weighted mean radiance of the Rotrad measurement targets rather than as a weighted mean brightness temperature. However, as expected from equation Eq. 20, the differences between the two estimates are small as shown in Table 5.3. The weights of the Rotrad targets were chosen as described in chapter 4.5.

Tree temperature [°C]	Grass temperature [°C]	Weighted mean temperature [°C]	EBBT from weighted mean radiance [°C]	Difference [°C]
5.0	20.0	14.0	14.30	0.30
15.0	30.0	24.0	24.28	0.28
25.0	40.0	34.0	34.26	0.26

Table 5.3: Surface temperatures of the Evora site as weighted mean brightness temperature (Eq. 19) and as equivalent black body temperature (EBBT) of the weighted mean radiance (Eq. 18). Three representative temperature scenarios were used for the calculations with weights 40% and 60% for tree and grass regions, respectively.

Since temperatures at the ground station are retrieved from radiance observations they must be corrected for emissivity. Figure 5.14 shows surface temperatures of the Evora site obtained from Rotrad measurements (dashed line) using Eq. 17 with an effective emissivity value of 0.978 as provided by LSA-SAF (Table 5.2). The black solid line shows the surface brightness temperatures of the weighted mean radiances from the target regions. The difference between brightness and for emissivity corrected surface temperatures amount to about 1°C (lower panel). The sky brightness temperatures (purple line) are nearly constant at -40°C which is typical for a cloud-free day.

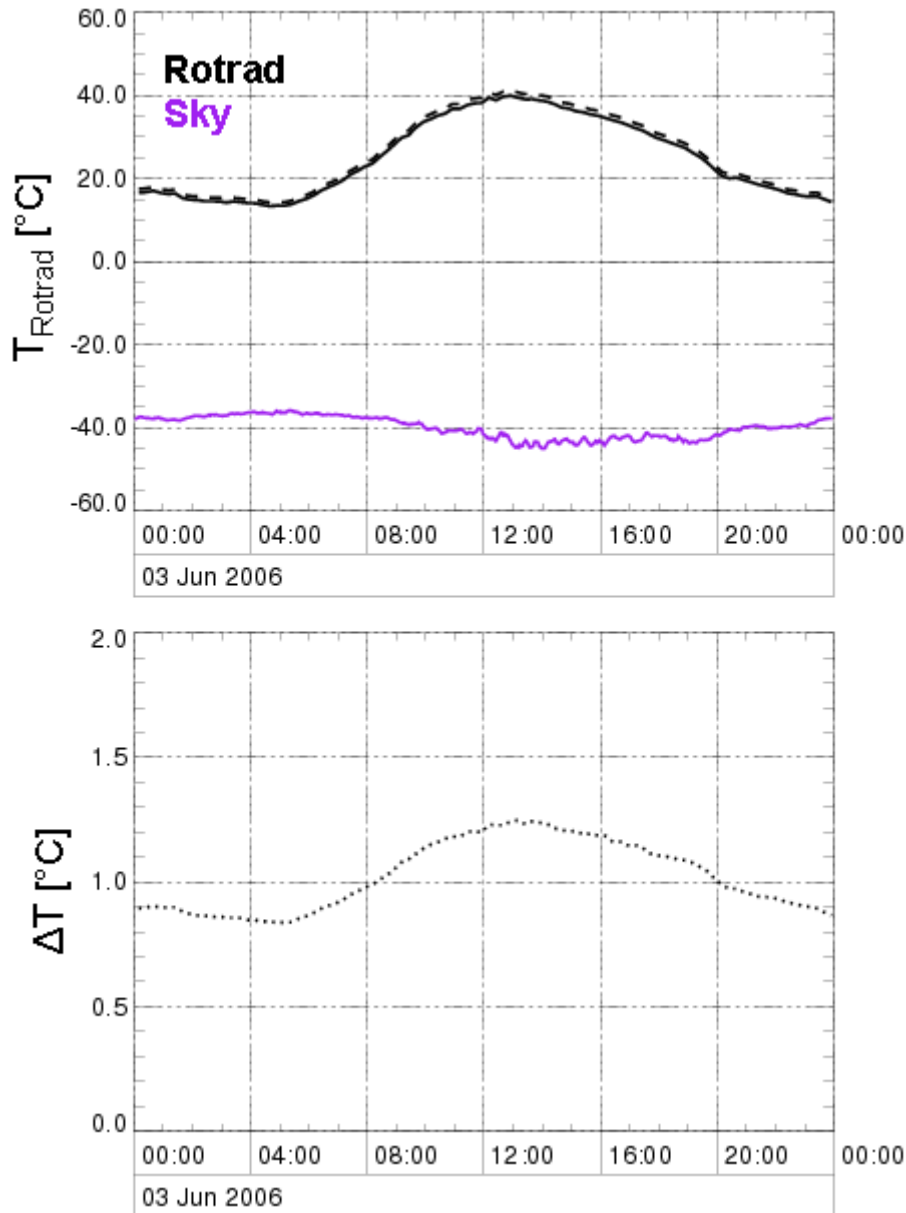


Figure 5.14: Top panel: Surface temperatures (black dashed line) and surface brightness temperatures of the Evora site. The brightness temperature of the sky (purple line) is typical for a cloud-free day. Lower panel: the differences in surface temperatures due to the emissivity correction (Eq. 17).

5.6 Resampling

Spatial and temporal resolution of ground data is much finer than that of the satellite data, so that the ground data must be resampled for the comparisons. The MSG satellite continuously scans its field of view at a rate of 15 minutes. The nominal time of each MSG slot refers to the beginning of the scan. The sensor reaches the Evora site 10 minutes after the beginning of a scan. Thus,

‘MSG slots’ of the Evora site are provided at 10, 25, 40, and 55 minutes after each hour.

The mean temperatures measured by the KT15 are stored every 10 min on a datalogger (chapter 4.6.7). The nominal time reported by the datalogger is constantly 5 minutes ahead the mean data acquisition time. If the timestamp of the satellite data does not match that of a KT15 value the mean of the two closest KT15 values are used.

Rotrad measurements acquired every 2 minutes are averaged within a time period of 10 minutes to reduce short-time temperature fluctuations. To match the time of the satellite data the nearest of the smoothed Rotrad measurements is used. Examples of smoothed Rotrad data are given in Figure 5.13. Standard deviations corresponding to the measurements of June 3, 2006 have been shown previously in Figure 5.7.

5.7 Error analysis

It has been shown in chapter 3.6 that the ground temperature of the Evora site can be estimated to good approximation from the weighted temperatures of its sub-regions. The ground temperature of the Evora site is then estimated as a weighted mean of the temperatures of the Rotrad targets.

$$T_{tot} = p_t T_t + (1 - p_t) (T_{g1} + T_{g2}) / 2 \quad Eq. 28$$

T_t , T_{g1} and T_{g2} are brightness temperatures of Rotrad targets for ‘tree’, ‘grass1’ and ‘grass2’, respectively. p_t is the area fraction of tree at the Evora site. The two grass targets are given equal weights. In case of one grass spot like it is the case for the KT15.85 measurements, we substitute a single temperature T_g for $(T_{g1} + T_{g2}) / 2$.

Considering only the error of tree cover estimation $\sigma(p_t)$ the standard deviation of the Evora surface brightness temperature T_{tot} is defined as follows:

$$\sigma(T_{tot}) = \sigma(p_t) |T_t - T_g| \quad Eq. 29$$

Eq. 29 shows that the error in ground temperature T_{tot} is proportional to the error in the tree area fraction and to the absolute temperature difference between tree and grass areas. This means that at night when trees and grass have almost the same temperature, the error in the estimate of tree area fraction does not affect the resulting averaged temperature.

Figure 5.15 shows the temperature error according to Eq. 29 for errors in tree area fraction of 0.05, 0.10, 0.15 and 0.20. For the Evora site this error is estimated to 0.10 (chapter 4.5.1.2). A histogram of the differences between grass and tree target of the measurements used in the validation is shown in Figure 5.16. In rare cases this difference can be as large as 20°C.

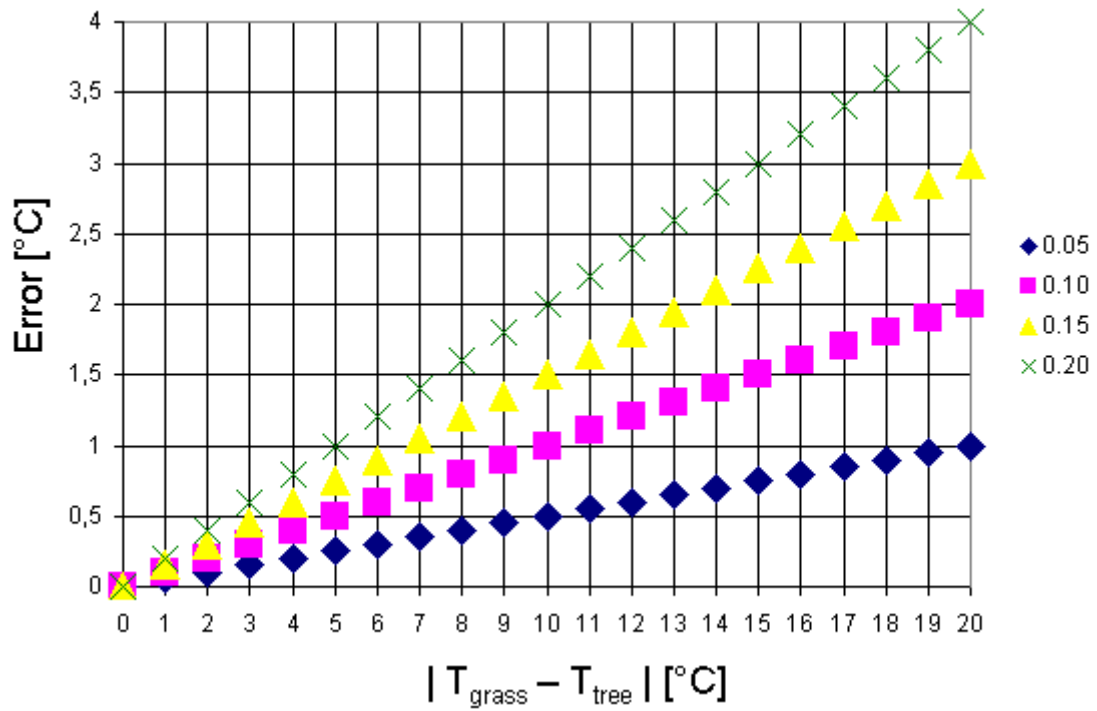


Figure 5.15: Standard error of the ground temperature T_{tot} as a function of absolute differences in tree and grass temperatures and uncertainties in tree area fraction of 0.05, 0.10, 0.15 and 0.20.

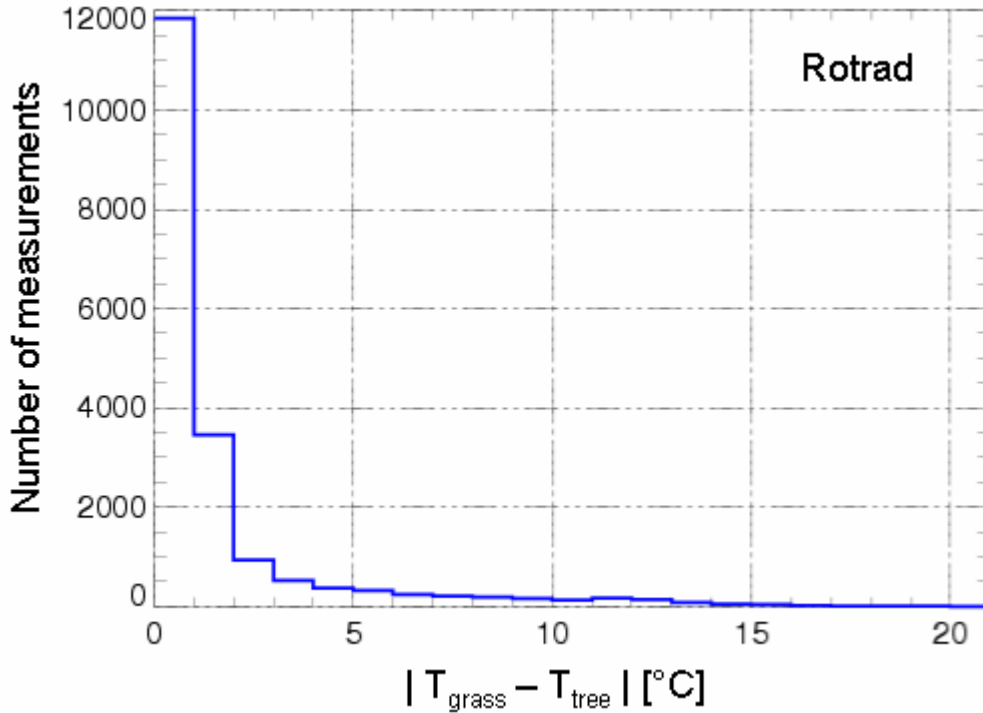


Figure 5.16: Histogram of differences between mean grass and tree temperatures of Rotrad measurement targets. In the validation period from August 2, 2005 to July 16, 2006 these temperature differences reach 20°C only in rare cases.

The analysis above considers only the influence of the error in tree fraction which is indeed a major source of uncertainty in the weighted ground brightness temperatures at daytime. At night the error in tree fraction is of minor importance and other sources of error limit the accuracy of the surface temperature used for the comparison with LST-MSG.

Starting from inverse Planck's function B^{-1} (Eq. 5) and making use of equations Eq. 17, Eq. 28 the variance of this temperature T_{sr} is given by equations Eq. 30 – Eq. 38 below as a function of estimated standard deviations for:

- emissivity $\sigma(\epsilon)$
- sky temperature $\sigma(T_{sky})$
- 'tree' target temperature $\sigma(T_t)$
- 'grass1' Rotrad target temperature $\sigma(T_{g1})$
- 'grass2' Rotrad target temperature $\sigma(T_{g2})$
- 'grass' KT15.85 target temperature $\sigma(T_g)$
- tree area fraction of the Evora site $\sigma(p_t)$

$$\sigma^2(T_{sr}) = \left(\frac{dB^{-1}}{dI_{sr}} \sigma(I_{sr}) \right)^2 \quad \text{Eq. 30}$$

$$\sigma^2(I_{sr}) = \left(\frac{\partial I_{sr}}{\partial I_{tot}} \sigma(I_{tot}) \right)^2 + \left(\frac{\partial I_{sr}}{\partial I_{sky}} \sigma(I_{sky}) \right)^2 + \left(\frac{\partial I_{sr}}{\partial \varepsilon} \sigma(\varepsilon) \right)^2 \quad \text{Eq. 31}$$

$$\sigma^2(I_{sky}) = \left(\frac{dB}{dT_{sky}} \sigma(T_{sky}) \right)^2 \quad \text{Eq. 32}$$

$$\sigma^2(I_{tot}) = \left(\frac{dB}{dT_{tot}} \sigma(T_{tot}) \right)^2 \quad \text{Eq. 33}$$

$$\sigma(T_{tot})^2 = A^T \cdot COV \cdot A \quad \text{Eq. 34}$$

$$A_{KT15} = \begin{bmatrix} p_t \\ 1 - p_t \\ T_t - T_g \end{bmatrix} \quad \text{Eq. 35}$$

$$COV_{KT15} = \begin{bmatrix} \sigma^2(T_t) & 0.95\sigma(T_t)\sigma(T_g) & 0 \\ 0.95\sigma(T_t)\sigma(T_g) & \sigma^2(T_g) & 0 \\ 0 & 0 & \sigma^2(p_t) \end{bmatrix} \quad \text{Eq. 36}$$

$$A_{Rotrad} = \begin{bmatrix} p_t \\ 0.5(1 - p_t) \\ 0.5(1 - p_t) \\ T_t - 0.5(T_{g1} + T_{g2}) \end{bmatrix} \quad \text{Eq. 37}$$

$$COV_{Rotrad} = \begin{bmatrix} \sigma^2(T_t) & 0.97\sigma(T_{g1})\sigma(T_t) & 0.96\sigma(T_{g2})\sigma(T_t) & 0 \\ 0.97\sigma(T_t)\sigma(T_{g1}) & \sigma^2(T_{g1}) & 0.98\sigma(T_{g2})\sigma(T_{g1}) & 0 \\ 0.96\sigma(T_t)\sigma(T_{g2}) & 0.98\sigma(T_{g1})\sigma(T_{g2}) & \sigma^2(T_{g2}) & 0 \\ 0 & 0 & 0 & \sigma^2(p_t) \end{bmatrix} \quad \text{Eq. 38}$$

Planck's equation and its inverse are used at the mean wavelength of the spectral response function of the radiometers (Eq. 7). In Eq. 31 it is assumed that sky

radiance I_{sky} , averaged surface leaving radiance I_{tot} , and emissivity ϵ are not correlated. Tree area fraction p_t is statistically independent from the ground temperature measurements. In contrast all ground temperatures are strongly correlated. Their natural correlation factors are computed from the available data. They are reported in the covariance matrices in Eq. 36 and Eq. 38 for the KT15.85 and Rotrad radiometers, respectively.

The variances of the radiometer measurements are calculated from sampling statistics of data collected within 10 minutes (chapter 5.2). It is known that emissivity hardly depends on temperature and was determined with estimated standard deviation of 0.2% (chapter 5.1). A problem arises because constant and too high values for the emissivity are used in the LST-MSG product. In order to avoid inconsistencies we use the satellite emissivity values for the correction of the ground radiometric measurements.

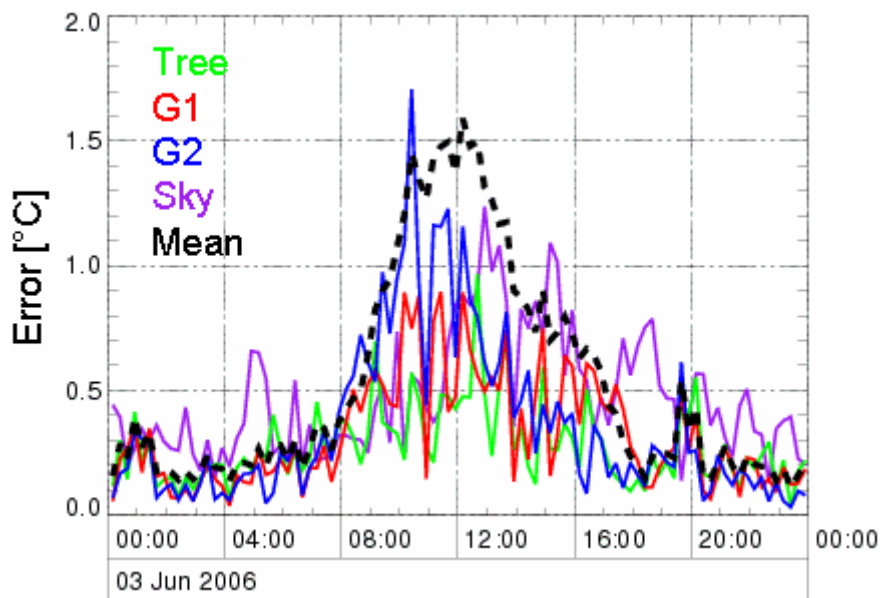


Figure 5.17: Diurnal variations of standard errors of surface temperatures according to Eq. 30 (black dashed line). Error contributions from the Rotrad radiometer are shown for the temperature measurements of the targets ‘tree’ (green), ‘grass1’ (red), ‘grass2’ (blue) and ‘sky’ (purple). Data resampled to 15 minutes time resolution.

Figure 5.17 shows the standard error calculated with equations Eq. 30 – Eq. 34 for an example day of June 3, 2006. The observed temperatures for that day are depicted in Figure 5.14. At daytime the main source of error derives from the error in area fraction occupied by tree crowns. As expected (Eq. 29) the standard error in surface temperature is much smaller at night and given by the instrument errors.

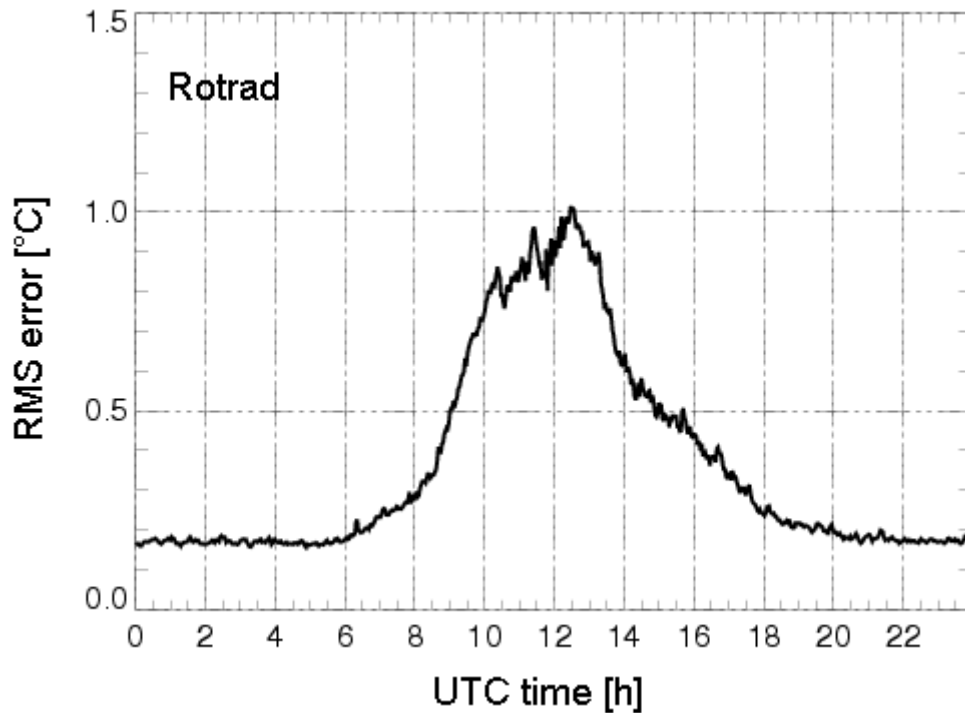


Figure 5.18: RMS error of Rotrad data. Inaccurate estimation of tree area fraction of the Evora site results in higher surface temperature uncertainties occurring from 6 a.m. to 6 p.m. Data were acquired in the time period from August 2005 to July 2006.

Figure 5.18 shows the root mean square error of the Evora surface temperatures obtained from this radiometer as a function of daytime; the corresponding distribution of data points is shown in Figure 5.19. Rotrad data were collected in the time period August 2005 to July 2006. Due to the selection criteria (chapters 5.3 and 5.4) an increased number of afternoon data was rejected.

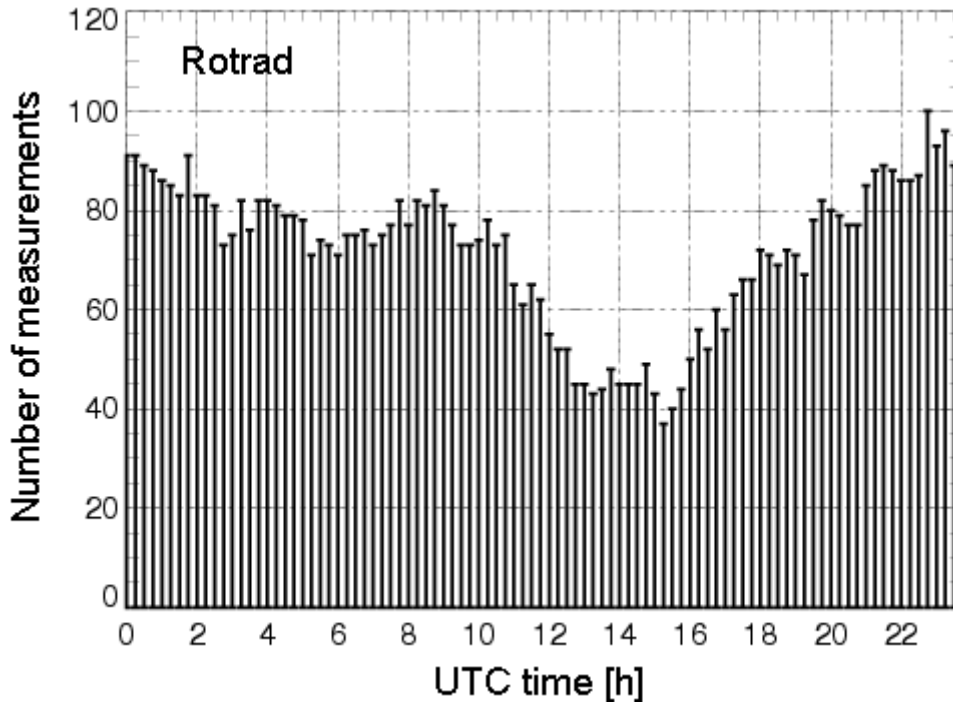


Figure 5.19: Diurnal distribution of Rotrad data used for the validation. Data were acquired in the time period from August 2005 to July 2006 and resampled to 15 minutes MSG time resolution.

Similar studies have been carried out for KT15.85 data that were collected between March and August 2007 (Figure 5.20 and Figure 5.21). At night the RMS error is comparable to the previous Rotrad measurements. During the day the standard deviations increase, but are smaller than those obtained from the Rotrad. This is consistent with the accuracy of the instruments (chapter 5.2). Moreover, the Rotrad targets are stronger influenced by moving shadows than the target positions of KT15.85.

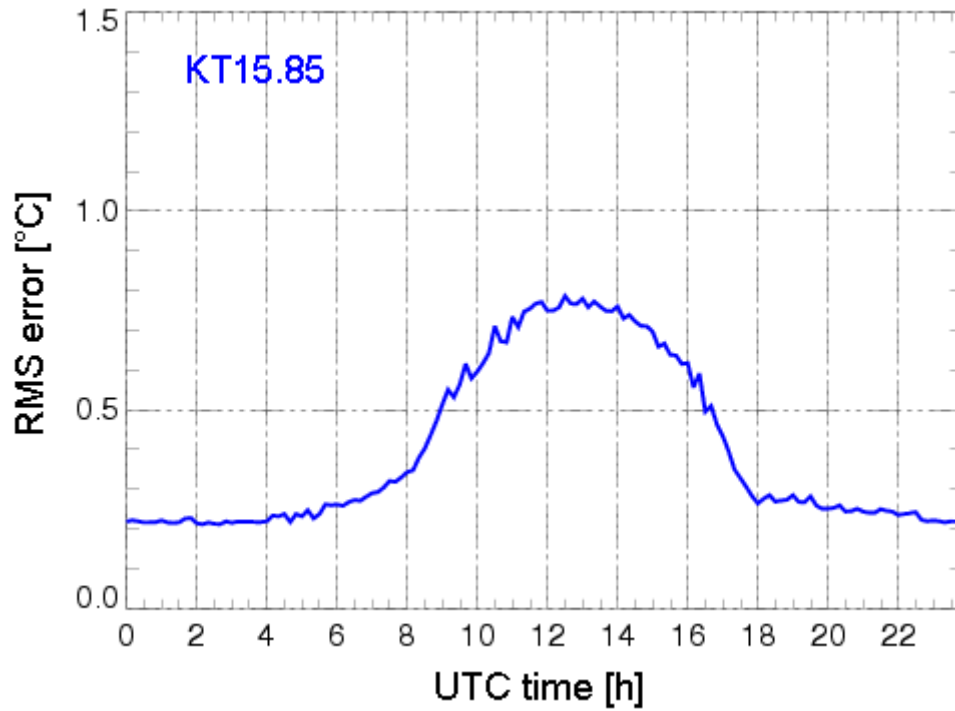


Figure 5.20: RMS error of KT15.85 data sampled in intervals of 10 minutes. Inaccurate estimation of tree area fraction results in higher surface temperature uncertainties occurring from 6 a.m. to 6 p.m. Data were acquired in the time period from March to August 2007.

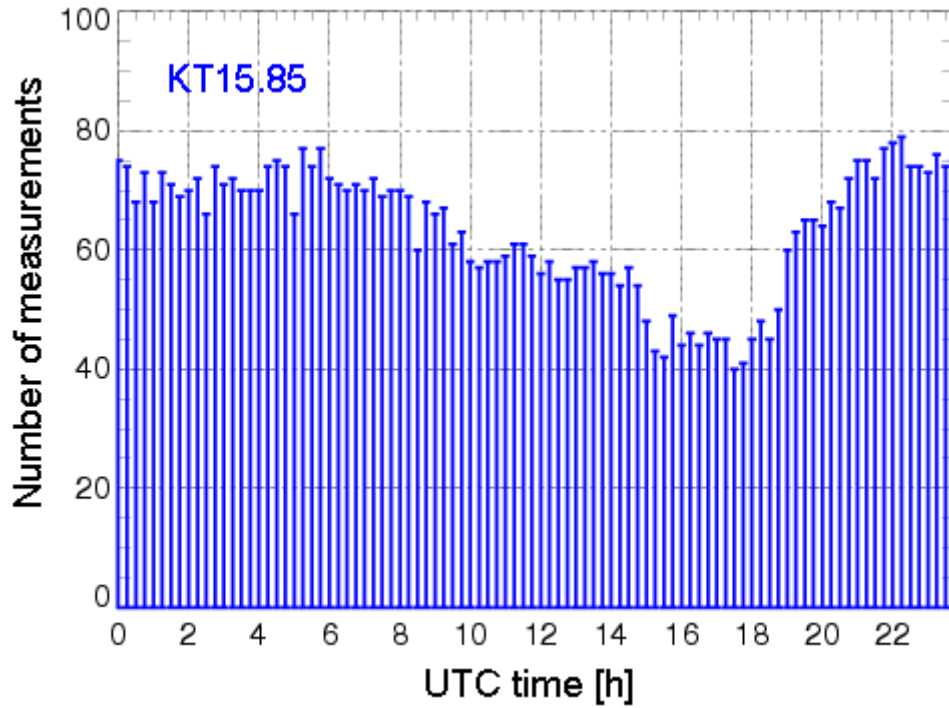


Figure 5.21: Diurnal distribution of KT15.85 used for the validation. Data were acquired in the time period from March to August 2007 and resampled to 15 minutes MSG time resolution.

6 Comparisons of ground and satellite LSTs

Preprocessed surface temperature measurements at the Evora site taken between August 2005 and August 2007 are compared in detail with corresponding satellite LST observations and show that their RMS differences do not exceed 2°C which is consistent with the nominal error of the LST-MSG product.

6.1 Comparisons with MSG data

The surface temperature measurements at the Evora site were carried out from August 2, 2005 to July 16, 2006 with Rotrad and continued with three KT15.85 radiometers from March 21 to August 26, 2007 replacing the broken Rotrad. For the validation the weighted average of Rotrad (40% tree, 30% ‘grass1’ and 30% ‘grass2’) and KT15.85 targets (40% tree and 60% grass) is used. Measurement targets and their weights characteristic for the Evora site are described in chapter 5.5. An additional wide-angle KT15.82 radiometer was used for independent control during both periods (chapter 4.8). Occasional lack of data during the two periods is due to technical problems at the ground station, missing LST satellite products because of system service, and presence of clouds over the validation site. The acceptance criteria for the measurements and satellite LSTs are listed in chapters 5.3 and 5.4, respectively. The histograms of the ground data used in the validation analysis are shown in Figure 5.19 and Figure 5.21 for Rotrad and KT15.85, respectively. The ground data were corrected for emissivity (chapter 5.1), resampled (chapter 5.6), and compared with ‘MSG slots’ (chapter 5.4).

Figure 6.1, Figure 6.2, and Figure 6.3 show scatter plots of ‘MSG slots’ and corresponding radiometric temperatures derived from Rotrad, KT15.85, and control KT15.82 measurements, respectively. Correlations between temperatures are generally high or even perfect (Rotrad: 0.985, KT15.85: 0.994, control KT15.82: 0.989) with regression lines of slope close to one. Only in case of control KT15.82 measurements the slope deviates significantly from unity because the tree fraction of the control target does not match that of the Evora site. The best agreement is found at night when the surface temperatures are low.

These results of the validation show that the RMS differences to the ground-truth temperatures do not exceed 2°C which is consistent with the nominal error of the LST-MSG product. A significant discrepancy occurs only in the comparison of LST-Rotrad and LST-MSG data taken during the development phase of the LST product in 2005. If these data are omitted the separated cluster of the data below the regression line completely disappears (not shown). Compared to Figure 6.1 the slope of the regression line increases to 0.93 and the RMS difference reduces to 1.7°C.

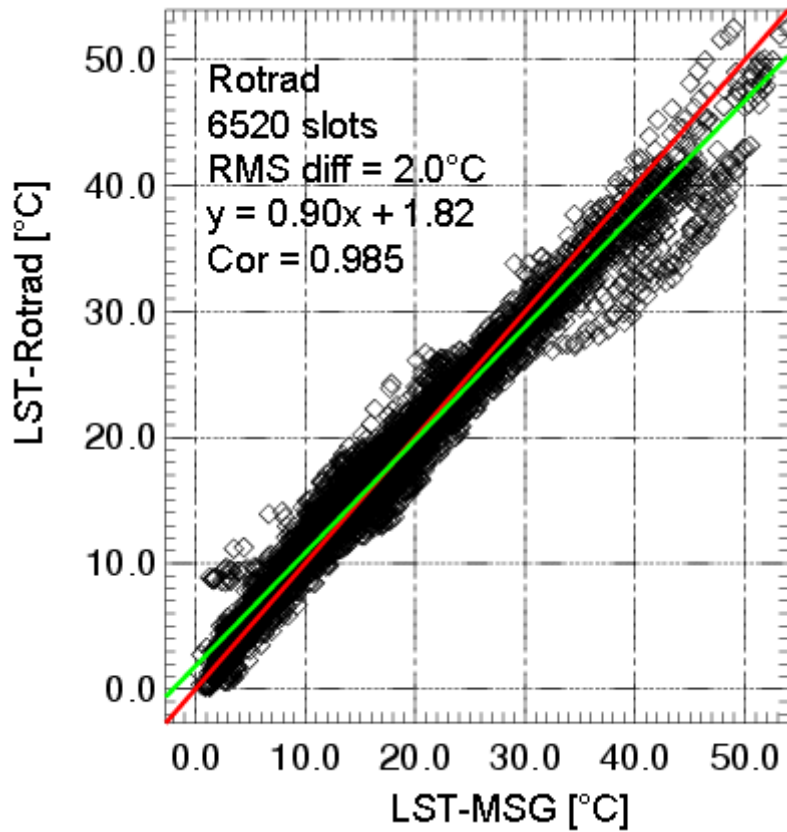


Figure 6.1: Evora surface temperatures obtained from Rotrad measurements plotted against ‘MSG slots’. The regression line (green) slightly deviates from the ideal solution $y = x$ (red). The cluster of the data below the regression line results from the data obtained in the development phase of the LST satellite product, i.e. in 2005. Analysed time period from August 2005 to July 2006.

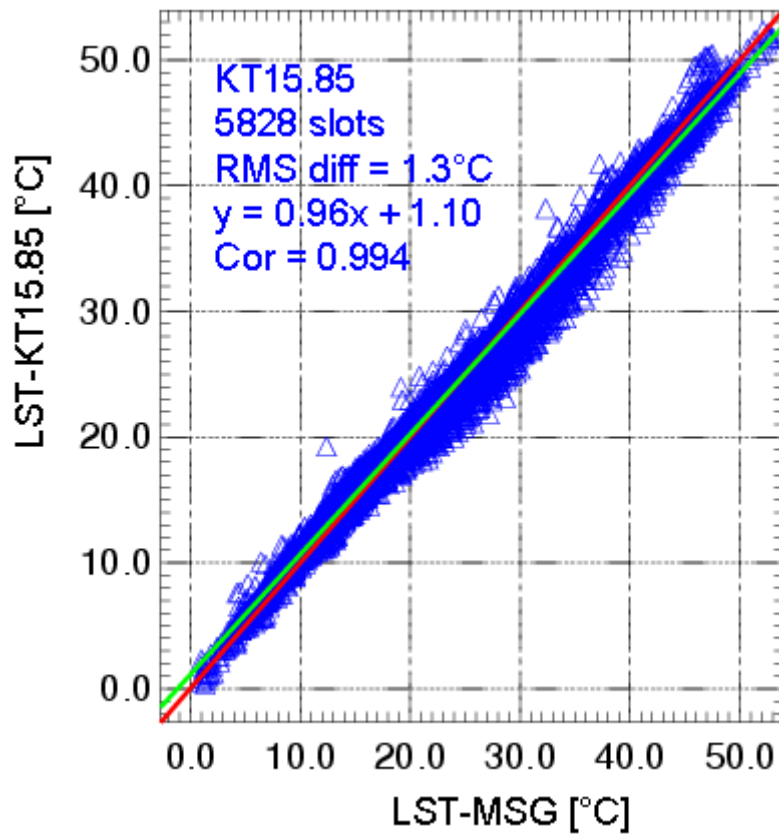


Figure 6.2: Evora surface temperatures obtained from KT15.85 measurements plotted against ‘MSG slots’. The regression line (green) slightly deviates from the ideal solution $y = x$ (red). Analysed time period from March to August 2007.

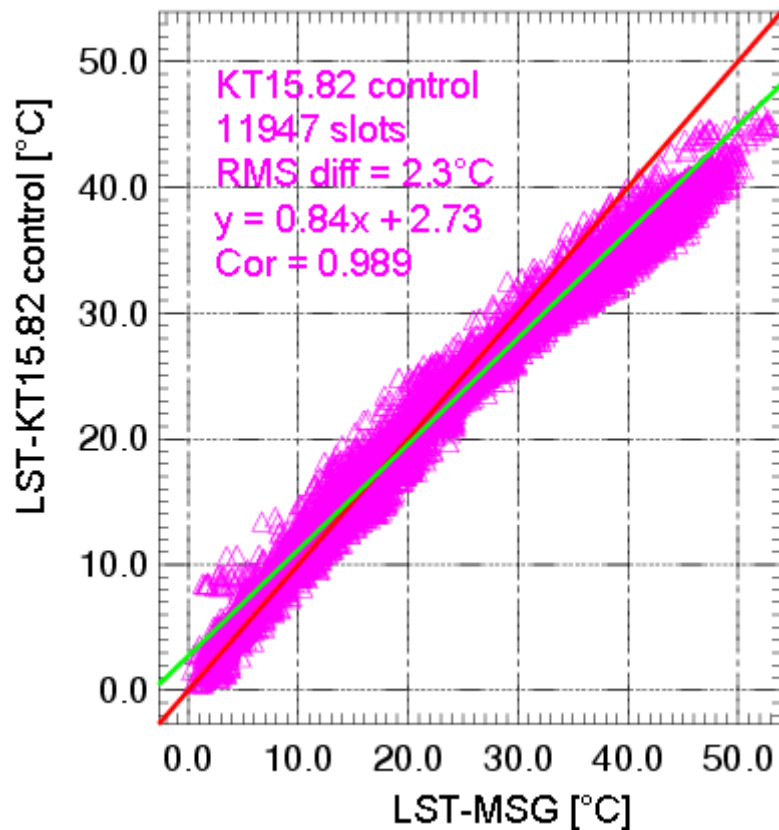


Figure 6.3: Evora surface temperatures obtained from control radiometer KT15.82 measurements plotted against ‘MSG slots’. The regression line (green) significantly deviates from the ideal solution $y = x$ (red). This deviation is due to the fact that the tree fraction of the target area seen by the wide-angle radiometer differs from the tree fraction of the Evora site. Analysed time period from August 2005 to August 2007.

Diurnal variations in mean temperature differences LST-MSG minus LST-ground instruments (Δ LST) are shown in Figure 6.4, Figure 6.6, and Figure 6.7. At night the LST-MSG is too low by 1°C compared to temperatures obtained from all three independent instruments at the ground station.

During the day the temperature bias varies in a complex, target-specific way. This is mostly due to shading effects of the various grass targets seen by the radiometers (Figure 4.23). These effects vary in a diurnal and season dependent way (Figure 5.13) which makes some of the ground measurements unsuitable for the validation of MSG observations. At daytime LST-MSG is generally higher than LST-Rotrad with a difference peak up to 4°C around 2 p.m. However, this peak decreases to $2.5 \pm 1.5^\circ\text{C}$ if the 2005 data obtained in the development phase of the LST-MSG product are not considered in the calculations (Figure 6.5).

A different picture is seen for LST-KT15.85 because of different shadow effects in its target area. These measurements were obtained in spring and summer when the impact of shadow on the grass targets is reduced. Temperature

difference peaks appear around sunrise and sunset (Figure 6.6). Between noon and 4 p.m. the bias becomes negative and is comparable to that observed during the night. As mentioned above the LST-KT15.82 control confirms the negative bias in LST-MSG at night. Since the tree fraction of the control target is larger than that of the Evora site a strong positive bias results.

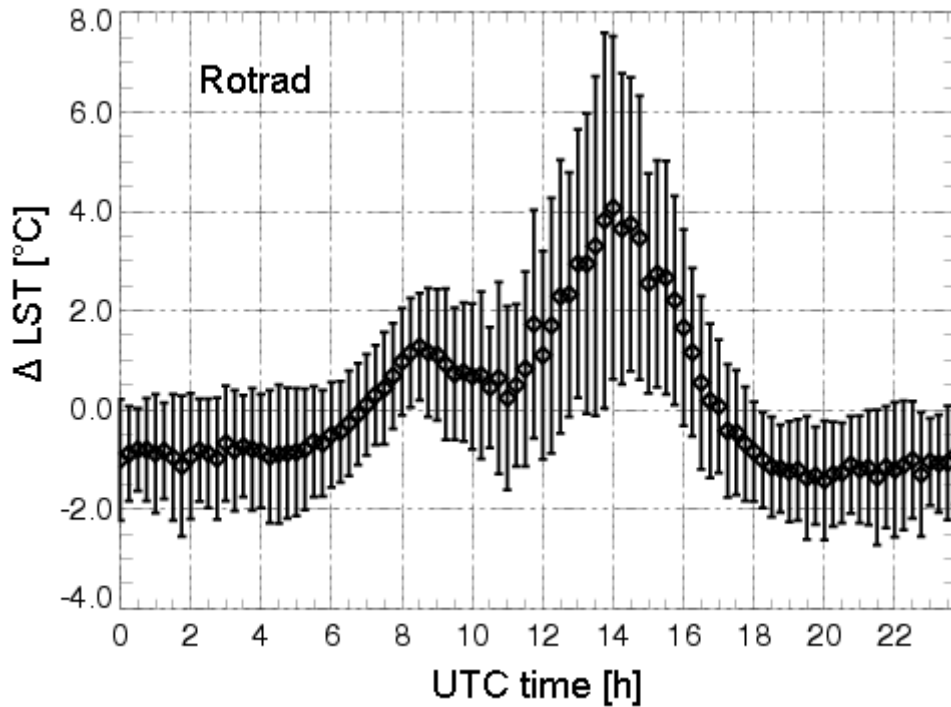


Figure 6.4: Diurnal variations in mean differences and their standard deviations (LST-MSG minus LST-Rotrad). Analysed time period from August 2005 to July 2006.

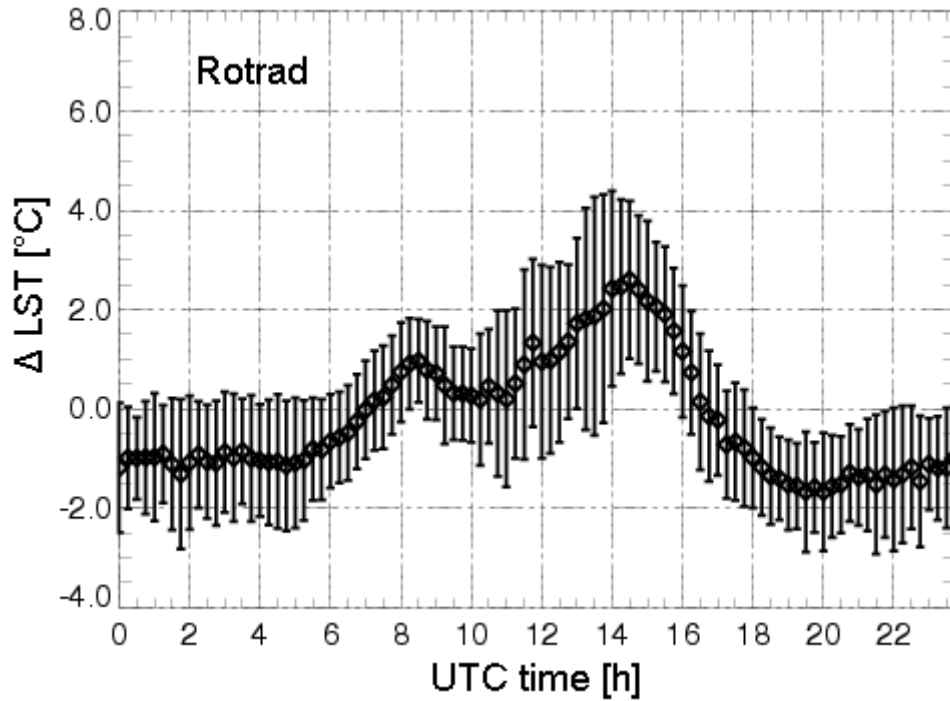


Figure 6.5: Diurnal variations in mean differences and their standard deviations (LST-MSG minus LST-Rotrad). Analysed time period from January to July 2006.

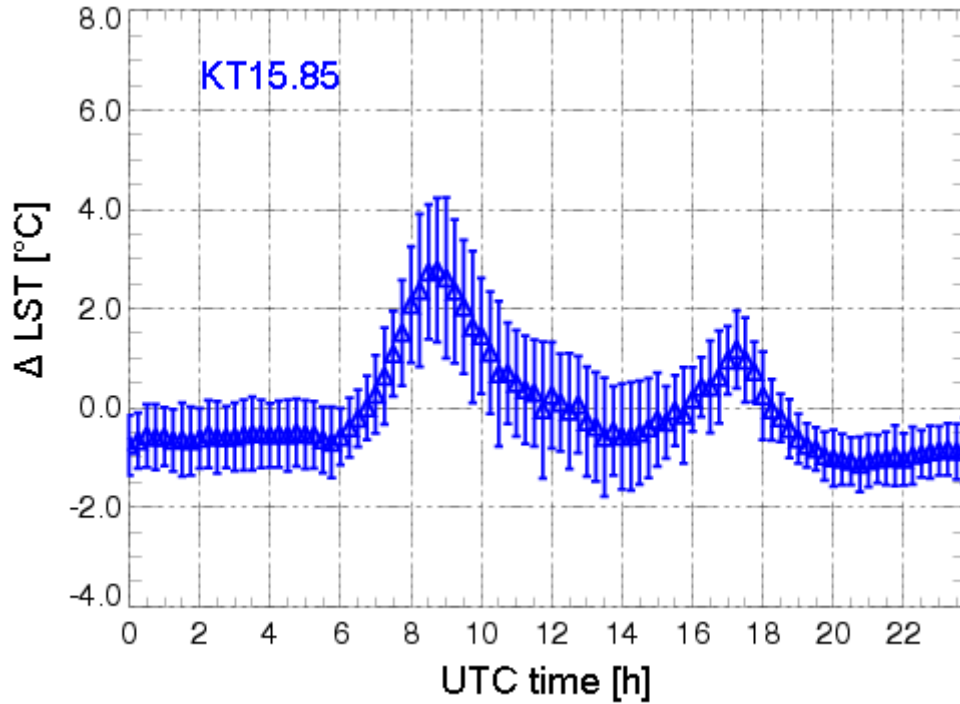


Figure 6.6: Diurnal variations in mean differences and their standard deviations ($LST-MSG$ minus $LST-KT15.85$). The peaks are caused by shadow effects at sunrise and sunset. Analysed time period from March to August 2007.

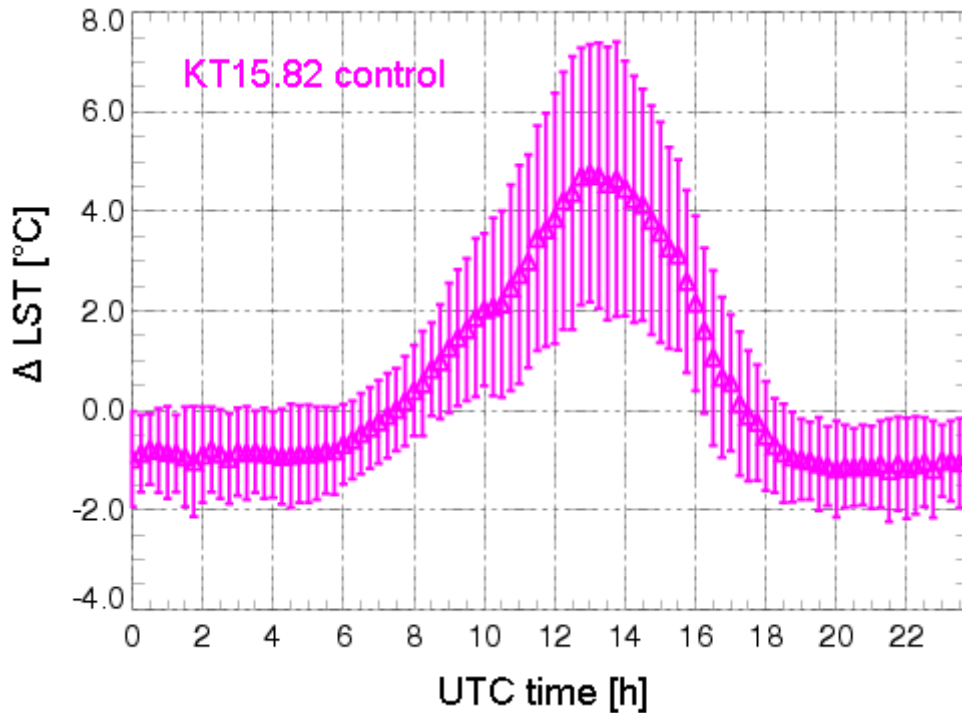


Figure 6.7: Diurnal variations in mean differences ($LST-MSG$ minus $LST-KT15.82$ control) and their standard deviations. Analysed time period from August 2005 to August 2007.

The mean Δ LST for each month are shown in Figure 6.8. The mean Δ LST vary by less than 2°C around zero which is within the nominal accuracy of the LST-MSG product. Possible reasons for the greater variability of the bias during September and October 2005 are incorrect coefficients used in the split-window calculations at high ground temperatures during the development phase of the LST product (see Figure 6.10). In addition, greater deviations result in part from shadows over both grass targets in the afternoon (see Figure 5.13).

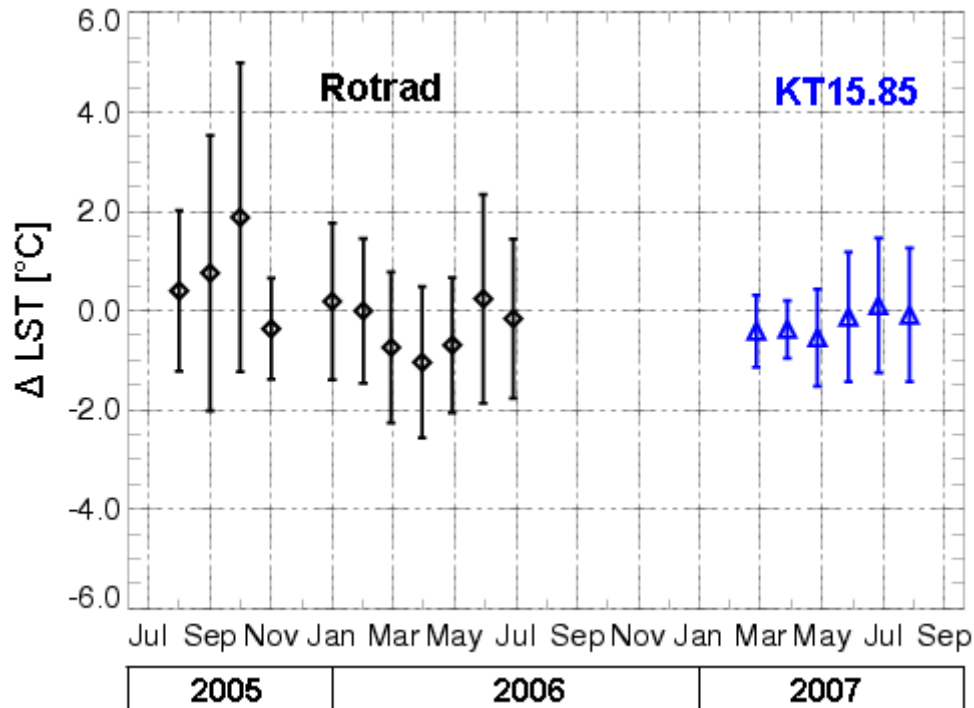


Figure 6.8: Monthly variations in mean differences (LST-MSG minus LST-ground station) and their standard deviations.

The mean standard deviation of the difference LST-MSG minus LST-ground station, $\sigma(\Delta$ LST), is specified for each month in Figure 6.9. Note, that $\sigma(\Delta$ LST) is larger than the error bar given in the previous figure because the bias in Δ LST is not removed. Still, most of the $\sigma(\Delta$ LST) are within the specified error in the LST-MSG product (2°C).

Generally, Rotrad data indicate larger disagreements to satellite LST than KT15.85. These greater deviations result from shadows over grass targets (see Figure 5.13 and Figure 4.23) and from the fact that the LST-MSG product was still in a development stage till summer 2006. Despite these circumstances, the discrepancies between LST-MSG and ground station LST do not exceed the nominal accuracy of the satellite product (2°C). A significant improvement of LST-MSG product was noted by comparisons with the LST-KT15.85 data taken in 2007. The RMS difference temperature $\sigma(\Delta$ LST) is less than 1.5°C (Figure 6.9).

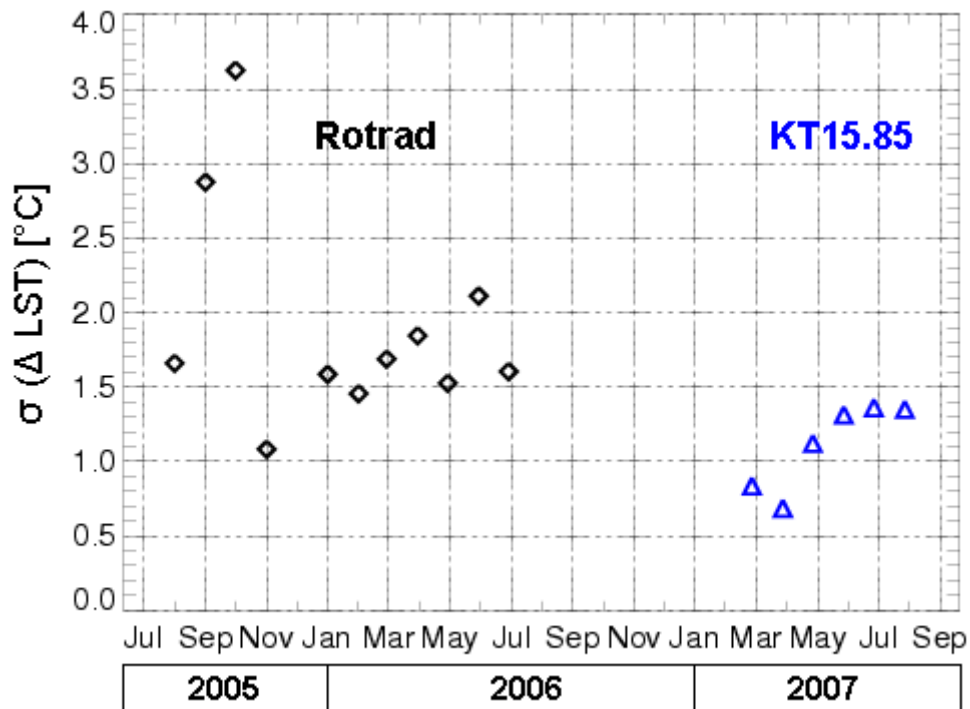


Figure 6.9: Monthly variations in root mean square differences (LST-MSG minus LST-ground station).

6.2 Comparisons with Meteosat-7 data

Meteosat-7, the predecessor of the MSG satellites (chapter 2) was in service until June 14, 2006 providing data from the geostationary orbit parallel to MSG, but with different spectral and spatial resolution. Overlapping LST data slots of Meteosat-7 and MSG between June and October 2005 are compared.

Meteosat-7 has only one IR band (10.5 – 12.5 μm) from which LSTs can be derived. Temperature data were obtained using a neural network approach ([Göttsche and Olesen, 2002a](#)) and resampled to match the MSG pixels (data provided by [Schmidt, 2007](#)). Satellite slots obscured by clouds are partly recovered using the Thermal Surface Parameter (TSP) model ([Göttsche and Olesen, 2001](#)). The TSP model uses clear-sky satellite slots available for each day to predict the missing surface temperatures from the function describing the diurnal surface temperature cycle.

Figure 6.10 shows the diurnal LST cycle at Evora derived from Meteosat-7 (green), MSG (pink) and the ground measurements (black) for September 28, 2005. Night LSTs are in perfect agreement. However, during daytime the LST derived from Meteosat-7 matches the LST-Rotrad data (apart from a shadow effect between 1 p.m. to 4 p.m.), but disagrees with the LST-MSG data. At noon LST-MSG is up to 7°C higher than LST-Meteosat-7. This could indicate a problem with the LST-MSG product rather than result from shadow effects at the ground station.

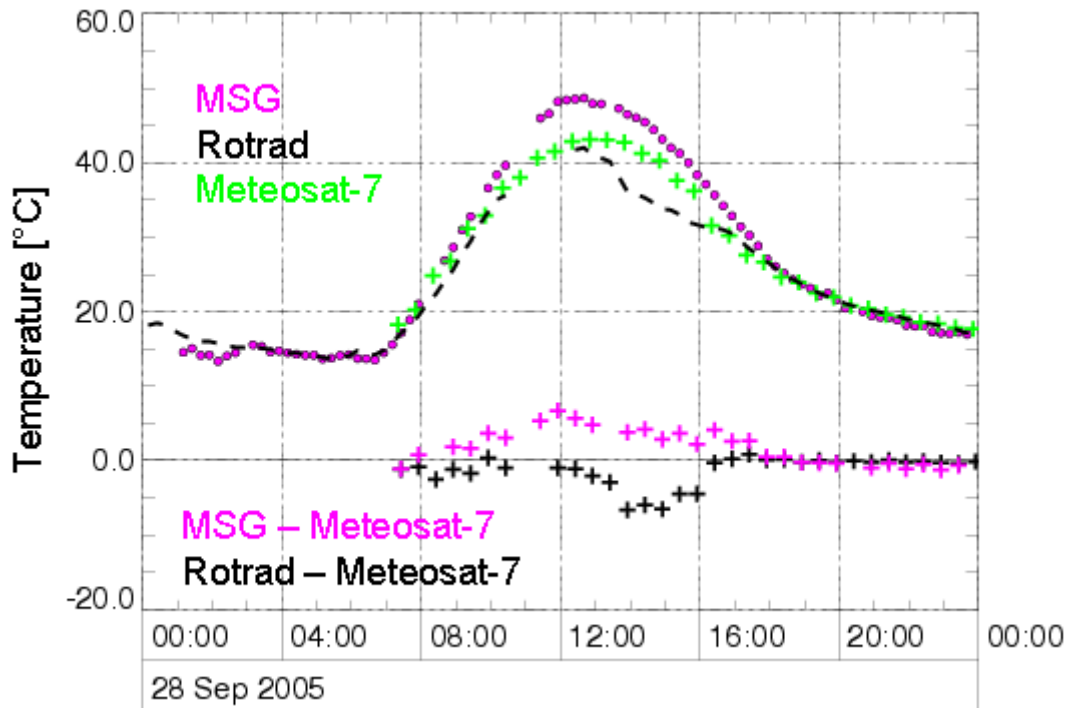


Figure 6.10: LST derived from MSG (pink cycles), Meteosat-7 (green crosses) and Rotrad measurements (black dashed line). Lower: differences MSG (pink crosses) and Rotrad (black crosses) minus LST from Meteosat-7.

A scatter plot between Meteosat-7 and MSG LST data in the time period from June to October 2005 is depicted in Figure 6.11. The correlation is very high and equals 0.973. However, the slope of the regression line deviates significantly from one. It appears that for high surface temperatures LST-MSG is up to 7°C higher than Meteosat-7, whereas for low surface temperatures (at night) the agreement is excellent. The overestimated LST-MSG values within the comparison time period are due to incorrect coefficients used in the split-window calculations at high ground temperatures during the development phase of the LST product ([Schmidt, 2007](#)).

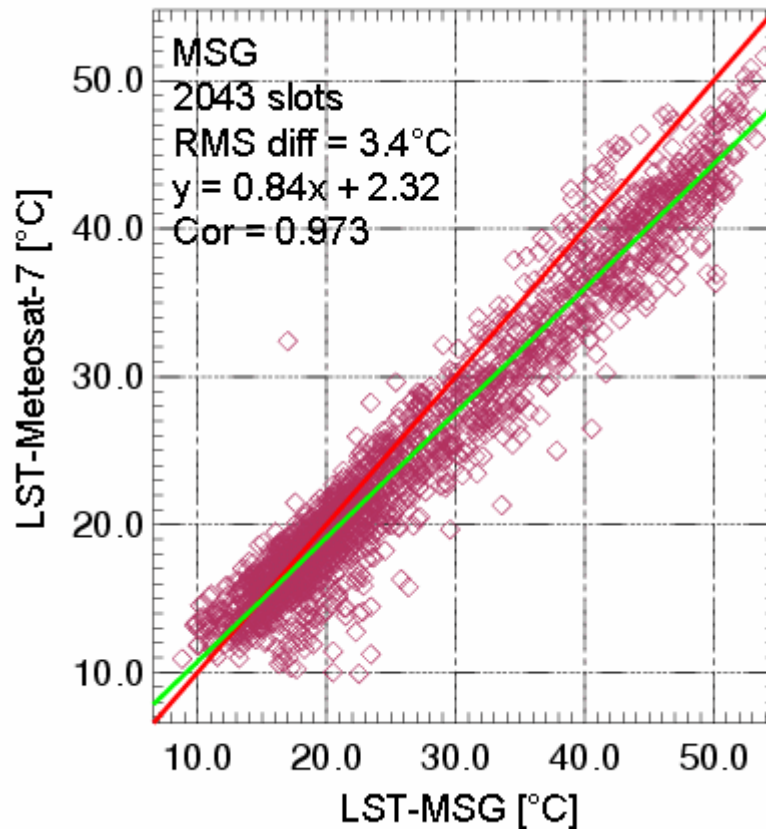


Figure 6.11: ‘Meteosat-7 slots’ plotted against ‘MSG slots’. The regression line (green) deviates from ideal solution $y = x$ (red) presumably because the LST-MSG is overestimated at high temperatures. Calculations made for the time period from June to October 2005.

Figure 6.12 shows the scatter plot of Meteosat-7 and Rotrad derived LSTs. Due to technical problems with Rotrad only 30 days within the time period from August to October 2005 are overlapping with available Meteosat-7 data. The available data correlate with 0.935 with a slope of the regression line close to unity. This means that there are little systematic deviations between ground station and Meteosat-7 LSTs. The scatter of the data could be caused by clouds and the implementation of the TSP model applied to sparse Meteosat-7 data. This model describes the diurnal LST cycle by a sinus function during daytime and a logarithmic attenuation function for night-time. Hence, short-time fluctuations of LST caused by different wind speeds, advection, or evaporation are not reflected by the TSP model (Schmidt, 2007). The large scatter of data above the regression line is caused by shadows at the station in the afternoons (Figure 6.10).

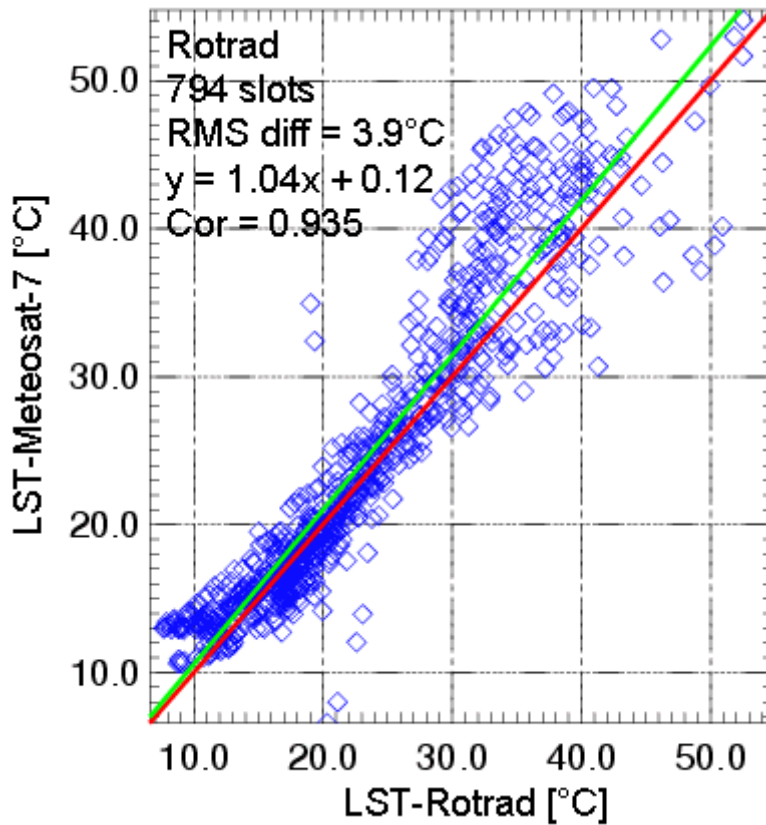


Figure 6.12: ‘Meteosat-7 slots’ plotted against LST-Rotrad (weighted with 40% ‘tree’, 30% ‘grass1’ and 30% ‘grass2’). The regression line (green) slightly deviates from ideal solution $y = x$ (red). Calculations made for the time period from August to October 2005.

7 Conclusions and outlook

Land surface temperature (LST) is an important product of the MSG satellite provided on an operational basis by the LSA-SAF project. This product is derived by the generalised split-window method which involves satellite radiance sensing in two adjacent infrared bands and a complex procedure combining a database of pre-calculated coefficients with actual site and weather information. Thus, permanent validation of the LSTs provided by the MSG satellite is of crucial importance and requires ground-based measurements.

Available ground-truth sites within the MSG field of view, although homogeneous, were too small to be representative for an MSG pixel. Therefore, an effort has been made to set up a new permanent station aimed at validation of LSTs derived from MSG data on a regular basis. Subject of this thesis was to verify the suitability of the selected validation site near Evora, Portugal (38.54° N, 8.00° W), installations and tests of the instruments, and to carry out comparisons of the ground-based radiometric measurements with satellite derived LSTs.

The selected validation site has many cloud-free days. It is located in evergreen oak woodland, hardly disrupted by fields and villages. The Evora site satisfies the homogeneity requirements over an area of $12 \times 12 \text{ km}^2$ as verified by high resolution satellite images and site visits. The site basically consists of tree crowns and grass in between which admits a simple model of only two temperatures distributed over the land cover elements. Thus, a key parameter describing the site is the fraction of its area covered by tree crowns. This fraction was estimated as 0.4 ± 0.1 from a high resolution Landsat satellite image using Normalised Difference Vegetation Index (NDVI). An alternative analysis was carried out with an Ikonos satellite image confirming the homogeneity of the site. However, the fraction of tree canopy cover of 0.47 estimated by the segmentation method was not accepted because this method is too sensitive to systematic errors in tracing tree boundaries.

For determination of ground-truth LST from the two land cover elements of the Evora site infrared radiometers were mounted on the tower well above the tree canopy and directed towards the tree and grass targets at the same viewing angle as the MSG satellite. Additional radiometric measurements were performed for monitoring sky brightness temperatures which are needed for emissivity correction. These measurements were also found to be extremely useful for detection of clouds that were not detected in the LST satellite product. To avoid inclusion of cloud contaminated data in the validation, acceptance criteria were developed and applied in an automatic fashion.

Detailed error analysis has shown that the accuracy of the land surface temperature retrieved at the ground station is proportional to the temperature difference of the land cover elements and the standard error of the tree area fraction. The expected errors were confirmed by the observed diurnal variations in the temperature measurements: at night this error was typically around 0.2°C because tree and grass targets have a very small temperature difference while it displayed a peak of up to 1°C around noon.

This study uses LST data from MSG satellite between August 2005 and August 2007. Agreement of these data with corresponding ground LSTs is remarkably good (correlation above 0.98) despite the simple characterisation of the Evora site by just two land cover elements. Moreover, the only parameter of the model, namely the tree area fraction, was not fitted but fixed according to independent determinations. The results have confirmed the nominal accuracy of 2°C of the LST-MSG product derived by LSA-SAF. The smallest deviations occur at night and are typically around -1°C which is better than the specified accuracy of the LST product. The larger deviations observed at daytime arise from deficits of the validation set-up at the ground station. Due to constraints imposed by the location of the tower the selection of measurement targets is not optimal. These measurement targets are partly shaded in a diurnal and seasonal dependent way.

The ground-truth data from the Evora site were used for the validation of LSTs derived from another satellite as well. Comparisons with Meteosat-7 LST during June to October 2005 show good agreement (correlation of 0.93). Unfortunately, the Meteosat-7 satellite was terminated shortly after the Evora station was fully functional.

The results from the Evora validation site suggest a number of improvements, some of which have been implemented recently. To avoid shadow effects the measurement targets should be chosen at locations that are permanently exposed to the sun. Accordingly, the radiometers from the Evora tower were moved to a nearby location and directed towards targets satisfying these criteria. Another improvement would be the sampling of permanently shaded grass target at the ground station. Then, an anisotropic LST model proposed by [Pinheiro et al., 2004](#) and [Pinheiro et al., 2006](#) could be implemented. This model is expected to estimate shaded area fraction as a function of the sun and satellite position.

Summarising, the success of the Evora ground station and the experience gained at this site encourage the set-up of further permanent validation stations in other geographical locations. An effort has been made to set up new validation stations in Senegal and Namibia. Ground LST-data from all three sites will be used for validation of the LST product from the recently launched European polar satellite Metop. The available logistics of the ground stations is expected to be a valuable asset for other, new satellite products as well.

8 References

- Aminou, D. M. A., Luhmann, H. J., Hanson, C., Pili, P., Jacquet, B., Bianchi, S., Coste, P., Pasternak, F., and Faure, F., 2003, Meteosat Second Generation – a comparison of on-ground and on-flight Imaging and Radiometric performances of SEVIRI on MSG-1. Proceedings of the EUMETSAT Meteorological Satellite Conference Weimar (Germany), 19 September – 3 October 2003
- Becker, F., 1987, The impact of spectral emissivity on the measurements of land surface temperature from a satellite. *International Journal of Remote Sensing*, vol. 8, no. 10, pp. 1509 – 1522
- Becker, F. and Li, Z.-L., 1990, Towards a local split window method over land surfaces. *International Journal of Remote Sensing*, vol. 11, no. 3, pp. 369 – 393
- Becker, F. and Li, Z.-L., 1995, Surface temperature and emissivity at various scales: definition, measurement and related problems. *Remote Sensing Reviews*, vol. 12, no. 3 – 4, pp. 225 – 253
- Berk, A., Anderson, G. P., Acharya, P. K., Chetwynd, J. H., Bernstein, L. S., Shettle, E. P., Matthew, M. W. and Adler-Golden, S. M., 2000, MODTRAN4 Version 2 User's Manual, Air Force Research Laboratory, Space Vehicle Directorate, Air Force Materiel Command, Hanscom AFB, MA 01731-3010
- Bhattacharya, B. K. and Dadhwal, V. K., 2003, Retrieval and validation of land surface temperature (LST) from NOAA AVHRR thermal images of Gujarat, India. *International Journal of Remote Sensing*, vol. 24, no. 6, pp. 1197 – 1206
- Brasseur, G. and Solomon, S., 1986, *Aeronomy of the Middle Atmosphere. Chemistry and Physics of the Stratosphere and Mesosphere*. Dordrecht (Holland), D. Reidel Publishing Company
- Carreiras, J. M. B., Pereira, J. M. C. and Pereira, J. S., 2006, Estimation of tree canopy cover in evergreen oak woodlands using remote sensing. *Forest Ecology and Management*, vol. 223, pp. 45 – 53
- Caselles, V. and Sobrino, J.A., 1989, Determination of frosts in orange groves from NOAA-9 AVHRR data. *Remote Sensing of Environment*, vol. 29, no. 2, pp. 135 – 146

- Chander, G. and Markham, B., 2003, Revised Landsat-5 TM Radiometric Calibration Procedures and Postcalibration Dynamic Ranges. *IEEE Transactions on Geoscience and Remote Sensing*, vol. 41, no. 11, pp. 2674 – 2677
- Chevallier, F., Morcrette, J.-J., Chédin, A., and Cheruy, F., 2000, TIGR-like atmospheric-profile databases for accurate radiative-flux computation. *Quarterly Journal of the Royal Meteorological Society*, vol. 126, issue 563, pp. 777 – 785
- Coll, C., Caselles, V., Galve, J. M., Valor, E., Niclòs, R., Sánchez, J. M. and Rivas, R., 2005, Ground measurements for the validation of land surface temperatures derived from AATSR and MODIS data. *Remote Sensing of Environment*, vol. 97, issue 3, pp. 288 – 300
- Coll, C., Caselles, V., Galve, J. M., Valor, E., Niclòs, R. and Sánchez, J. M., 2006, Evaluation of split-window and dual-angle correction method for land surface temperature retrieval from Envisat/Advanced Along Track Scanning Radiometer (AATSR) data. *Journal of Geophysical Research*, vol. 111, no. D12105, doi: 10.1029/2005JD006830
- Dash, P., Göttsche, F. M., Olesen, F. S. and Fischer, H., 2002, Land surface temperature and emissivity estimation from passive sensor data: theory and practice – current trends. *International Journal of Remote Sensing*, vol. 23, no. 13, pp. 2563 – 2594
- Dash, P., Olesen, F. S. and Prata A. J., 2004, Optimal land surface temperature validation site in Europe for MSG. *Proceedings of the EUMETSAT Meteorological Satellite Conference, Prague (Czech Republic), 31 May – 4 June 2004*, pp. 248 – 264
- Donlon, C. J., Keogh, S. J., Baldwin, D. J., Robinson, I. S., Ridley, I., Sheasby, T., Barton, I. J., Bradley, E. F., Nightingale, T. J. and Emery, W., 1998, Solid-State Radiometer Measurements of Sea Surface Skin Temperature. *Journal of Atmospheric and Oceanic Technology*, vol. 15, issue 3, pp. 775 – 787
- Göttsche, F. M., and Olesen, F. S., 2001, Modelling of diurnal cycles of brightness temperature extracted from METEOSAT data. *Remote Sensing of Environment*, vol. 76, no. 3, pp. 337 – 348

- Göttsche, F. M. and Olesen, F. S., 2002a, Evolution of neural networks for radiative transfer calculations in the terrestrial infrared. *Remote Sensing of Environment*, vol. 80, pp. 157-164
- Göttsche, F. M. and Olesen, F. S., 2002b, Atmospheric correction of IR satellite data using neural networks. Recent advances in quantitative remote sensing, Torrent, Spain, 16 – 20 September 2002
- Hook, S. J., Prata, A. J., Alley, R. E., Abtahi, A., Richards, R. C., Schladow, S. G. and Pálmarsson, S. Ó., 2003, Retrieval of Lake Bulk and Skin Temperatures Using Along-Track Scanning Radiometer (ATSR-2) Data: A Case Study Using Lake Tahoe, California. *Journal of Atmospheric and Oceanic Technology*, vol. 20, pp. 534 – 548
- Hook, S. J., Chander, G., Barsi, J. A., Alley, R. E., Abtahi, A., Palluconi, F. D., Markham, B. L., Richards, R. C., Schladow, G. S. and Helder, D. L., 2004, In-Flight Validation and Recovery of Water Surface Temperature With Landsat-5 Thermal Infrared Data Using an Automated High-Altitude Lake Validation Site at Lake Tahoe. *IEEE Transactions on Geoscience and Remote Sensing*, vol. 42, no. 12, pp. 2767 – 2776
- Kondratyev, K. Y., 1969, *Radiation in the Atmosphere*. New York Academic Press, pp. 16 – 22
- Kustas, W. P. and Norman, J. M., 1996, Use of remote sensing for evapotranspiration monitoring over land surfaces. *Hydrological Sciences – Journal – des Sciences Hydrologiques*, vol. 41, no. 4, pp. 495 – 516
- Madeira, C., 2002, Generalised split-window algorithm for retrieving land-surface temperature from MSG/SEVIRI data. *Proceedings of the Land Surface Analysis SAF Training Workshop*, Lisbon, 8 – 10 July 2002, pp. 42 – 47
- McMillin, L. M., 1975, Estimation of Sea Surface Temperatures from two infrared window measurements with different absorption. *Journal of Geophysical Research*, vol. 80, no. 36, pp. 5113 – 5117
- Meteosat Second Generation, MSG System Overview, 2001, EUM TD 07, issue 1.1,
http://www.eumetsat.int/Home/Main/Publications/Technical_and_Scientific_Documentation/Technical_Descriptions/index.htm?l=en

- Norman, J. M. and Becker, F., 1995, Terminology in thermal infrared remote sensing of natural surfaces. *Agricultural and Forest Meteorology*, vol. 77, pp. 153 – 166
- Ottlé, C. and Vidal-Madjar, D., 1992, Estimation of Land Surface Temperature with NOAA9 Data. *Remote Sensing of Environment*, vol. 40, pp. 27 – 41
- PC208W Version 3.3 Datalogger Support Software, User Guide, 2001, Campbell Scientific, Inc.
- Peres, L. F. and DaCamara, C., 2005, Emissivity Maps to Retrieve Land-Surface Temperature From MSG/SEVIRI. *IEEE Transactions on Geoscience and Remote Sensing*, vol. 43, no. 8, pp. 1834 – 1844
- Petty, G. W., 2004, *A first course in atmospheric radiation*. Sundog Publishing, Madison, Wisconsin
- Pili, P., 2000, Overview of the SEVIRI instrument capabilities. Report of the fourth EUMETSAT user forum in Africa Kampala, Uganda, 25 – 29 September 2000
- Pinheiro, A. C. T., Privette, J. L., Mahoney, R. and Tucker, C. J., 2004, Directional Effects in a Daily AVHRR Land Surface Temperature Dataset Over Africa. *IEEE Transactions on Geoscience and Remote Sensing*, vol. 42, no. 9, pp. 1941 – 1954
- Pinheiro, A. C. T., Privette, J. L. and Guillevic, P., 2006, Modeling the Observed Angular Anisotropy of Land Surface Temperature in a Savanna. *IEEE Transactions on Geoscience and Remote Sensing*, vol. 44, no. 4, pp. 1036 – 1047
- Prabhakara, C., Dalu, G. and Kunde V. G., 1974, Estimation of Sea Surface Temperature from remote sensing in 11- to 13 μm window region. *Journal of Geophysical Research*, vol. 79, no. 33, pp. 5039 – 5044
- Prata, A. J., 1994, Land surface temperatures derived from the Advanced Very High Resolution Radiometer and the Along-Track Scanning Radiometer 2. Experimental results and validation of AVHRR algorithms. *Journal of Geophysical Research*, vol. 99, no. D6, pp. 13025 – 13058
- Prata, A. J., Caselles, V., Coll, C., Sobrino, J. A. and Ottlé, C., 1995, Thermal remote sensing of land surface temperature from satellites: current status and future prospects. *Remote Sensing Reviews*, vol. 12, pp. 175 – 224

- Prata, A. J. and Cechet, R. P., 1999, An assessment of the Accuracy of Land Surface Temperature Determination from the GMS-5 VISSR. Remote Sensing of Environment, vol. 67, pp. 1 – 14
- Prata, A. J., Rutter, G., Lynch, M., McAttee, B. and Cechet, B., 2000, Validation of Remotely Sensed Thermal Infrared Data and Surface Temperature Algorithm Development. Earth Observation Centre (EOC) proposal, available on request as an e-document from CSIRO Atmospheric Research, PB 1 Aspendale, Victoria, Australia,
http://www.cossa.csiro.au/tasks/task2_4/EOCProp1_Report.pdf
- Prata, A. J., 2003, Land surface temperature measurement from space: Validation of the AATSR Land Surface Temperature Product. Report to the Rutherford Appleton Expert Support Laboratory, RAL, Chilton, Didcot, UK, available on request as an e-document from CSIRO Atmospheric Research, PB 1 Aspendale, Victoria, Australia
- Prata, A. J., 2004, Visiting Scientist Report: European Land Surface Temperature Validation Site for MSG/SEVIRI. Available on request as an e-document from Forschungszentrum Karlsruhe IMK-MSA, Hermann-von-Helmholtz-Platz 1, 76344 Eggenstein-Leopoldshafen, Germany
- Price, J. C., 1983, Estimating Surface Temperatures from Satellite Thermal Infrared Data – A Simple Formulation for the Atmospheric Effects. Remote Sensing of Environment, vol. 13, pp. 353 – 361
- Price, J. C., 1984, Land Surface Temperature Measurements From the Split Window Channels of the NOAA 7 Advanced Very High Resolution Radiometer. Journal of Geophysical Research, vol. 89, no. D5, pp. 7231 – 7237
- Product User Manual PUM, LST Land Surface Temperature, 2006, issue 1.3, <http://landsaf.meteo.pt/>
- Product Output Format Document POF, SAF for Land Surface Analysis LSA-SAF (Land SAF), 2006, version 1.6, issue 1.6, <http://landsaf.meteo.pt/>
- Schmidt, A., Zeitreihen der Landoberflächentemperatur abgeleitet aus Meteosat-7 Satellitendaten, 2007, Dissertation, Forschungszentrum Karlsruhe, IMK
- Snyder, W. C., Wan, Z., Zhang, Y. and Feng, Y.-Z., 1997, Requirements for Satellite Land Surface Temperature Validation Using a Split Playa. Remote Sensing of Environment, vol. 61, pp. 279 – 289

- Sobrino, J. A., Li, Z.-L., Stoll, M. P. and Becker, F., 1996, Multi-channel and multi-angle algorithms for estimating sea and land surface temperatures with ATSR data. *International Journal of Remote Sensing*, vol. 17, no. 11, pp. 2089 – 2114
- Sobrino, J. A., Li, Z.-L., Sòria, G. and Jiménez-Muñoz, J. C., 2002, Land Surface Temperature and emissivity retrieval from remote sensing data. *Recent Research Developments on Geophysics*, vol. 4, pp. 21 – 44
- Sobrino, J. A., Jiménez-Muñoz, J. C. and Paolini, L., 2004a, Land surface temperature retrieval from LANDSAT TM 5. *Remote Sensing of Environment*, vol. 90, pp. 434 – 440
- Sobrino, J. A., Sòria, G. and Prata, A. J., 2004b, Surface temperature retrieval from Along Track Scanning Radiometer 2 data: Algorithms and validation. *Journal of Geophysical Research*, vol. 109, no. D11101, doi: 10.1029/2003JD004212
- Sobrino, J. A. and Romaguera, M., 2004, Land surface temperature retrieval from MSG1-SEVIRI data. *Remote Sensing of Environment*, vol. 92, pp. 247 – 254
- Sobrino, J. A., Jiménez-Muñoz, J. C., Zarco-Tejada, P. J., Sepulcre-Cantó, G. and de Miguel, E., 2006, Land surface temperature derived from airborne hyperspectral scanner thermal infrared data. *Remote Sensing of Environment*, vol. 102, pp. 99 – 115
- The Meteosat System, 2000, Eumetsat, EUM TD 05, Revision 4, http://www.eumetsat.int/Home/Main/Publications/Technical_and_Scientific_Documentation/Technical_Descriptions/index.htm?l=en
- Wan, Z. and Dozier, J., 1989, Land-Surface Temperature Measurement from Space: Physical Principles and Inverse Modelling. *IEEE Transaction on Geoscience and Remote Sensing*, vol. 27, issue 3, pp. 268 – 278
- Wan, Z. and Dozier, J., 1996, A Generalized Split-Window Algorithm for Retrieving Land-Surface Temperature from Space. *IEEE Transaction on Geoscience and Remote Sensing*, vol. 34, no. 4, pp. 892 – 905
- Wan, Z., Zhang, Y., Zhang, Q. and Li, Z.-L., 2002, Validation of the land-surface temperature products retrieved from Terra Moderate Resolution Imaging Spectrometer data. *Remote Sensing of Environment*, vol. 83, pp. 163 – 180

9 Publications of the author

- Gajewska, E., Prata, F. and Olesen, F. S., 2006, Ground-truth for MSG Land Surface Temperature. Proceedings of Eumetsat Meteorological Satellite Conference, Helsinki, 12 – 16 June 2006
- Gajewska, E., Olesen, F. S. and Prata, F., 2006, Validation of Land Surface Temperatures (LSTs) derived from MSG/SEVIRI with the Evora, Portugal ground-truth station measurements. Second Recent Advances in Quantitative Remote Sensing. Ed. José A. Sobrino. Servicio de Publicaciones. Universitat de Valencia. Valencia, 2006
- Kabsch, E., Olesen, F., Prata, F., 2008, Initial results of the land surface temperature (LST) validation with the Evora, Portugal ground-truth station measurements. International Journal of Remote Sensing, vol. 29, no. 17, pp. 5329 – 5345, doi: 10.1080/01431160802036326
- Trigo, I. F., Monteiro, I. T., Olesen, F. S. and Kabsch, E., 2008, An assessment of remotely sensed land surface temperature. Journal of Geophysical Research, 113, D17108, doi: 10.1029/2008JD010035

10 Acknowledgement

This work would not have been possible without the support and encouragement of many persons, but especially I would like to express my gratitude to:

- Prof. Dr.-Ing. Hans-Peter Bähr (Institute of Photogrammetry und Remote Sensing, IPF, University Karlsruhe) for supervising this thesis
- Prof. Dr. Herbert Fischer (Institute of Meteorology and Climate Research, IMK, Forschungszentrum Karlsruhe) for providing me the opportunity to undertake this thesis-work
- Folke Olesen (Meteorological Satellite Applications, IMK-MSA, Forschungszentrum Karlsruhe) for his scientific guidance and support by the work
- All members of the IMK-MSA group, especially Dr. Andreas Schmidt for providing the Meteosat-7 data, Dr. Prasanjit Dash for pre-processing of AVHRR data to recognize potential validation sites and Walter Fiebig for the technical help by the construction of the Evora station
- The LSA-SAF group for providing land surface temperature and emissivity data from MSG
- Dr. Fred Prata (Norwegian Institute for Air Research, NILU, Kjeller, Norway formerly CSIRO, Marine and Atmospheric Research, Aspendale, Australia) for his advices regarding the LST validation station and providing pyrgeometer and pyranometer for the Evora station
- John Bennett (CSIRO, Marine and Atmospheric Research, Aspendale, Australia) for construction of the rotating radiometer implemented at the Evora tower and e-mailed notices concerning this instrument
- Dr. João Banza (Instituto Superior de Agronomia, ISA, Lisbon, Portugal) for assistance by the construction and maintenance of the station
- João Carreiras (Instituto Superior de Agronomia, ISA, Department of Forestry, Lisbon, Portugal) for providing the Landsat data and pre-processing of Landsat images for the retrieval of the tree canopy cover at the Evora site
- The workshop of IMK for preparation of the mountings and cases for all instruments at the Evora tower, especially Stephan Kraut for wiring up of the instrumentation for the Evora tower

- Bernhard Deny (Institute of Meteorology and Climate Research, IMK, University Karlsruhe) for programming the datalogger and his technical advises
- Dr. Wolfgang Kabsch for stylistic text editing and his useful scientific comments

11 List of used notations

Variable	Explanation	Units
B_{λ}^{-1}	inverse Planck's function at a wavelength λ	K
$B_{\lambda}(T)$	black body spectral radiance emitted at a wavelength λ and temperature T	W/(m ² sr m)
C	Wien's displacement constant (2.897768×10^{-3})	m K
c	velocity of light (2.99792458×10^8)	m/s
ε	emissivity	-
$\bar{\varepsilon}$	effective emissivity	-
ε_f	band average emissivity	-
F_B	broadband flux resulting from integrating Planck's function over all wavelengths and over a hemisphere	W/m ²
$f(\lambda)$	spectral response function of a radiometer	-
h	Planck's constant (6.626076×10^{-34})	J s
$I_{\lambda}(T)$	radiance emitted at a wavelength λ by real objects at temperature T	W/(m ² sr m)
I_{sky}	sky emitted radiance observed by a radiometer	W/(m ² sr m)
I_{sr}	surface emitted radiance observed by a radiometer	W/(m ² sr m)
I_{tot}	surface leaving radiance observed by a radiometer	W/(m ² sr m)
k	Boltzmann's constant (1.380658×10^{-23})	J/K
λ_f	weighted mean wavelength	m
p_g	area fraction of tree sub-regions	-
p_t	area fraction of grass sub-regions	-
σ	Stefan–Boltzmann constant (5.670400×10^{-8})	W/(m ² K ⁴)
$T_{10.8}$	top of atmosphere brightness temperature at 10.8 μm SEVIRI spectral band	K
$T_{12.0}$	top of atmosphere brightness temperature at 12.0 μm SEVIRI spectral band	K
T_b	brightness temperature	K
T_{sr}	land surface temperature	K

12 List of used abbreviations

AATSR	Advanced Along-Track Scanning Radiometer
ABB	Ambient Black Body of Rotrad
ASL	Above Sea Level
ATSR	Along-Track Scanning Radiometer
AVHRR	Advanced Very High Resolution Radiometer
CSIRO	Commonwealth Scientific and Industrial Research Organisation
DEM	Digital Elevation Model
EBBT	Equivalent Black Body Temperature
ECMWF	European Centre for Medium-Range Weather Forecasts
Eumetsat	European Organisation for Exploitation of Meteorological Satellites
FWHM	Full Width at Half Maximum
FZK	Forschungszentrum Karlsruhe
G1	'grass1' Rotrad measurement target
G2	'grass2' Rotrad measurement target
GERB	Geostationary Earth Radiation Budget
GMS	Geostationary Meteorological Satellite (Japanese satellite)
GMT	Greenwich Mean Time
HBB	Hot Black Body of Rotrad
HRV	High Resolution Visible
IMK	Institute for Meteorology and Climate Research (Institut für Meteorologie und Klimaforschung)
IR	Infrared
Landsat TM	Landsat Thematic Mapper
KT15	series of infrared radiation pyrometer from Heitronics
LSA-SAF	Land Surface Analysis – Satellite Application Facility
LST	Land Surface Temperature
Metop	Meteorological Operational Satellite
MFG	Meteosat First Generation
MODIS	Moderate-resolution Imaging Spectroradiometer
MSG	Meteosat Second Generation
MVIRI	Meteosat Visible and Infrared Imager
NATA	National Association of Testing Authorities
NDVI	Normalised Difference Vegetation Index
NE Δ T	Noise Equivalent Delta Temperature
NIR	Near Infrared
NOAA	National Oceanic and Atmospheric Administration
NWC	Nowcasting and Very Short Range Forecasting
RGB	Red-Green-Blue colour composite
RMS	Root Mean Square
Rotrad	Rotary Radiometer

SAF	Satellite Application Facility
SEVIRI	Spinning Enhanced Visible and Infra-Red Imager
SSP	Sub-Satellite Point
TIGR	Thermodynamic Initial Guess Retrieval
TIR	Terrestrial Infrared
TSP	Thermal Surface Parameter
UCSB	University of California, Santa Barbara
UTC	Coordinated Universal Time
VIS	Visible
VNIR	Visible and Near Infrared
WV	Water Vapour

13 Appendix

13.1 Rotrad technical details

The Rotrad was provided from CSIRO (courtesy of John Bennett), calibrated and ready to use. The calibration coefficients for the temperature sensors in Eq. 39, Eq. 40 and Eq. 41 were obtained using standard calibration techniques, i.e. the sensors were placed in a well stirred, temperature variable alcohol bath and calibrated using a data-logging system to simultaneously record the output counts of the HBB, the ABB, and the thermopile back face sensor temperature sensing elements. NATA¹ calibrated platinum (temperature resistance element) was used to determine the temperature of the variable alcohol bath.

Hot Black Body

$$\begin{aligned} HBBtemp = & 1.1862e-17 \cdot HBBcounts^4 + 3.4999e-13 \cdot HBBcounts^3 - \\ & - 0.00000000097646 \cdot HBBcounts^2 + 0.001169 \cdot HBBcounts + 23.641 \end{aligned} \quad Eq. 39$$

Ambient Black Body

$$\begin{aligned} ABBtemp = & 1.1823e-17 \cdot ABBcounts^4 + 3.5919e-13 \cdot ABBcounts^3 - \\ & - 0.0000000014135 \cdot ABBcounts^2 + 0.0011417 \cdot ABBcounts + 22.842 \end{aligned} \quad Eq. 40$$

Thermopile temperature

$$\begin{aligned} Reftemp = & 1.6234e-17 \cdot Refcounts^4 + 2.4242e-13 \cdot Refcounts^3 - \\ & - 0.0000000049527 \cdot Refcounts^2 + 0.0011678 \cdot Refcounts + 20.441 \end{aligned} \quad Eq. 41$$

HBBtemp – temperature of the HBB – close to 42°C constant

HBBcounts – radiometer counts representing the HBB temperature

ABBtemp – temperature of the ABB – close to air temperature

ABBcounts – radiometer counts representing the ABB temperature

Reftemp – housing temperature

Refcounts – radiometer counts representing the thermopile back-plane temperature

The Rotrad has its own internal geometry (Figure 13.1). The position of the sensor is indicated by the angle and by the code mode. The angles are given in grades. Each sequence in automatic mode starts from HBB continuing clockwise to ABB (100 grades), then to sky (050 grades), ground surface opposite to the sky direction (250 grades) and at the end in the direction of two user-defined angles. Two user-defined positions can be adjusted to any angle from 000 to

¹ The National Association of Testing Authorities (NATA) is Australia's national laboratory accreditation authority.

399. The smallest possible movement of the detector is limited to one step, which equals one grade (0.9 degree).

Similarly, the position modes have following code values: 252 for the HBB, 253 for the ABB, 254 for the Zenith, 255 for the Nadir, 250 for the first user-defined position and 251 for the second user-defined position. There is also a possibility to switch to manual mode. Then the sensor moves only on command.

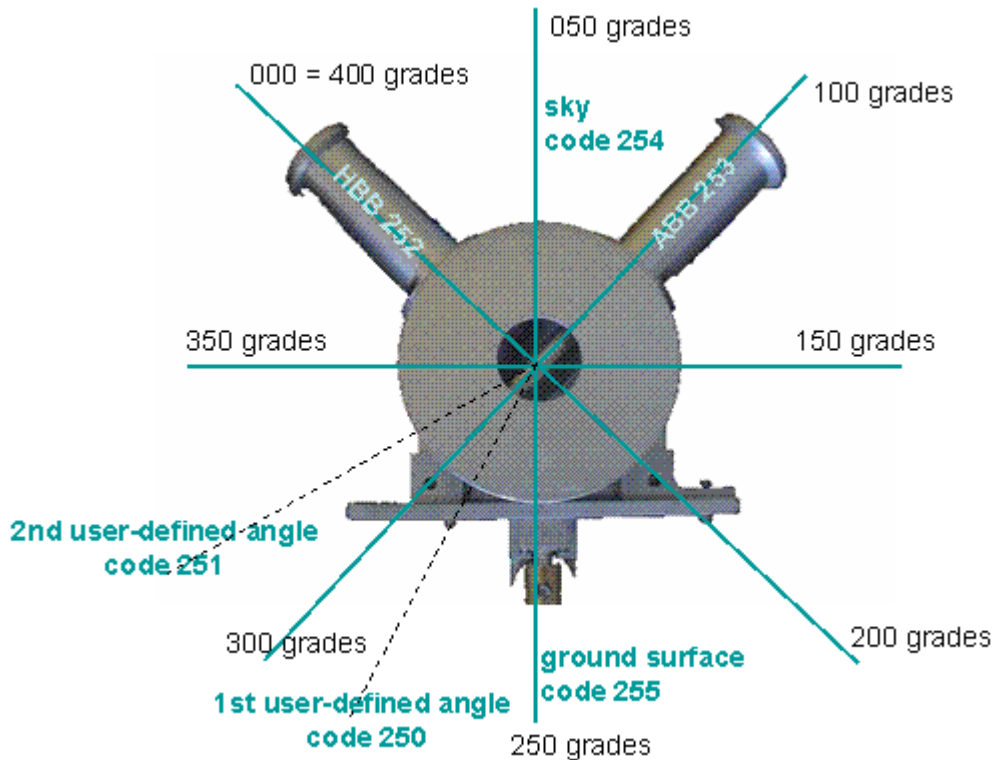


Figure 13.1: Internal geometry of the Rotrad used by the interpretation of the output data.

Data output rate ranges from 2 to 99 seconds. However, the minimum time for each direction is 10 seconds. This allows the detector to get its requested position and settle down. For skipping the position looking time must be set to null seconds.

The radiometer has its own built in data logging facility. An internal 32 Mb memory card is included for this purpose. Data are stored on the internal memory card and can be downloaded upon request to an external computer (see Table 13.2). During memory download the radiometric measurements hold on and only after 'esc' the radiometer continues its measurements. The data are saved on the memory card any time when the radiometer works, regardless if the data are saved to the file in a computer or not. After download the data still stay on the memory card, because download does not cause its erasure. When there is no more free memory on the card the old data will be replaced with current data.

Data are sent as printable ASCII characters with either comma or pipe character delimiting between the fields. The first sent character signifies the sort of data: ‘*’ is auto sent data, ‘@’ is a response to command and ‘#’ is memory card data.

Typical auto sent data stream looks e.g.:

```
* ,05/03/6,18:06:13,001|+12990,00065|-07564,00031|+13337,00004|-  
09159,00000|+32739,00000|+18862,00018|  
-27206,00002|+00027,00000|252,000
```

and is interpreted as follows:

* ,05/03/6,	Date: dd/mm/y
18:06:13,	Time: hh:mm:ss
001	ID reference (applicable if multiple radiometers used)
+12990,00065	signal counts
-07564,00031	thermopile back-plane temperature counts
+13337,00004	Hot Black Body counts
-09159,00000	Ambient Black Body counts
+32739,00000	spare
+18862,00018	power supply voltage counts
-27206,00002	reference voltage counts
+00027,00000	ADC offset counts
252,	current position of the detector (e.g. 252 corresponds to HBB)
000	looking direction of the detector from home position (HBB)

The data stream consists of number pairs, like e.g. +12990,00065|. The first five digits refer to the averaged value of the signal obtained over the sampling period as set by the command CV (Table 13.1). The radiometer signal is digitized with a multi-channel, 16 bit analogue to digital converter. The measurement is saved as integer counts, in a range from -32768 to +32767. The second five digits is the indication of signal quality given as difference between the maximum signal and the minimum signal in the sample period, saved as unsigned integer (from 00000 to 65535).

The Rotrad samples at 10 kHz rate, and it outputs minimum 2 s data average via serial port. The configuration of the RS232 is as follows:

Baud rate: 57600

Parity: N

Data bits: 8

Stop bits: 1

Flow control: none

A serial output of the radiometer can be observed on a PC using e.g. Microsoft HyperTerminal in a rate adjusted by the analogue print/log time. HyperTerminal is also used to send command to the Rotrad. The Rotrad commands are listed in Table 13.1 and in Table 13.2. Note <x> indicate user variables, in this case, one character. There is a response time to commands and the unit processes only one command at a time. All commands end in a carriage return.

Command	Description
CA<x>	Set the system into auto mode <x>=1 or manual mode <x>=0. Auto mode runs the set sequence looking at HBB, ABB, Up, 1st used-defined position, 2nd user-defined position then Down for programmed times (see CTH<xxx>, CTA<xxx>, CTU<xxx>, CT1<xxx>, CT2<xxx>, CTD<xxx>). The system outputs data to the RS232 port at CV<xx> rate and logs to memory at the same rate. In Manual mode, it stays at current view until externally commanded to move. Data outputs still at CV<xx> rate.
CD	Request the current date. Date is returned as dd\mm\y, where dd is day, mm is month and y is year number in a four year leap year system, 0 is a leap year.
CD<ddmmyy>	Set the date to dd\mm\y
CT	Request current time from logger, data returned as @CThh:mm:ss where hh is hour, mm is minute and ss is second in 24hour format.
CT<hhmmss>	Set the time to hh:mm:ss
CV	Return the current analog print/log rate, return is @CVxx where xx is seconds.
CV<xx>	Set the analog prin/log time to xx seconds, where xx is 02 to 99.
CH<x>	Enable or disable the hot black body heater controller where x=1 is enabled and x=0 is disabled.
CSH	Send the mirror to look at the HBB
CSA	Send the mirror to look at the ABB
CSU	Send the mirror to look at the sky target
CSD	Send the mirror to look at the surface target
CSF	Single Step Mirror Forward
CSB	Single Step Mirror Back
CI	Return the site ID, return is @CIxxx, where xxx is from 000 to 255.
CI<xxx>	Set the site ID to xxx where xxx is 000 to 255.

CSO	Turn off power to the mirror stepping motor after moving, conserves power and stops heating, but mirror only held in position by motor magnets.
CSX	Leave power on to mirror stepping motor after moving.
CP	Force an analog print
CPI<xxx>	Set the steps for 1 st user-defined position (xxx = 000 to 399)
CP2<xxx>	Set the steps for 2 nd user-defined position (xxx = 000 to 399)
CR	Reset automatic scan sequence to start (HBB)
CT1<xxx>	Set time looking at programmable position 1 to xxx seconds (010-600)
CT2<xxx>	Set time looking at programmable position 2 to xxx seconds (010-600)
CTH<xxx>	Set time looking at HBB to xxx seconds (010-600)
CTA<xxx>	Set time looking at ABB to xxx seconds (010-600)
CTD<xxx>	Set time looking at surface to xxx seconds (010-600)
CTU<xxx>	Set time looking at sky to xxx seconds (010-600)
CTP	Print Scan looking times
C?	Print command list

Table 13.1: Rotrad commands.

Command	Description
'esc'	Cancels a memory card download
CM	Return Memory Card Status
CMD	Initiate a memory card download from StartOfDump to Current pointers
CML	Set the StartOfDump pointer to LastDownload pointer
CMR	Set the StartOfDump pointer and LastDownload pointer to Current pointer
CMZ	Reset all pointers to default
CMI	Cause a memory card re-initialisation
CMA	Download entire memory card from block 0 to size
CMS<xxxxxx>	Set StartOfDump pointer to xxxxx
CMI<xxxxxx>	Set Current pointer to xxxxx
CM<xxxxxx>,<yyyyy>	Download from block xxxxx to yyyyy

Table 13.2: Commands for the Rotrad internal memory card.

13.2 Description of datalogger output file

No.	Label	Value	Units
1	7 L	Version of file	*.dld
2	_RTM L	Julian day in year	xxx
3	_RTM L	Time	hhmm
4	Temp_2m_AVG L	Air temperature at 2 m	°C
5	Temp_Mast_AVG L	Air temperature at 28 m	°C
6	rF_2m_AVG L	Relative air humidity at 2m	%
7	rF_Mast_AVG L	Relative air humidity at 28 m	%
8	WG_mps_S_WVT L	Wind speed at 2m	m/s
9	WR_Grad_D1_WVT L	Wind direction at 2m	degrees
10	WR_Grad_SD1_WVT L	Standard deviation of (9)	degrees
11	LWRad_PIR_AVG L	Longwave radiation (pyrgeometer: 3 – 100 μ m)	mV
12	RThPIR_AVG L	Case temperature of the pyrgeometer as resistance	k Ω
13	RT_KT15_AVG L	Surface brightness temperature (KT15.82: 8 – 14 μ m, objective: M6)	°C
14	TotRadBF3_AVG L	Total radiation (0.4 – 7 μ m)	W/m ²
15	DifRadBF3_AVG L	Diffuse radiation (0.4 – 7 μ m)	W/m ²
16	TRadEP09_AVG L	Shortwave radiation (pyranometer: 0.3 – 3 μ m)	W/m ²
17	EP09Temp_AVG L	Internal ambient temperature of pyranometer	°C
18	EP09Seal_AVG L	Hermetic seal integrity output from pyranometer	mV
19	UBatterie_AVG L	Voltage of the battery	V
20	Temp_2m_STD L	Standard deviation of (4)	°C
21	Temp_Mast_STD L	Standard deviation of (5)	°C
22	rF_2m_STD L	Standard deviation of (6)	%
23	rF_Mast_STD L	Standard deviation of (7)	%
24	WG_mps_STD L	Standard deviation of (8)	m/s
25	LWRad_PIR_STD L	Standard deviation of (11)	mV
26	RThPIR_STD L	Standard deviation of (12)	k Ω
27	RT_KT15_STD L	Standard deviation of (13)	°C
28	TotRadBF3_STD L	Standard deviation of (14)	W/m ²
29	DifRadBF3_STD L	Standard deviation of (15)	W/m ²
30	TRadEP09_STD L	Standard deviation of (16)	W/m ²

Table 13.3: Description for each column in a datalogger output file acquired before March 21, 2007.

No.	Label	Value	Units
1	8 L	Version of file	*.dld
2	_RTM L	Julian day in year	xxx
3	_RTM L	Time	hhmm
4	Temp_2m_AVG L	Air temperature at 2 m	°C
5	Temp_Mast_AVG L	Air temperature at 28 m	°C
6	rF_2m_AVG L	Relative air humidity at 2m	%
7	rF_Mast_AVG L	Relative air humidity at 28 m	%
8	WG_mps_S_WVT L	Wind speed at 2m	m/s
9	WR_Grad_D1_WVT L	Wind direction at 2m	degrees
10	WR_Grad_SD1_WVT L	Standard deviation of (9)	degrees
11	LWRad_PIR_AVG L	Longwave radiation (pyrgeometer: 3 – 100 μm)	mV
12	RThPIR_AVG L	Case temperature of the pyrgeometer as resistance	k Ω
13	RT_KT15_AVG L	Radiative surface temperature (KT15.82: 8 – 14 μm , objective: M6)	°C
14	RT_Himmel_AVG L	Radiative sky temperature (KT15.85: 9.5 – 11.5 μm , objective: L6, nr 8142)	°C
15	RT_Baum_AVG L	Radiative surface temperature (KT15.85: 9.5 – 11.5 μm , objective: L6, nr 8141) pointing to the tree	°C
16	RT_Wiese_AVG L	Radiative surface temperature (KT15.85: 9.5 – 11.5 μm , objective: L6, nr 8140) pointing to the grass	°C
17	TotRadBF3_AVG L	Total radiation (0.4 – 7 μm)	W/m ²
18	DifRadBF3_AVG L	Diffuse radiation (0.4 – 7 μm)	W/m ²
19	TRadEP09_AVG L	Shortwave radiation (pyranometer: 0.3 – 3 μm)	W/m ²
20	EP09Temp_AVG L	Internal ambient temperature of pyranometer	°C
21	EP09Seal_AVG L	Hermetic seal integrity output from pyranometer	mV
22	UBatterie_AVG L	Voltage of the battery	V
23	Temp_2m_STD L	Standard deviation of (4)	°C
24	Temp_Mast_STD L	Standard deviation of (5)	°C
25	rF_2m_STD L	Standard deviation of (6)	%
26	rF_Mast_STD L	Standard deviation of (7)	%
27	WG_mps_STD L	Standard deviation of (8)	m/s
28	LWRad_PIR_STD L	Standard deviation of (11)	mV
29	RThPIR_STD L	Standard deviation of (12)	k Ω
30	RT_KT15_STD L	Standard deviation of (13)	°C
31	RT_Himmel_STD L	Standard deviation of (14)	°C
32	RT_Baum_STD L	Standard deviation of (15)	°C
33	RT_Wiese_STD L	Standard deviation of (16)	°C
34	TotRadBF3_STD L	Standard deviation of (17)	W/m ²
35	DifRadBF3_STD L	Standard deviation of (18)	W/m ²
36	TRadEP09_STD L	Standard deviation of (19)	W/m ²

Table 13.4: Description for each column in a datalogger output file acquired after update, i.e. after March 21, 2007.